Quasi-real photo-production of hyperons on polarized ^{1,2}H targets

David Heesbeen

The work described in this thesis is part of the research program of the 'Stichting voor Fundamenteel Onderzoek der Materie (FOM)', which is financially supported by the 'Nederlands organisatie voor Wetenschappelijk Onderzoek (NWO)'.

RIJKSUNIVERSITEIT GRONINGEN

Quasi-real photo-production of hyperons on polarized ^{1,2}H targets

Proefschrift

ter verkrijging van het doctoraat in de
Wiskunde en Natuurwetenschappen
aan de Rijksuniversiteit Groningen
op gezag van de
Rector Magnificus, dr. F. Zwarts,
in het openbaar te verdedigen op
vrijdag 6 juni 2003
om 16:00 uur

door

David Heesbeen

geboren op 22 april 1969
te Alkmaar

Promotores:	Prof. dr. G. van der Steenhoven
	Prof. dr. P.K.A. de Witt Huberts
Co-promotor:	Dr. J.J.M. Steijger
Beoordelingscommissie:	Prof. dr. E. Laenen
	Prof. dr. H. Löhner
	Prof. dr. S. Belostotski

Contents

Chapter 1

Introduction

The constituents of atomic nuclei, i.e. the protons and neutrons, are composed of quarks and gluons. The interactions between these particles are governed by the strong interaction, which is described by Quantum Chromo Dynamics (QCD). Unfortunately, perturbative QCD calculations, i.e. calculations based on an expansion in powers of the strong coupling constant α_s, are not always possible due to the increase of α_s at large distances or small momenta. As a consequence, it is not possible to calculate the internal structure of nucleons from first principles. It is, however, possible to calculate observables for lepton-quark scattering reactions in a QCD framework, in which the nucleon structure is modeled by - a priori unknown - structure functions. Hence, lepton-quark scattering data can be used to obtain experimental values for the structure functions. Such experiments are known as Deep-Inelastic Scattering (DIS) experiments.

Since the late sixties DIS experiments have been performed at various laboratories. These experiments proved that the scattering takes place on pointlike spin-$\frac{1}{2}$ particles residing in the nucleon, which subsequently became known as quarks.

Originally, it was assumed that the spin of the nucleon (of $\frac{1}{2}$) could be fully attributed to the spin of the quarks. It was assumed that the spins of two quarks cancel and that the remaining quark gives the spin of the nucleon. It was a surprise when the EMC experiment [1] showed in 1988 that only a small fraction ($14 \pm 9 \pm 21$ %) of the proton spin could be attributed to the quark spins. After the EMC experiment other experiments carried out at SLAC, CERN and DESY confirmed the small value of $\Delta\Sigma$ reported by EMC[1].

Since then, it was realized that the nucleon spin originates from several components.

[1]It is noted that use is made of experimental information on weakly decaying baryons in extracting $\Delta\Sigma$ from the spin-dependent structure function data.

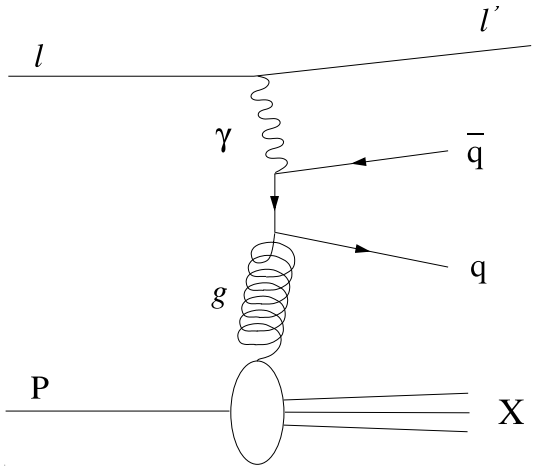

Figure 1.1: *Leading order $q\bar{q}$-production via the photon gluon fusion process in lepton scattering off a proton.*

Apart from the intrinsic angular momentum of the quarks ($\Delta\Sigma$) and gluons (ΔG), the orbital angular momentum of the quarks (L_q) and gluons (L_g) may also contribute to the total angular momentum of the proton:

$$\frac{1}{2} = \frac{1}{2}\Delta\Sigma + \Delta G + L_q + L_g \tag{1.1}$$

The quark spin contribution can be further decomposed into contributions from the different flavors, i.e. $\Delta\Sigma = \Delta u + \Delta\bar{u} + \Delta d + \Delta\bar{d} + \Delta s + \Delta\bar{s}$. The contribution of charm or heavier quarks is usually neglected, as it is believed to be very small.

The gluon contribution to the nucleon spin can be obtained from the Q^2 evolution of the polarized structure functions or by identification of events in which the virtual photon couples directly to the gluons. The orbital angular momentum contribution is much more difficult to access. Recently, it has been suggested [2] that the target transverse spin asymmetry in exclusive meson or photon production is very sensitive to the total angular momentum of the quarks from which information on L_q can be derived.

A way to access the gluon spin contribution is provided by the photon-gluon fusion process (PGF). In figure 1.1 this process is depicted in leading order. The virtual photon splits into a $q\bar{q}$ pair, of which one quark interacts with a target gluon. In order to separate this process from background processes it is required that the transverse momentum of the q and $\bar{q}$ quarks is relatively large. Another method to identify PGF is provided by searching for charmed hadrons, which are characteristic for PGF as other processes do not usually result in the production of charmed hadrons.

In this thesis, I present the results of a search for the lightest charm baryon, the Λ_c^+ (2284.9 MeV), which has a *udc* quark structure. It is believed that in the HERMES experiment a relatively large fraction of the c quarks fragment into a Λ_c^+ baryon since we

are in the threshold regime for c quark production. For instance, at the threshold only the reaction $l + p \rightarrow \Lambda_c^+ \overline{\mathrm{D}}^0$ can occur. By identifying the Λ_c^+ and trying to measure the asymmetry of the yield with respect to the beam and target spin orientations it is hoped to get information on the gluon polarization. In the presented measurements the DIS lepton was not explicitly identified which brings us in the quasi-real photoproduction regime. The advantage of this is that the cross sections are an order of magnitude higher than in the DIS regime. At the same time many background processes are also enhanced which may possibly contribute to the measured double spin asymmetries. These contributions are unconnected to the photon-gluon fusion process, and may thus dilute the asymmetry.

The study of the helicity dependence of Λ_c^+ production motivated in part the design and implementation of the Lambda Wheels, a new wheel shaped array of silicon counters that has been installed in the HERMES front region. The Lambda Wheels will increase the Λ^0 hyperon statistics per unit luminosity by a factor of four with respect to the statistics obtained with the standard HERMES acceptance. Another reason to build the Lambda Wheels is the possibility to enter the target fragmentation domain for Λ^0 production. This is interesting as it is possible to determine the relative orientation of u and s quarks in the nucleon from the Λ^0 decay products in the target fragmentation domain [3]. In the second part of this thesis the results are presented of a performance study of a prototype Lambda Wheel module.

The thesis is organized as follows. In chapter 2 the theoretical framework which motivates the analysis presented in this thesis is given.

In order to place the Lambda Wheel design and the search for the Λ_c^+ baryon presented in this thesis in perspective the HERMES experiment is briefly described in chapter 3.

In chapter 4 the analyses in which signals for the $\Sigma^\star$, Ξ and Λ_c^+baryons are extracted are described. These analyses have in common that the above mentioned particles have a decay chain in which a Λ hyperon and a π meson appear. For the $\Sigma^\star$ and Ξ hyperons a double spin asymmetry is built from the number of counts extracted from the peaks. For the Λ_c^+ baryon the obtained statistics is too low to construct such an asymmetry, and for this reason other undetected particles are allowed in the final state (partial reconstruction). Consequently, Monte Carlo simulations are needed to determine the amount of Λ_c^+ baryons present in a certain mass range and the corresponding amount of background events. This chapter is concluded by the evaluation of a double spin asymmetry for these partially reconstructed Λ_c^+ baryons. From this asymmetry a value of the gluon polarization $\Delta G/G$ is extracted.

In order to have a higher detection probability for the Λ_c^+ baryon, a new detector has been designed and commissioned in 2002. In Chapter 5 the physics motivation and details of the design of the Lambda Wheels are given. First operational results obtained with a prototype module are presented.

The Lambda Wheels cannot be incorporated in the existing tracking program of HERMES due to its wider acceptance, and because the strip orientation is not parallel to the standard wire orientation in the other tracking detectors. A tracking program for the Lambda Wheels has been developed and incorporated into the eXternal Tracking Code (XTC) that is also used for other wide angle detectors of the HERMES spectrometer. The Lambda Wheel part of the tracking program, that has been used to analyze the data of a first operational Lambda Wheel module, is described. Insight is given in the selection methods used to combine the strips of different planes into physical tracks. In this chapter also a method is given to determine the tracking efficiency of the Lambda Wheel silicon planes. This method is applied to various situations.

A summary and outlook is given in the final chapter.

Chapter 2

Theoretical Framework

2.1 Deep-Inelastic Scattering

In the HERMES experiment at DESY leptons (electrons or positrons) are scattered off nucleons and part of the final state particles can be observed. Under certain restrictions on the event kinematics (to be discussed in section 2.1.1), deep-inelastic scattering (DIS) events are sampled. In a DIS event an exchange boson emitted by the beam lepton interacts with a parton in the nucleon. Due to the relatively low beam energy at HERMES as compared to the Z and W boson mass only the exchange of virtual photons needs to be considered.

2.1.1 Kinematics

In figure 2.1 the kinematics of a DIS event is sketched. The momentum and energy of the incoming lepton are represented by $\vec{k}$ and E, respectively. After scattering over a polar angle θ the momentum and energy of the leptons are different which is denoted by a prime ($\vec{k}'$ and E', respectively). In inclusive DIS only the scattered lepton is detected. In that case knowledge of the incident lepton energy E (27.55 GeV), and the quantities E' and θ suffice to describe the event completely. From these variables, the negative squared four momentum of the virtual photon Q^2, the energy transfer of the lepton to the target ν, and the square of the mass of the final state W^2 can be defined. In the laboratory frame, these quantities are related to the measured variables according to:

$$Q^2 \stackrel{\text{lab}}{=} 4EE'\sin^2(\theta/2) > 0, \tag{2.1}$$

$$\nu \stackrel{\text{lab}}{=} E - E', \tag{2.2}$$

$$W^2 \stackrel{\text{lab}}{=} M^2 + 2M\nu - Q^2 \tag{2.3}$$

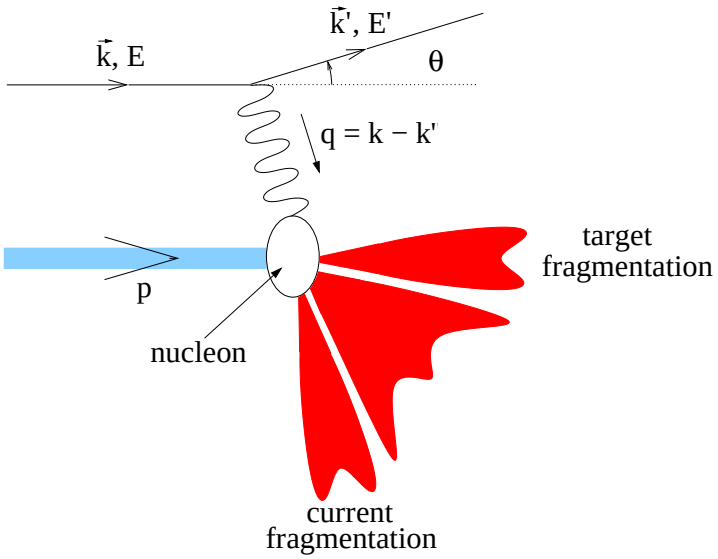

Figure 2.1: *Schematic picture of deep-inelastic lepton-nucleon scattering in the one-photon exchange approximation. The hadron formation or fragmentation process is represented by the dark shaded areas. The current fragmentation domain correspond to hadrons that result from the struck quark. In the target fragmentation domain the hadrons originate from the remnant quarks in the nucleon.*

with M the mass of the nucleon. Note that the lepton mass m is neglected. The dimensionless variables

$$x \overset{\text{lab}}{=} \frac{Q^2}{2\,M\,\nu} \qquad \text{and} \tag{2.4}$$

$$y \overset{\text{lab}}{=} \frac{\nu}{E} \tag{2.5}$$

can be defined. The so-called Bjorken scaling variable x is a measure of the inelasticity of the reaction, and y is a measure of the fractional energy transfer of the photon. Their physical ranges are given by $0 \leq x \leq 1$ and $0 \leq y \leq 1$. The kinematic restrictions that are usually imposed on deep-inelastic scattering correspond to $Q^2 > 1$ GeV^2 and $W > 2$ GeV. The minimum value for Q^2 is needed to ensure the validity of perturbative QCD, while the minimum value for W is needed to stay away from the baryon resonance region.

2.1.2 Unpolarized cross section

In the one-photon exchange approximation the lepton-nucleon DIS cross section can be expressed in terms of a leptonic tensor $L^{\mu\nu}$ and a hadronic tensor $W_{\mu\nu}$:

$$\frac{d^2\sigma}{d\Omega dE'} = \frac{\alpha^2}{Q^4}\frac{E'}{E}L^{\mu\nu}W_{\mu\nu}, \tag{2.6}$$

where $\alpha \approx \frac{1}{137}$ is the electromagnetic fine structure constant. The tensor associated with the lepton vertex $L^{\mu\nu}$ is exactly calculable in Quantum Electro Dynamics (QED). After averaging over initial spin states and summing over the final spin states it can be written as [4]

$$L^{\mu\nu} = 2(k'^{\mu}k^{\nu} + k'^{\nu}k^{\mu} - (k' \cdot k - m^2)g^{\mu\nu}), \tag{2.7}$$

where $g^{\mu\nu}$ is the metric tensor, and m the lepton mass.

It is not possible to calculate the hadronic tensor $W_{\mu\nu}$ rigorously from first principles like $L^{\mu\nu}$. However, using symmetry arguments and QED conservation laws it can be parametrized by writing $W_{\mu\nu}$ in terms of the hadron momentum p and the virtual photon momentum q as a sum of the structure functions W_1 and W_2 which are themselves a function of Q^2 and ν

$$W_{\mu\nu} = W_1\left(-g_{\mu\nu} + \frac{q_\mu q_\nu}{q^2}\right) + W_2\frac{1}{M^2}\left(p_\mu - \frac{p\cdot q}{q^2}q_\mu\right)\left(p_\nu - \frac{p\cdot q}{q^2}q_\nu\right). \tag{2.8}$$

Using expressions 2.7 and 2.8 for the two tensors, the unpolarized cross section can be written as [4]

$$\frac{d^2\sigma}{d\Omega dE'} = \frac{(2\alpha E')^2}{Q^4}\left[W_2(Q^2,\nu)\cos^2\frac{\theta}{2} + 2W_1(Q^2,\nu)\sin^2\frac{\theta}{2}\right]. \tag{2.9}$$

It is customary to replace W_1 and W_2 by two dimensionless structure functions F_1 and F_2, which are defined as

$$F_1(x,Q^2) = MW_1(x,Q^2), \tag{2.10}$$
$$F_2(x,Q^2) = \nu W_2(x,Q^2). \tag{2.11}$$

Using these expressions the unpolarized DIS cross section can be written as

$$\frac{d^2\sigma}{dxdQ^2} = \frac{4\pi\alpha^2}{Q^4}\cdot[F_1(x,Q^2)\cdot y^2 + \frac{F_2(x,Q^2)}{x}\cdot(1 - y - \frac{Mxy}{2E})]. \tag{2.12}$$

The observation that F_1 and F_2 do not depend on Q^2 for a given value of x led to the Quark Parton Model (QPM). In this model the structure functions are written as an

incoherent sum over inelastic contributions associated with 'partons', i.e. structureless particles within the nucleon. If the spin of the partons is $\frac{1}{2}$, the structure functions F_1 and F_2 are related via the relation

$$F_2(x) \;=\; 2xF_1(x)\,, \tag{2.13}$$

which is known as the Callan-Gross relation. The experimental confirmation of this relation has been used as experimental evidence for the spin-$\frac{1}{2}$ character of the quarks.

2.2 Spin structure of the nucleon

In the previous section possible spin dependencies in $L^{\mu\nu}$ and $W_{\mu\nu}$ were not considered. At HERMES a polarized lepton beam scatters off a polarized target and thus the spin dependencies should be taken into account. If one does so, two spin-dependent structure functions $g_1(x)$ and $g_2(x)$ need to be introduced, which are the polarized analogues of the spin-independent structure functions F_1 and F_2. However, for the spin-dependent structure functions no such relation as the Callan-Gross relations exists.

Data on the spin-dependent structure functions can be obtained from a cross section difference measurement. If longitudinally polarized leptons are scattering off a longitudinally polarized target the longitudinal double-spin asymmetry $A_\parallel$ is usually measured. It is defined by

$$A_\parallel = \frac{\sigma^{\overrightarrow{\Leftarrow}} - \sigma^{\overrightarrow{\Rightarrow}}}{\sigma^{\overrightarrow{\Leftarrow}} + \sigma^{\overrightarrow{\Rightarrow}}}, \tag{2.14}$$

where $(\overrightarrow{\Leftarrow})\ \overrightarrow{\Rightarrow}$ denotes the case where the lepton ($\rightarrow$) and nucleon ($\Leftarrow$ or $\Rightarrow$) spins are aligned (anti) parallel. If one neglects the contribution of the transverse structure function g_2 (which can be measured in separate experiments using a transversely polarized target), the measured polarization $A_\parallel$ is related to the structure functions g_1 and F_1 through:

$$\frac{A_\parallel}{D} \approx \frac{g_1}{F_1} \approx A_1, \tag{2.15}$$

where D represents the virtual photon depolarization factor given by

$$D = \frac{y(2-y)}{y^2 + 2(1-y)(1+R)}. \tag{2.16}$$

The quantity y $(=\frac{\nu}{E})$ has been introduced before, and R represents the ratio of the longitudinal and transverse photo-absorption cross sections in deep-inelastic scattering.

Information on the spin structure of the nucleon is obtained from asymmetry measurements (Eq. 2.14) in various event topologies. In inclusive spin dependent DIS (section 2.2.1) the helicity distribution $g_1(x)$ is measured. If also a hadron is observed (section 2.2.2) information on quark helicities for separate flavors is obtained. By making use of scaling violations of inclusive spin dependent DIS information on the gluon polarization can be extracted (section 2.2.3).

2.2.1 Inclusive spin-dependent DIS

In the Quark Parton Model (QPM), deep-inelastic lepton-nucleon scattering is interpreted as incoherent scattering of a lepton from quarks in the nucleon. In the infinite momentum frame, the scaling variable x corresponds to the momentum fraction carried by the struck quark. In this framework the (un)polarized parton distributions depend on x, and can be defined as

$$q_f(x) \equiv q_f^{\overrightarrow{\leftarrow}}(x) + q_f^{\overleftarrow{\leftarrow}}(x) \qquad \text{and} \tag{2.17}$$

$$\Delta q_f(x) \equiv q_f^{\overrightarrow{\leftarrow}}(x) - q_f^{\overleftarrow{\leftarrow}}(x), \tag{2.18}$$

where the terms $q_f^{\overrightarrow{\leftarrow}}(x)$ and $q_f^{\overleftarrow{\leftarrow}}(x)$ denote the probabilities to find a parton of type f with momentum fraction x with its spin anti-parallel or parallel to the nucleon spin. The (un)polarized structure functions can be written as

$$\begin{array}{ll} F_1(x) = \frac{1}{2}\sum_f e_f^2 q_f(x), & F_2(x) = x\sum_f e_f^2 q_f(x), \\ g_1(x) = \frac{1}{2}\sum_f e_f^2 \Delta q_f(x), & g_2(x) = 0, \end{array} \tag{2.19}$$

where the sum runs over the quark flavors present in the nucleon and e_f is the charge of a quark with flavor f.

It is possible to determine $g_1(x)$ for the proton or the neutron (from polarized deuterium or ^{3}He data) by measuring the asymmetry given by Eq. 2.14. As can be seen from Eq 2.19 such data only give information on the sum of the quark polarizations over all flavors. If SU(3) symmetry is assumed and the integral of the structure function $g_1(x)$ over x for the proton is combined with data on hyperon decays, it is possible to extract the first moments ($\int_0^1 \Delta q(x)\mathrm{d}x$) of the flavor separated spin-dependent quark distributions, $\Delta q_f(x)$, which are also often represented as $\Delta u(x) = \Delta q_u(x)$, $\Delta d(x) = \Delta q_d(x)$, etc. However, the full x-dependence of $\Delta q_f(x)$ for the various quark flavors including information on possibly polarized sea quarks, requires the use of semi-inclusive data, which is the subject of the next subsection.

2.2.2 Semi-Inclusive spin-dependent DIS

In semi-inclusive deep-inelastic scattering (SIDIS), a high-momentum hadron is detected in coincidence with the scattered beam lepton. Depending on the momentum of a hadron in the final state a separation into two distinct kinematic regions can be made, i.e. the current fragmentation region and the target fragmentation region. In the current fragmentation region the final state hadron contains the quark struck by the virtual photon, and in the target fragmentation region the final state hadron originated from the spectator remnants of the nucleon. After imposing requirements on the event kinematics it can be made fairly probable that the observed hadron is a fragmentation product that carries the struck quark, i.e. it is a current fragmentation product. In order to quantify these requirements two dimensionless variables are introduced

$$z \stackrel{\text{lab}}{=} \frac{E_h}{\nu} \qquad \text{and} \tag{2.20}$$

$$x_F \approx 2p_{\parallel}/W, \tag{2.21}$$

where z is the ratio of the energy E_h transfered from the virtual photon to the hadron over the virtual photon energy ν, and x_F is the Feynman scaling variable. The latter is approximated by taking the longitudinal momentum component $p_{\parallel}$ of the hadron in the γN center of momentum frame. A fast-forward hadron produced a DIS event has a very high probability to contain the struck quark [5]. In ref. [6] hadrons with high forward momenta in the $\gamma^{\star}N$ center of mass system are selected imposing $z > 0.2$ and $x_F > 0$. In contrast, low momentum hadrons from the target fragmentation region are have $x_F < 0$.

In semi-inclusive deep-inelastic scattering the spin-dependent functions $\Delta q_f(x)$ can be measured for individual quark flavors f because the quark hadronization process can be modeled [7] which makes it possible to evaluate the probabilities that quarks of a given flavor were struck. Using these probabilities, it is possible to decompose the quark spin into its different flavors, provided that both polarized leptons and polarized targets are used. At HERMES such a complete flavor decomposition [6] of the nucleon spin, in leading order QCD, has been performed on the basis of a set of measured semi-inclusive asymmetries. The measured asymmetries $A_{\parallel}^h$ for various hadrons h are related to the polarized quark distributions Δq_f according to

$$\frac{A_{\parallel}^h(x,Q^2)}{D} \approx \frac{\sum_f e_f^2\, \Delta q_f(x,Q^2) \int dz\, \mathrm{D}_f^h(z,Q^2)}{\sum_f e_f^2\, q_f(x,Q^2) \int dz\, \mathrm{D}_f^h(z,Q^2)}, \tag{2.22}$$

where the fragmentation function $\mathrm{D}_f^h(z,Q^2)$ represents the probability density of a quark of flavor f to produce a hadron h with an energy fraction z of the energy of

the virtual photon. Energy conservation implies that the fragmentation functions are normalized such that

$$\sum_h \int_0^1 dz\, z\, \mathrm{D}_f^h(z, Q^2) = 1. \tag{2.23}$$

Using iso-spin invariance and charge conjungation invariance the total number of independent fragmentation functions can be reduced. If, for example, only the u, d and s quarks are considered three fragmentation functions remain in the case of pions:

$$\begin{array}{rcccccccc} \mathrm{D}^+ & \equiv & \mathrm{D}_u^{\pi^+} & = & \mathrm{D}_{\bar{d}}^{\pi^+} & = & \mathrm{D}_d^{\pi^-} & = & \mathrm{D}_{\bar{u}}^{\pi^-}\,, \\ \mathrm{D}^- & \equiv & \mathrm{D}_d^{\pi^+} & = & \mathrm{D}_{\bar{u}}^{\pi^+} & = & \mathrm{D}_u^{\pi^-} & = & \mathrm{D}_{\bar{d}}^{\pi^-}\,, \\ \mathrm{D}_s & \equiv & \mathrm{D}_s^{\pi^+} & = & \mathrm{D}_{\bar{s}}^{\pi^+} & = & \mathrm{D}_s^{\pi^-} & = & \mathrm{D}_{\bar{s}}^{\pi^-}\,, \end{array} \tag{2.24}$$

with D^+ the favored fragmentation function as the pion produced by each quark has that quark in its ground state wave function. The unfavored fragmentation function and strange quark fragmentation functions are described by D^- and D_s.

The fragmentation functions cannot be calculated from first principles. If the cross section is factorized into nucleonic parton distributions, partonic cross sections and the unknown fragmentation functions, the fragmentation functions can be obtained from a fit through cross section data. They can also be obtained from a fragmentation model like the Lund String Model. In this model, the confinement potential of the struck quark is assumed to originate from an initial $q\bar{q}$ string. This potential increases as the string is stretched. After a certain increase in potential energy the string breaks forming a $q\bar{q}'$ and a $q'\bar{q}$ string. Subsequently, these strings may break as well. After the remaining energy reaches a certain minimum this process is stopped and hadrons are formed. In this hadronization process a $q\bar{q}$ pair will result in the formation of mesons, while initial strings of the type $q(q\bar{q})$ need to be considered to allow for the formation of baryons.

Using the flavor tagging method described above the fraction of the nucleon spin carried by the separate flavors has been determined at $Q^2 = 2.5$ GeV^2 in Ref. [6]. (A similar analysis based on the first few years of data taking at HERMES was published in Ref. [8].) In table 2.1 the resulting spin contributions carried by the separate flavors and their combined contribution to the nucleon spin are given. From table 2.1 it is seen that most of the nucleon spin is carried by the u and d quarks. As these contributions are oppositely oriented, the total amount of spin carried by the quarks amounts to only 44 % of the QPM expectation.

Table 2.1: *Contribution of the various quark flavors to the nucleon spin [6]. The sum ($\Delta\Sigma$) of all the flavors is also listed. The quoted measurements at $Q^2 = 2.5$ GeV^2 correspond to the first moments of the various spin distributions $\Delta q_f(x)$.*

$$\begin{aligned} \Delta u &= 0.61 \pm 0.02 \pm 0.08 \\ \Delta d &= -0.24 \pm 0.03 \pm 0.07 \\ \Delta \bar{u} &= 0.04 \pm 0.03 \pm 0.07 \\ \Delta \bar{d} &= -0.01 \pm 0.03 \pm 0.05 \\ \Delta s + \Delta \bar{s} &= 0.05 \pm 0.03 \pm 0.07 \\ \\ \Delta\Sigma &= 0.442 \pm 0.026 \pm 0.064\ . \end{aligned}$$

In order to make up for the total spin of the proton it has been suggested that the gluons are also polarized, and/or that the partons have a non-zero orbital angular momentum.

2.2.3 Gluon polarization

A virtual photon only scatters off charged particles. It is therefore not possible to scatter directly off the gluons present in the nucleon. It is, however, possible to access the gluon polarization using the *axial anomaly* (see Ref [9, 10]). Here an anomalous contribution arises in the axial current matrix element a_0, which introduces a point-like interaction between the flavor singlet current J^0_μ and gluons. After modification the axial-vector current element (for three quark flavors) is given by

$$a_0(Q^2) = \Delta\Sigma - \frac{3\alpha_s(Q^2)}{2\pi}\Delta G(Q^2)\,. \tag{2.25}$$

Using the flavor decomposition analysis described in the previous subsection it is possible to obtain experimental information on a_0. Using $\Delta\Sigma$ and a_0 as obtained from such an analysis a value for $\Delta G/G$ can be determined. In Ref. [6] this method is applied to the most recent spin-dependent semi-inclusive data. From this analysis a value for a_0 of 0.48 ± 0.17 on the proton and 0.27 ± 0.17 on the neutron was found. Taking the average value for a_0 and $\Delta\Sigma = 0.442 \pm 0.026 \pm 0.064$ as given in table 2.1 the following value for the gluon polarization, $\Delta G(2.5\ \text{GeV}^2) = 1.08 \pm 0.76(\text{stat}) \pm 0.81(\text{syst})$ was evaluated.

It is also possible to determine the gluon contribution to the nucleon spin from a fit to the existing inclusive data for the proton, deuteron and neutron spin-dependent

structure functions. According to the Altarelli-Parisi evolution equations the spin-dependent structure functions obtain a Q^2-dependence due to a possibly non-zero polarized gluon contribution. Recently, a value for $\Delta G = 0.63^{+0.20}_{-0.19}$ at $Q^2 = 1$ GeV^2 was determined in Ref. [11] from a fit to world data.

A more direct determination of the gluon polarization has been suggested in Ref. [12]. Photon-gluon fusion events can be identified by observing a pair of light hadrons with relatively large transverse momentum P_T. At HERMES [13] such an analysis was pioneered by searching for oppositely charged pion pairs with $P_T > 0.5$ GeV. The observed asymmetry could be related - in a model-dependent analysis - to a value of the gluon polarization of $\Delta G/G = 0.41 \pm 0.18\ (stat) \pm 0.03\ (syst)$. The model dependence due to the difficulty to estimate QCD Compton contribution is not contained in the margins of uncertainty.

The value of ΔG found in the three analyses mentioned above suggests that the gluons are positively polarized in the proton. However, the uncertainties involved are still very large. In order to improve the precision by which this quantity is known, quasi-real photo-production of charmed hadrons can be studied. This is the subject of next section.

2.3 Quasi-real photo-production

For DIS measurements the detection of the scattered lepton is needed. Events in which the beam leptons are scattered over an angle so small that the particles do not enter the HERMES acceptance are labeled as quasi-real photo-production. Experimentally, the events correspond to photo-production as no scattered lepton is observed. On the other hand, the data may actually correspond to DIS events at very low Q^2, which explains the label 'quasi-real' when identifying such events. Due to the steep rise in cross section towards lower Q^2 values the yield for quasi-real photo-production is considerably increased as compared to semi-inclusive deep-inelastic scattering. However, for such events less information on the event kinematics is available. In photo-production a beam of real photons, which thus only have a transverse polarization component, is used. In contrast to this, the virtual photons emitted by the lepton beam at HERMES have both a transverse and longitudinal component. The Q^2 spectrum of the virtual photon does, however, extend to $Q^2 = 0$, i.e. the Q^2 value corresponding to real photons.

In the quasi-real photo-production regime, i.e. very low Q^2, various processes may contribute to the cross section for producing a given particle. In leading order, two types of processes can contribute: direct photon processes, where the photon interacts

with the nucleon as a bare photon, and hadronic photon processes, where the photon interacts with the proton via hadronic interactions, for example, diffractive processes. Depending on the scale set by the mass of the charm quark perturbative calculations are possible. Photon-gluon fusion is an example of an direct perturbatively calculable process in which a single gluon is exchanged. The fluctuation of a (virtual) photon into a $q\bar{q}$ pair is an example of the later process, which can also be calculated perturbatively provided the transverse momenta of the quarks with respect to the photon direction is large enough. Below this scale no perturbative calculations are possible and we enter the non-perturbative QCD domain, where model estimates are used to evaluate the cross section. The cross section for photo-production in the non-perturbative low-P_T regime is usually approximated by taking the incoherent sum of various direct processes (like DIS, photon-gluon fusion and QCD Compton), Vector Meson Dominance (VMD) contributions, and the anomalous photon process.

In the following subsections each of these processes are discussed separately. The discussion is partially focused on the way the processes are programmed in PYTHIA [14, 15], the Monte Carlo code which is mostly used to correct and interpret quasi-real photo-production data. Furthermore, the focus is on charm production, as charm production is used to identify the photon gluon fusion process, while hyperon production is an important source of background.

2.3.1 Open charm production

In open charm photo-production the c and $\bar{c}$ quarks fragment separately into hadrons that either contain a c or $\bar{c}$ quark. This is in contrast to J/Ψ photo-production where a $c\bar{c}$ bound state is produced (the J/Ψ meson), and which is denoted as hidden charm production. In hidden charm production an additional gluon has been exchanged to form the $c\bar{c}$ bound state. Therefore, one cannot simply assume that photon-gluon fusion is the dominant production process, which makes J/Ψ detection a less suitable tool to study photon-gluon fusion [16]. Open charm production, on the other hand, is thought to be a cleaner probe of photon-gluon fusion as no additional gluon is needed. Nevertheless, also in this case contributions from various other mechanisms need to be considered. In this subsection, an overview is given of these processes with emphasis on mechanisms that may contribute to Λ_c^+ photo-production, on which subject experimental data are presented in this thesis.

Photon-gluon fusion

In photon-gluon fusion the virtual photon fluctuates into a $q\bar{q}$ pair of which one quark couples to a gluon in the target. This means that PGF events are sensitive to the gluon distribution G. The cross section for the photo-production of $c\bar{c}$ pairs can be written as a convolution of the cross section for the hard photon-gluon scattering subprocess $\gamma g \to c\bar{c}$ and the gluon structure function $G(x_g, \hat{s})$. Hence, the quasi-real photo-production cross section σ for open charm can be expressed as

$$\sigma^{\gamma N \to c\bar{c}}(\nu) = \int_{4m_c^2}^{2M\nu} d\hat{s}\, \hat{\sigma}^{\gamma g \to c\bar{c}}(\hat{s}) G(x_g, \hat{s}), \tag{2.26}$$

where $\hat{s} = (q+g)^2$ is the energy squared in the photon-gluon center of momentum system with q and g the four-momenta of the photon and gluon. The fractional gluon momentum with respect to the nucleon momentum is denoted by

$$x_g = \hat{s}/2M\nu. \tag{2.27}$$

The integration runs from the threshold energy squared in the center-of-momentum $(2m_c)^2$, with m_c the charm quark mass, up to the maximum $W^2_{max} = M^2 + 2M\nu \approx 2M\nu$ with ν the (real) photon energy.

The cross section difference $\Delta\sigma$ for PGF with parallel and anti-parallel orientations of the target spin and fixed beam spin is given by

$$\Delta\sigma^{\gamma N \to c\bar{c}}(\nu) = \int_{4m_c^2}^{2M\nu} d\hat{s}\, \Delta\hat{\sigma}^{\gamma g \to c\bar{c}}(\hat{s}) \Delta G(x_g, \hat{s}). \tag{2.28}$$

In the photo-production limit $Q^2 \to 0$ the hard scattering cross sections $(\Delta)\sigma$ can be written in leading order QCD as [17, 18]

$$\hat{\sigma}(\hat{s}) = e_c^2 \frac{2\pi\alpha\alpha_s(\hat{s})}{\hat{s}} [-\beta(2-\beta^2) + \frac{1}{2}(3-\beta^4)\ln\frac{1+\beta}{1-\beta}], \tag{2.29}$$

$$\Delta\hat{\sigma}(\hat{s}) = e_c^2 \frac{2\pi\alpha\alpha_s(\hat{s})}{\hat{s}} [-3\beta + \ln\frac{1+\beta}{1-\beta}], \tag{2.30}$$

where $\beta = \sqrt{1 - 4m_c^2/\hat{s}}$ is the center of momentum velocity of the charm quark, α and α_s are the electromagnetic and strong coupling constants, and $e_c = \frac{2}{3}$ is the charge of the charm quark.

In Ref. [19, 20] higher order contributions to the PGF charm cross section have been calculated. Significant corrections near the threshold of the partonic subprocess

are reported, but the kinematic dependence of the corrections is similar to that of the LO cross section. Hence, in practice a fudge factor (K-factor) is often used to correct the LO cross sections.

It is possible to relate the polarized gluon density ΔG to an asymmetry that can be measured, provided charm events produced by the PGF process are identified. In that case the measured asymmetry is related to the basic cross sections involved according to

$$A_{\gamma N}^{\mathsf{PGF}} = \frac{\Delta\sigma^{\gamma N\to c\bar{c}}}{\sigma^{\gamma N\to c\bar{c}}} \approx \frac{\Delta\sigma^{\gamma g\to c\bar{c}}}{\sigma^{\gamma g\to c\bar{c}}}\frac{\Delta G}{G} = \hat{a}_{\mathsf{PGF}}\frac{\Delta G}{G}, \tag{2.31}$$

where the second (approximate) equality only holds for a small $\hat{s}$ bin (as applies to HERMES[1]) within which ΔG nor G are expected to vary. In the r.h.s. the partonic level asymmetry $\hat{a}_{\mathsf{PGF}}$ is implicitly defined. Calculations of expected PGF asymmetries have been performed in LO (Ref. [21, 22]) as well as in approximate NLO (Ref. [23]).

Another characteristic that distinguishes PGF events from (background) photo-production processes is the, on average, higher transverse momentum of the final state particles. Possible backgrounds to this process come from DIS involving quarks with high intrinsic transverse momentum, radiation of soft gluons by the struck quark, other hard subprocesses (QCD Compton) or accumulation of P_T in the fragmentation process. Hence, Monte Carlo simulations are needed to identify the kinematical domain where PGF dominates. As was shown in subsection 2.2.3 an analysis of data collected on a longitudinally polarized ^{1}H target in which the (two) final state particles were required to have high transverse momenta led to a first determination of the gluon polarization.

Intrinsic Charm

In principle intrinsic charm quarks in the nucleon may also contribute to quasi-real photo-production of charmed hadrons. A model in which charm is an intrinsic constituent of the proton has been proposed as a way to explain the charm cross sections in hadron-production experiments for large values of x [24]. In this model a charm component with probability β^2 is added to the proton wave function, i.e. $|p\rangle = \alpha|uud\rangle + \beta|uudc\bar{c}\rangle$. In the model the quark and anti-quark distributions peak at x values of about 0.25. When compared initially to EMC data at high x some indications for intrinsic charm were found. However, after data from the ZEUS and H1 experiments

[1]The $\hat{s}$-range covered by the HERMES experiment starts at the Λ_c^+ production threshold at 4.15 GeV and ends at the maximum value of 7.24 GeV that can be reached. As the photo-production cross section rises steeply with $\hat{s}$, effectively the $\hat{s}$-bin has a size of only about 1-2 GeV.

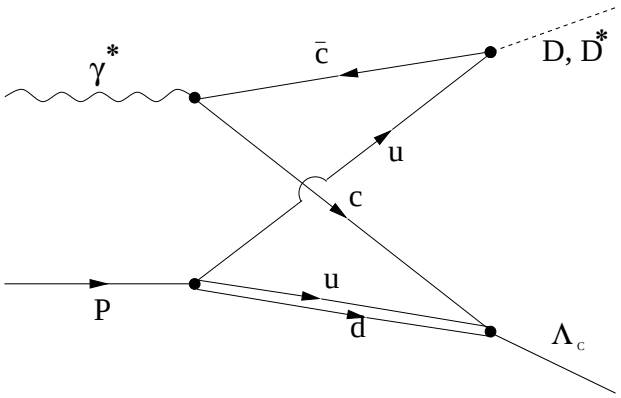

Figure 2.2: *Quark Interchange process contributing to the production of a Λ_c baryon in association with a $\bar{D}$ or $\bar{D}^\star$ meson.*

became available and NLO calculations became possible, intrinsic charm was no longer needed to get agreement between data and calculations [25]. Thus, a possible charm contribution to the proton wave function is now usually neglected, as we will also do in the present study.

Threshold production

In the threshold regime, multi-parton subprocesses, which are normally suppressed by powers of $1/m_q^2$, might dominate the contributions of the leading-twist single-gluon subprocesses due to phase-space suppression [26]. In contrast to charm production at high energy all the target nucleon constituents may act coherently in heavy quark production near threshold. In Ref. [26] it is shown that a model that takes such an enhancement due to phase-space effects into account reproduces a measurement of the elastic J/Ψ photo-production cross section near threshold (E_γ=12 GeV). Such calculations are presently not available for Λ_c^+ threshold production, but the process may play a role as well.

Quark Interchange

In Ref. [27], the Quark Interchange (QI) process, illustrated in figure 2.2, was introduced as a possible contamination to charm production via the PGF process. In Ref. [27] the exclusive reaction

$$\gamma + p \rightarrow \bar{D}(or\bar{D}^\star) + \Lambda_c \tag{2.32}$$

is considered. In this process a $c\bar{c}$ pair with small transverse momentum with respect to the direction of the photon is created. While the $\bar{c}$ quark forms a $\overline{\mathrm{D}}$ or $\overline{\mathrm{D}}^\star$ meson, the c quark combines with the (ud) di-quark remnant of the proton to give a Λ_c baryon. No explicit gluon exchange contributes to this process. The authors of Ref. [27] do not derive a cross section expression for the QI process, but conclude that the double spin

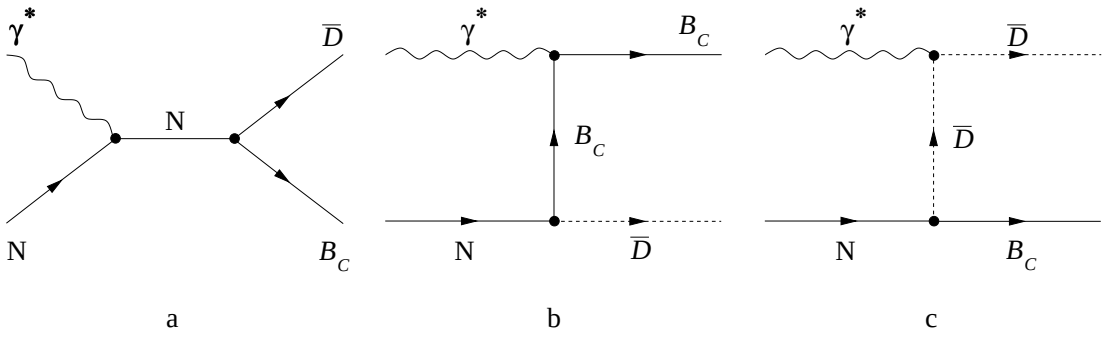

Figure 2.3: *Feynman diagrams which are evaluated for the process* $\gamma + N \rightarrow B_c + \bar{D}$ *in the framework of the* ELA *calculation. The diagrams a, b and c represent the s-, u- and t-channel exchange, respectively.*

asymmetry is possibly affected by this process. The double spin asymmetry contribution of the QI process is estimated to be 12%[2].

The QI process might be distinguished from PGF by requiring large transverse momenta of the reconstructed charmed final state particles, i.e. the $\bar{D}$-meson or the Λ_c baryon. This difference originates from the required coupling of the u quark to the $\bar{c}$ quark to form a $\bar{D}^{(\star)}$ meson, and the ud di-quark with the c quark to form a Λ_c^+ baryon. As neither the u (nor the ud) quark generally has a high transverse momentum each of the charm quarks should also not carry a large P_T as this would prevent the formation of the final $\bar{D}$ and Λ_c^+ hadrons. Hence, by experimentally requiring a high P_T value the contribution of the QI process should be suppressed. In the absence of a cross section calculation for this process the amount of suppression (as a function of P_T) cannot be evaluated at present.

Effective Lagrangian Approach

An alternative method to describe quasi-real photo-production of Λ_c^+ baryons close to threshold is presented in Ref. [28]. Instead of starting from the interaction at the partonic level (as is done in the leading order QCD calculation of the PGF process) an effective Lagrangian approach (ELA) is used for the calculation of exclusive associative photo-production of charmed particles. In the ELA calculation the interactions are treated at the baryon-meson level. The authors of Ref. [28] consider the exclusive reaction $\gamma + p \rightarrow B_c + \bar{D}$, with the charmed baryon $B_c = \Lambda_c^+$ or Σ_c^+. Three matrix elements are calculated, corresponding to the s-, u- and t-channel exchange contribu-

[2]In Ref. [27] the sign convention of the asymmetry is inverted.

tions (see figure 2.3), with s, u and t denoting the Mandelstam variables $s = (k + p_1)^2$, $u = (k - p_2)^2$ and $t = (k - q)^2$. For the pseudoscalar meson-baryon vertex they find

$$\begin{aligned} M_s &= e\,\frac{g_{NB_{\mathrm{C}}D}}{s-m^2}\,\bar{u}(p_2)\gamma_5(\hat{k}+\hat{p}_1+m)\,[Q_N\hat{\epsilon}-\frac{\hat{\epsilon}\hat{k}}{2m}\kappa_N]u(p_1)\,, \\ M_u &= e\,\frac{g_{NB_{\mathrm{C}}D}}{u-m^2}\bar{u}(p_2)\,[Q_{\mathrm{C}}\hat{\epsilon}-\frac{\hat{\epsilon}\hat{k}}{2M}\kappa_{\mathrm{C}}](\hat{p}_2-\hat{k}+M)\gamma_5 u(p_1), \\ M_t &= 2e\,Q_D\frac{g_{NB_{\mathrm{C}}D}}{t-M_D^2}\,\hat{\epsilon}\cdot\hat{q}\bar{u}(p_2)\gamma_5 u(p_1), \end{aligned} \tag{2.33}$$

where k, q, p_1 and p_2 are the four momenta of the γ, $\bar{D}$, N and B_{C}, ϵ is the four vector representing the photon polarization and $m(Q_N)$, $M(Q_{\mathrm{C}})$ and $M_D(Q_D)$ are the masses (electric charges) of the nucleon, the charmed baryon and the D-meson, respectively. The constant $g_{NB_{\mathrm{C}}D}$ is the coupling constant describing the strength of the vertex for nucleon-charmed baryon-D meson interactions, while κ_N or κ_{C} are the nucleon and charmed baryon anomalous magnetic moments. A priori no knowledge is available on the value of $g_{NB_{\mathrm{C}}D}$ or κ_{C}, which are thus treated as (more or less) free parameters in the ELA calculations. It can be seen from equations 2.33 that the cross section scales linearly with $g^2_{NB_{\mathrm{C}}D}$, while the dependence on κ_{C} is much weaker.

The use of the effective Lagrangian approach as a low-energy approximation of QCD is well established for threshold calculations involving light quarks. It is used in Chiral Perturbation Theory for instance. However, its application to the charm sector is not unambiguous as the mass of the charm quark cannot be neglected as can be done for the u and d quarks in the case of π threshold production. Nevertheless, the approach of Ref. [28] might be useful for us as it provides an estimate of the energy dependence of the Λ_c^+ photo-production process including (effectively) many higher-order processes which at present are difficult to incorporate in a QCD calculation.

2.3.2 Hyperon production

The internal spin structure of the Λ hyperon is of importance in order to reach a full understanding of the spin structure of hadrons in general. The comparison between the spin structure of the nucleon and the Λ hyperon can be used to test symmetry relations among quarks. In the naive quark model, for instance, the spin of the Λ is carried solely by the s quark, while a SU(3) model suggests that only 60% is carried by the s and $\bar{s}$ quarks [29]. The rest of the spin is supposedly carried by the u and d quarks. The HERMES collaboration has studied this problem by measuring the $u \to \Lambda$ spin transfer probability [30].

A problem in the interpretation of these data is, however, that the Λ can also be a decay product of the heavy (Ξ and Σ) hyperons, which means that the contribution from these heavy hyperons to the production mechanism needs to be determined first. In Ref. [31] it was found, for instance, from a Monte Carlo study that at $z < 0.65$ about 60% of the Λ hyperons may come from a heavy hyperon. This falls to about 30% if $z > 0.75$. Furthermore, it was found that the majority of the Λ hyperons at $x_F > 0$ do not contain the struck quark. For the Λ hyperons that do contain the struck quark the simulations seem to imply that the Λ polarization is mainly due to u quarks at $z \approx 0.6$, while the s quarks are found to be dominant for $z > 0.8$. In order to verify these simulations the relative contribution of the Σ^0, $\Sigma^\star$ and Ξ hyperons to Λ^0 production needs to be measured, and compared to the Monte Carlo predictions.

Another interesting aspect of hyperon production is revealed by measuring their cross section asymmetry with respect to the target spin orientation. Depending on the production mechanism assumed such measurements might provide information on the sea quark polarization as some of the hyperons are all-sea[3] objects.

2.3.3 Light quark production

In this subsection we discuss several light quark processes that might contribute to the $\Lambda\pi X$ final states studied in this thesis. The leading order DIS contribution is vanishing in the limit of $Q^2 \to 0$, and hence only gives a small contribution to quasi-real photo-production. In the PYTHIA calculation this is achieved through the introduction of a phenomenological suppression factor, i.e. a Sudakov form factor.

Light quarks can also be produced in photon-gluon fusion (PGF), which is modeled using its partonic cross section (see [15]), and the QCD Compton process, which both are direct interactions of the photon with a partonic constituent of the nucleon.

The VMD cross section, which may also contribute, is written as a sum over low mass vector meson states:

$$\sigma^{\gamma^\star p}_{VMD} = \sum_{V=\rho^0,\omega,\phi,\mathrm{J}/\Psi} \frac{4\pi\alpha}{f_V^2}\left(\frac{m_V^2}{m_V^2+Q^2}\right)^2 \sigma^{Vp}, \tag{2.34}$$

where f_V^2 and m_V are the appropriate photon vector meson coupling constants and masses, and σ^{Vp} the vector meson photo-production cross section.

[3]Here it is meant that the particle does not contain quark flavors that are also present in the target nucleon as a valence quark, i.e. u- or d-quarks.

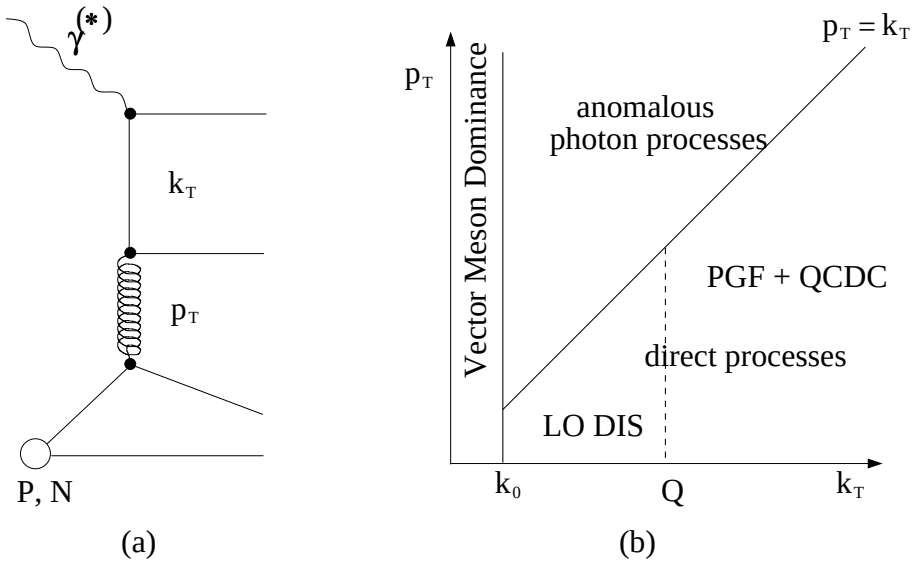

Figure 2.4: *(a) Diagram for a hard γp process with two relevant momentum scales. (b) The allowed phase space for the various processes contributing to quasi-real photoproduction. (Figure taken from [15])*

The anomalous photon process which resembles the VMD process without an explicit vector meson intermediate state, is calculated through:

$$\sigma^{\gamma p}_{anom} = \frac{\alpha}{\pi} \sum_q e_q^2 \int_{k_0} \frac{d\, k_T^2}{k_T^2} \sigma^{(q\bar{q})p}, \tag{2.35}$$

and depends on the intrinsic transverse momentum k_T of the partons in the photon with a lower cut off at k_0. This process can also lead to the production of Λ^0 hyperons if one of the quarks of the quark-antiquark pair originating from the photon interacts with the quarks in the proton.

In order to avoid double counting two scales are introduced in PYTHIA that classify the processes. The intrinsic k_T of the partons in the photon, which is related to the $\gamma \rightarrow q\bar{q}$ vertex, and the intrinsic p_T of the involved parton in the nucleon are used. As can be seen from figure 2.4 depending on the value of k_T certain processes are assumed to be dominant when simulating the requested hadronic final state in quasi-real photoproduction.

2.3.4 Discussion

This chapter mainly served to provide a framework for the interpretation of the Λ_c^+ yields and asymmetries which are presented in chapter 4. Many processes may contribute to charm production in general and Λ_c^+ quasi-real photo-production in particular. However, in leading order QCD calculations, only the PGF induced Λ_c^+ yield is included. On the other hand, the data may contain many NLO and non-perturbative QCD effects. For this reason, the ELA calculations or the QI process are also considered (when possible) as these calculations might effectively include some of these non-leading processes. But as it is unclear how the various available calculations should be combined, and in order to ensure an unambiguous interpretation of the data, it was decided to compare to calculations based on the LO QCD PGF process when discussing the data in chapter 4.

Chapter 3

The HERMES experiment

For a clear understanding of the boundary conditions to which the design of the Lambda Wheels was subjected (chapter 5) and to set the framework for the analysis described in this thesis (chapter 4) the HERMES experiment is briefly described in this chapter. The HERMES experiment has been designed to study the spin structure of the nucleon by scattering polarized leptons off a (fixed) polarized target. It is situated in the East-section of the HERA lepton-proton collider facility of DESY in Hamburg. HERMES only uses the lepton beam which is scattered from polarized atomic nuclei that are injected into a target cell internal to the beam. This is in contrast to the ZEUS and H1 experiments which use both beams in collider mode, and the HERA-B experiment which uses the proton beam only.

The HERA storage ring is described in section 3.1, and the polarized HERMES target in section 3.2. The HERMES spectrometer is the subject of section 3.3.

3.1 The HERA storage ring

The lepton storage ring of HERA at DESY can either store electrons or positrons with an energy of 27.5 GeV and has a length of 6.3 km. At the start of a fill of the lepton ring typical beam currents of 30 to 40 mA are achieved. The life time of one fill is typically 12 hours. At about 10 mA the remaining lepton current is dumped. Due to the Sokolov-Ternov effect [32] a transverse polarization of the leptons is built up. In order to obtain the longitudinal polarization utilized in the HERMES experiment spin rotators are placed in front of and behind the HERMES experiment. A mean polarization of about 40 to 60 % is achieved with a rise time of about 22 minutes. The value of the polarization is measured with both a longitudinal and a transverse polarimeter. The transverse polarimeter [33] is located close to the west section of HERA. It measures an up-down asymmetry of photons Compton scattered from the beam leptons with

a systematic uncertainty of 3.4 %. The measured asymmetry is proportional to the beam polarization. The longitudinal polarimeter [34] is situated near the HERMES interaction point and uses the spin dependent angular distribution of the Compton cross section for longitudinally polarized leptons. The longitudinal polarization of the lepton beam is measured with a fractional systematic uncertainty of 1.6 %. Furthermore, the ratio of the polarizations measured with the longitudinal and transverse polarimeters is found to be about 1.02, i.e. the two polarimeters yield consistent results within their respective systematic uncertainties.

3.2 The internal gas target

The advantage of the HERMES experimental set-up as compared to other polarized DIS facilities is the possibility to use an internal target in combination with a storage cell. As a result undiluted highly polarized gases could be used. In other experiments massive polarized targets are used with large dilution factors, as hydrogen polarization is always obtained in combination with another atom.

At HERMES the gas atoms are brought into the middle of a tube with an elliptical cross section through which the lepton beam passes. This tube is known as the target cell and is 40 cm long. If it is cooled down to 100 K, target thicknesses of about 10^{14} nucleons/cm^2 are obtained for polarized hydrogen and deuterium, and 10^{15} nucleons/cm^2 for polarized ^{3}He gas. If unpolarized gas atoms are used as target the thickness can be increased to about 10^{16} nucleons/cm^2. This mode of operation has a large impact on the lepton beam life time, i.e. it is reduced to a few hours or less. It has therefore been used only at the end of a fill in order to collect a large sample of unpolarized DIS data in a relatively small amount of time. The analysis described in this thesis is, however, limited to the polarized hydrogen and deuterium data collected in the years 1997-2000.

3.3 The HERMES spectrometer

The HERMES experiment is built around a forward angle spectrometer mostly designed for studying semi-inclusive DIS on polarized (internal) targets [35]. The spectrometer is divided in a front and backward part with respect to the spectrometer magnet. The dipole magnet has an integrated field of $\int B \cdot dl = 1.3$ Tm. The tracks reconstructed in the front and backward regions are combined in the middle of the magnet, enabling a momentum measurement based on the measured bending of the track. The momentum

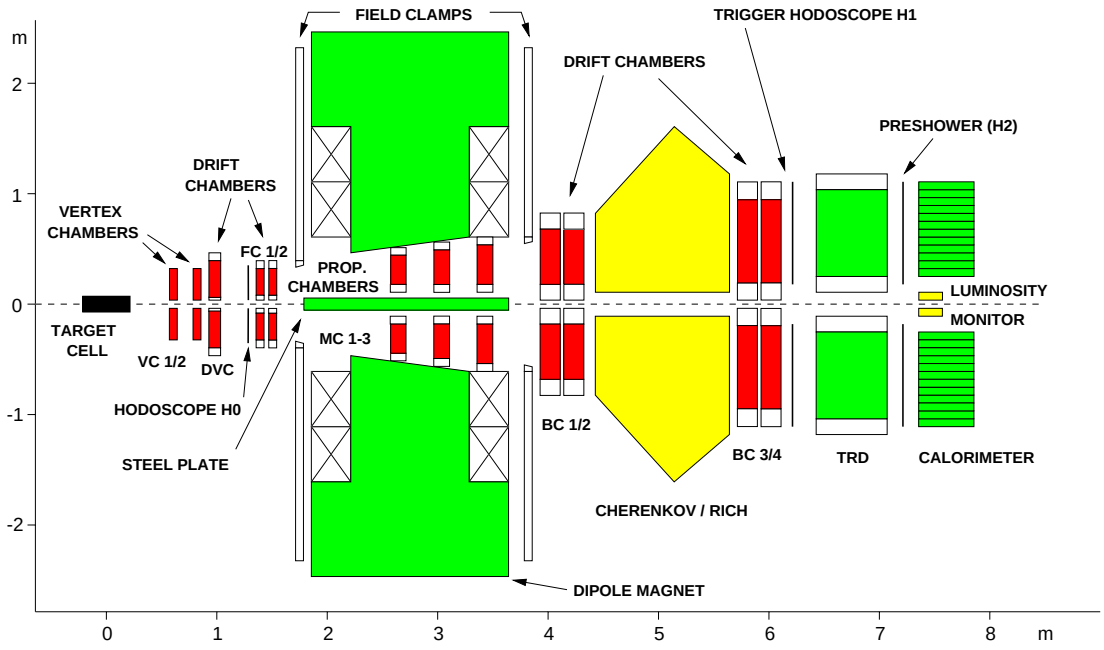

Figure 3.1: *Side view of the* HERMES *spectrometer.*

resolution $\Delta p/p$ of the scattered lepton is about 1-3 % and the angular resolution is better than 0.6 mrad. The spectrometer consists of an upper and lower part which are mirror images of each other. The vertical acceptance has a gap due to a steel plate that is needed to shield the lepton beam from the magnetic field of the spectrometer magnet. The acceptance of the experiment in the horizontal and vertical direction is $|\theta_x| \leq 170$ mrad and 40 mrad $\leq |\theta_y| \leq 140$ mrad, respectively. The spectrometer acceptance and the beam energy of 27.5 GeV result in an accessible kinematic range limited to $0.02 < x < 0.8$ and $0.2\ \text{GeV}^2 < Q^2 < 20\ \text{GeV}^2$.

The tracking chambers are mostly normal drift chambers. They all have their wires either oriented vertically, or tilted either +30 ° or -30 ° with respect to the vertical axis. The Vertex Chambers [36] (VC), however, are composed of 2 sets of 3 microstrip gas counters. In the front region the Drift Vertex Chambers (DVC) and the Front Chamber (FC) are both drift chambers composed of 6 planes. The Magnet Chambers (MC) are used for low momentum tracks that do not reach the Back Chambers (BC) and the particle identification detectors. The front tracking is based on a combination of VC, DVC and FC information. While the VC provided the most precise tracking information it had to be removed in 1998 due to severe radiation damage encountered when the HERA beam was lost in the vicinity of HERMES.

The remainder of the section is organized as follows. First the detectors used for

particle identification are described in subsection 3.3.1. The luminosity monitor used for the measurement of the beam luminosity is the subject of subsection 3.3.2, and in the last subsection the HERMES trigger and the data acquisition system are introduced.

3.3.1 Particle identification

Initially, particle identification at HERMES was mainly designed to achieve a very good lepton-hadron separation. This was accomplished with a threshold Čerenkov detector, a transition radiation detector (TRD), a pre-shower counter and an electromagnetic calorimeter. With the installation of a Ring Imaging Čerenkov Chamber in 1998, which replaced the threshold Čerenkov detector, it became possible to identify πs, Ks and protons in a large momentum range [37].

The threshold Čerenkov counter detects Čerenkov light emitted if the speed of a particle is above the speed of light in the gas medium, which is given by the refractive index n of the medium $v_t = c/n$. For particles with a different mass m a different threshold momentum results, which is given by

$$p_t = \frac{\gamma_t mc}{n} \tag{3.1}$$

with $\gamma_t = n/\sqrt{n^2-1}$. It is thus possible to identify hadrons of the smallest mass, i.e. πs, in the momentum range between the threshold for a π Čerenkov signal (3.9 GeV)[1] and the threshold for K detection (13.7 GeV). Above the K threshold it is not possible to separate πs and kaons. It is, however, possible to minimize proton contamination up to the proton threshold (26.2 GeV). With the inclusion of the RICH also the angle of the Čerenkov radiation is measured. This angle θ_C is given by

$$\cos\theta_C = \frac{1}{\beta n} \tag{3.2}$$

with $\beta = \frac{v}{c}$ the relative velocity of the particle. This angle is determined from the signals of a matrix of 1934 photomultiplier tubes per detector half which detect the Čerenkov radiation reflected in a mirror array. The RICH detector enables π, K and p identification in the momentum range from 2 GeV to 15 GeV [38]. The lower limit could be achieved by also using aerogel as refractive material. In the case of the threshold Čerenkov counter only a N_2-C_4F_{10} gas mixture was used.

The transition radiation detector (TRD) consists of a box filled with polyethylene/polypropylene fibers containing Xe(90%)/CH_4(10%) gas. The numerous boundaries between the materials with a different dielectric constant result in transition radiation

[1] Values are given for the 1997 set up.

when a high energy particle is propagating through it, which is measured (mainly X-rays) with a multiwire proportional counter. At HERMES $\gamma > 6000$ for positrons or electrons while hadrons have $\gamma < 200$. A lower Lorentz factor γ results in a lower energy of the transmitted photons. Therefore, a measurement of the radiated energy enables a clear distinction between leptons and hadrons.

The pre-shower detector consists of 42 plastic scintillator modules with a width of 9.3 cm each, a length of 91 cm and a thickness of 1 cm. The modules are placed in two rows such that an overlap of 1.5 mm exists in between two adjacent modules. The modules are read out with photomultiplier tubes with a diameter of 5.2 cm. The difference in the longitudinal shower profile between leptons and hadrons results in a pre-shower value. The combination of the pre-shower detector and the calorimeter detector signals can be used to improve the lepton-hadron separation.

Each half of the calorimeter [39, 40] consists of (42×10) radiation resistant F101 lead glass blocks. A block measures 9×9 cm^2 and is 50 cm long. Each block is coupled to a 7.62 cm photomultiplier using silicone glue. In order to prevent radiation damage during injection and ramping of the beam the calorimeter can be moved away from the beam. The energy resolution of the calorimeter is given by [40]

$$\frac{\sigma(E)}{E}[\%] = \frac{10.0 \pm 2.0}{E[\mathrm{GeV}]} + \frac{5.1 \pm 1.1}{\sqrt{E[\mathrm{GeV}]}} + (2.0 \pm 0.5) + \frac{10.0 \pm 2.0}{E[\mathrm{GeV}]}\,. \tag{3.3}$$

The energy response to electrons is linear within 1 % from 1 GeV to 30 GeV.

Lepton/Hadron separation

The outputs of the pre-shower detector (Pre), the Čerenkov detector (Cer) and the calorimeter (Cal) are combined into a quantity PID_3 which is used to separate leptons from hadrons

$$PID_3 = \log_{10}\left[\frac{(P^e_{Pre}P^e_{Cer}P^e_{Cal})}{(P^h_{Pre}P^h_{Cer}P^h_{Cal})}\right]. \tag{3.4}$$

Here P^k_l is the conditional probability that a particle of type k gave a signal in the detector l. For the transition radiation detector TRD a separate PID variable is made

$$PID_5 = \log_{10}\left[\frac{(P^e_{TRD})}{(P^h_{TRD})}\right], \tag{3.5}$$

which in the analysis is usually added to PID_3 and denoted as PID (without subscript). Hadrons or leptons are identified by imposing requirements on the PID variable. Application of this PID scheme gives a lepton detection efficiency over 97% with a hadron contamination below 0.01%. The hadron detection efficiency is 99% with a lepton contamination below 0.6%.

3.3.2 Luminosity monitor

The luminosity of the experiment is measured by detecting elastic scattering of the beam leptons from electrons of the target atoms. The scattered and ejected electrons are detected in a calorimeter on either side of the beamline, 7.2 m downstream of the center of the target cell. The calorimeter consists of $NaBi(WO_4)_2$ crystals with a very high radiation tolerance. Like the calorimeter these crystals are moved away from the beam during injection. The energy resolution of the calorimeter is [41]

$$\frac{\sigma(E)}{E}[\%] = \frac{4.3}{E[\mathrm{GeV}]} + \frac{9.3}{\sqrt{E[\mathrm{GeV}]}} + 0.3, \tag{3.6}$$

for electron energies between 1 and 6 GeV.

In practice the luminosity follows from the luminosity trigger rate per burst according to

$$\mathcal{L} = C_{Lumi} f_l \dot{L} \Delta_{Burst}, \tag{3.7}$$

where the luminosity constant C_{Lumi} takes into account the acceptance of the detector and the cross sections for Møller scattering or Bhabha scattering and pair annihilation, f_l is the ratio of nucleons to atomic electrons which is introduced to arrive at a luminosity per nucleon, and $\dot{L}$ is the frequency of coincident hits in the time interval of one burst Δ_{Burst}. In [41] the reciprocal value of the luminosity constant was determined to be $C^{-1}_{Lumi,e^+} = 2.22 \pm 0.14$ μb for a positron beam, and $C^{-1}_{Lumi,e^-} = 3.59 \pm 0.22$ μb for an electron beam. For the effective luminosity $\mathcal{L}_{eff} = \eta_{Dead}\mathcal{L}$ a correction, on burst level, for the dead time of the data acquisition system is applied.

3.3.3 Trigger system and data acquisition

A first level trigger system is used for the selection of the events to be recorded. The physics trigger for DIS and SIDIS events is provided by requiring hits in all the hodoscopes and an energy deposit in two adjacent columns of the calorimeter above 1.4 GeV. For quasi-real photo-production events a separate trigger is needed as no scattered positron is detected. This is accomplished by the requirement of at least one track in both the upper and lower detector halves. For the identification of these tracks the three hodoscopes and the first backward drift chamber are used. For each of the triggers it is also required that they are in coincidence with the accelerator bunch crossing signal.

The different detectors have their own read out system that also acts as a buffer before the data are sent to the on-line work stations. Here the raw data (in EPIO format [42]) are stored to disk and tape simultaneously. While the detectors are read

out and the digitization of the data is in progress no new triggers can be accepted. As a consequence a dead-time is introduced. If this dead-time becomes too high some of the triggers can be pre-scaled to reduce the dead-time. Part of the data is reconstructed 'on the fly' in order to monitor the functioning of the HERMES detector during data taking. Besides the information retrieval following the occurence of a trigger, online information is recorded at fixed time intervals. This information normally doesn't fluctuate during small time intervals and is called slow-control information. It contains almost constant control variables of the various detectors, such as high voltages and temperatures. The slow-control data are continuously monitored every 10 seconds of a run.

In order to analyze the data the event information is decoded by the Hermes Decoder Code (HDC) and written in the ADAMO [43] format. The Hermes Reconstruction Code (HRC) tracks the events in the front and the back region, and combines both tracks. Besides tracking, HRC also determines the momenta of the particles and combines the PID information and the measured amount of energy deposited in the calorimeter with reconstructed full tracks. After HRC part of the decoded data is stripped and a μDST[2] is made containing the event information in a format suitable for physics analyzes. This information is the starting point for the tracking and analyzis work discussed in chapter 4 and 6.

[2]The Data Summary Tape contains only information needed for a physics analysis.

Chapter 4

Λ_c^+ photo-production

4.1 Introduction

The results of experiments, in which longitudinally polarized electrons were scattered off quarks in longitudinally polarized nucleons (DIS) have shown that the nucleon spin is only partly carried by quarks. It has been suggested that orbital angular momentum and spin polarization of gluons are possibly also accounting for part of the nucleon spin. The (polarized) deep-inelastic lepton scattering experiments that led to this conclusion are reviewed at various places. [44, 45, 46]

In order to measure the orbital angular momentum of quarks and gluons in the nucleon in principle use can be made of the Deeply-Virtual Compton Scattering process [47, 48], a subject not further discussed in this thesis.

For the measurement of the gluon polarization, a process has to be identified in which the probe (effectively) couples to a single gluon. Such a process is photon-gluon fusion (PGF), of which the corresponding diagram is shown in fig. 4.1. The photon γ interacts with a gluon g from the target by exchange of a (virtual) quark, resulting in a quark-antiquark pair. These particles have opposite momentum in the center of momentum system of the photon and the gluon. The cross section asymmetry of PGF-events with respect to the target-spin orientation is related to the gluon polarization [21, 22] by (see Eq. 2.31)

$$A_1^{PGF} = \frac{\int \mathrm{d}\hat{\sigma}\ \hat{a}_{\mathsf{PGF}} \Delta G}{\int \mathrm{d}\hat{\sigma}\ G} \simeq \hat{a}_{\mathsf{PGF}} \frac{\Delta G}{G}\,, \tag{4.1}$$

where $\hat{a}_{\mathsf{PGF}}$ is the partonic level asymmetry, $\hat{\sigma}$ the parton level cross section for this process, and $(\Delta)G$ the (polarized) gluon distribution. The integral runs over all kinematic variables covered by the acceptance of the experiment. If the variation of $\hat{a}_{\mathsf{PGF}}$, ΔG and G within the acceptance is small the second equality holds (see equation 2.31). For light

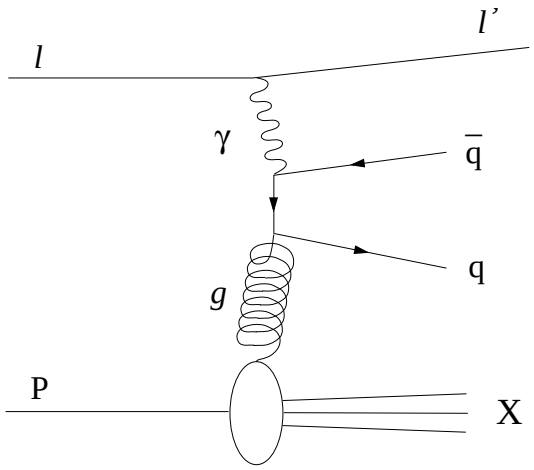

Figure 4.1: *Leading order $q\bar{q}$-production via the photon gluon fusion process in electron scattering off a proton.*

quarks the partonic level asymmetry is negative, while it becomes positive for charm and heavier quarks [22]. Consequently, the polarized gluon distribution is measurable if PGF events can be isolated from the quasireal photoproduction background. This is not easy as the background at the low Q^2 values probed in photoproduction is roughly two orders of magnitude larger than the PGF yield [49], if no further requirements are imposed. Therefore, an analysis method or experimental technique is needed that enables us to distinguish between PGF and quasireal photoproduction events. Two such methods are known; in one the relatively high transverse momentum of the final state hadrons in the PGF process is used [13], while in the other the occurrence of charmed hadrons in the final state is used as a tag of PGF events. Here it is assumed that the intrinsic charm quark content in the nucleon can be neglected. In this thesis an analysis is presented of data collected at HERMES in which both ideas are combined in an effort to extract information on $\Delta G/G$ from quasireal photoproduction of Λ_c^+ baryons (which have a *udc* quark structure).

After selection of PGF events an asymmetry A can be measured. A_1^{PGF} is related to the measured asymmetry through

$$A_1^{\mathsf{PGF}} = \frac{A}{P_{Target} P_{Beam} D}, \tag{4.2}$$

where D is the depolarization of the virtual photon with respect to the polarization of the incident lepton, while P_{Target} and P_{Beam} are the measured target and beam polarizations, respectively.

In an analysis of data collected on a longitudinally polarized ^{1}H target in which two oppositely charged final state hadrons were required to have high transverse momenta a spin-target asymmetry $A_{||}$ of -0.28 ± 0.12 (*stat*) was measured at HERMES [13]. The

only known process to which a large negative asymmetry can be attributed is the production of light $q\bar{q}$-pairs via PGF. Correction for background processes (such as QCD Compton scattering and processes involving vector mesons) using the PYTHIA Monte Carlo program [50] made it possible to derive a (model dependent) value for $\Delta G/G$ of $0.41 \pm 0.18\ (stat) \pm 0.03\ (syst)$ from these data. It should be noted, though, that the size of the model dependence is difficult to estimate as it relies on the Monte Carlo simulations of the background processes which cannot be easily checked by an independent analysis. The quoted systematic uncertainty of 0.03, therefore only represents the systematic error related to the experiment.

Another signature that can be used to isolate PGF events from the photo-production background is the presence of charm in the final state hadrons. As it is commonly assumed that the nucleon contains no charm quarks, the observation of a charmed hadron is direct evidence of the occurrence of a PGF event, provided that no other production processes occur. However, complications arise from the relatively low value of the center of mass energy at HERMES of $\sqrt{s} = 7.24$ GeV, which is close to the threshold for charm production at 4.15 GeV[1]. However, charm production through different processes such as quark interchange (QI) [27] and exclusive production (i.e. $\gamma + \mathrm{p} \rightarrow \Lambda_c^+ + \overline{\mathrm{D}}^0$) [28] might become important close to threshold (see sect. 2.3).

At HERMES it has been tried to identify PGF events by searching for quasireal photoproduction of charmed mesons such as the $\mathrm{D}^{\star\pm}$ [51] and the D^0 [52] meson. In the first analysis the statistics extracted from the data collected in '96 and '97 on a hydrogen target was insufficient for the determination of an asymmetry. In the second analysis a larger amount of charm events could be extracted by imposing various cuts in the analysis. Similar to this analysis, partial reconstruction of the signal was exploited. Here the decay channel $\mathrm{D}^{\star 0} \rightarrow \mathrm{D}^0\pi^0$ with $\mathrm{D}^0 \rightarrow \mathrm{K}^{\pm}X$ has been used. A spin-asymmetry of $0.71 \pm 0.14\ (stat)$ was evaluated for these events, and from this asymmetry a value of $\Delta G/G = 0.85 \pm 0.17\ (stat) \pm 0.16\ (syst)$ was determined. It should be noted, however, that this analysis has not yet been cross checked and is subject to uncertainties due to use of Monte Carlo programs to determine the relative signal and background contributions.

In the analysis presented in this chapter it is explored whether photoproduction of Λ_c^+ baryons can be used to access PGF. It will be shown that it is possible to reconstruct the Λ_c^+ baryon using the decay channel $\Lambda_c^+ \rightarrow \Lambda^0\pi^+$, which has a branching ratio of only 0.9%. The statistics of the Λ_c^+ peak, however, is low as a combined result of the small charm production cross section, the small branching ratio, and the low HERMES ac-

[1]The center of mass energy gives an upper limit on the energy avialable for a reaction.

ceptance for this event type. Therefore, no viable asymmetry can be extracted from the data contained in the Λ_c^+ peak. The small number of identified Λ_c^+ baryons enables us, however, to estimate the number of Λ_c^+ particles that may be observed in different decay channels.

To increase the statistics needed for a Λ_c^+ asymmetry measurement it has been investigated whether partially reconstructed Λ_c^+ particles [53], i.e. Λ_c^+ events of which one or more of the decay products escape the HERMES acceptance, can be used to determine the asymmetry for Λ_c^+ production. As an example, Λ^0 hyperons coming from the Λ_c^+ via an intermediate Σ^0 are part of the sample, as the γ originating from the Σ^0-decay is not contained in the analysis. The advantage of using partial reconstruction to identify PGF is that the estimated branching ratio for the semi-exclusive channel $\Lambda_c^+ \to \Lambda^0\pi^+X$ is almost a factor 15 larger as compared to the exclusive $\Lambda_c^+ \to \Lambda^0\pi^+$ channel.

While studying the semi-inclusive $\Lambda\pi$ invariant mass spectra it turned out to be possible to reconstruct Ξ and $\Sigma^\star$ hyperons as well using the same data set. This can be understood since the reconstruction of the Ξ and $\Sigma^\star$ hyperons is similar to that of the Λ_c^+ as these particles predominantly decay into a (Λ,π)-pair. As a result it is possible to determine the relative yields and double spin asymmetries for photoproduction of these hyperons. Furthermore, it gives a handle on the kinematic requirements introduced to suppress the background in the partially reconstructed Λ_c^+ particles.

The yields and target-spin asymmetries for the photo-produced Ξ and $\Sigma^\star$ hyperons are also of some intrinsic interest as they provide information on the relative importance of heavier hyperons when studying Λ production. Moreover, the anti-hyperons, which are all-sea particles (see footnote on page 20), may provide information on the sea-quark polarization.

The organization of this chapter is as follows. First the selection criteria applied to the data are discussed, and the kinematics for the reconstruction of photo-produced hyperons is introduced. Next these criteria are applied to the data to arrive at signals for the Ξ and $\Sigma^\star(1385)$ hyperons. After imposing additional requirements a low statistics Λ_c^+ baryon mass spectrum is obtained. Based on this spectrum the Λ_c^+ cross section is determined (section 4.3.3). In the next section (4.4) the yield and double spin asymmetries for photoproduction of the Ξ and $\Sigma^\star(1385)$ hyperons are evaluated. In order to be able to determine similar asymmetries for the Λ_c^+ production the method of partial reconstruction of the Λ_c^+ is introduced, resulting in asymmetries for (Λ^0,π^+)-pairs in different kinematical intervals. These asymmetries are discussed in the context of various Monte Carlo estimates of the signal and the background. As the normalizations of

the Monte Carlo programs for quasireal hyperon production at modest $\sqrt{s}$ are largely untested and therefore questionable, the normalizations are based on the strength of the Λ_c^+ and $\Sigma^{\star+}$ peaks observed in the same data set. In this way a kinematic domain (at high P_T) where PGF dominates is identified, thus making it possible to associate the observed asymmetry with the gluon polarization. Unfortunately, the resulting $\Delta G/G$ is dependent on the (model) assumptions, similar to the model uncertainties hampering the high-p_T pair analysis [13] mentioned above. Despite these limitations the derived value for the raw asymmetry is used to extract a value for $\Delta G/G$. This estimate is compared to the value derived from the high-p_T pair analysis, and other data available on $\Delta G/G$. Finally, the most important results are summarized in the last section.

4.2 Data selection

Four years of data taking have been used for the analysis presented in this chapter. In 1997 a polarized hydrogen target ($\vec{\mathrm{H}}$) was used. In 1998, 1999 and 2000 data were taken on a polarized deuterium target. Apart from 1998 the DIS lepton was a positron. During data taking two major improvements in the experimental setup took place. In between the 1997 and 1998 runs a Ring Imaging Čerenkov Counter (RICH) replaced a Threshold Čerenkov detector, thereby improving the hadron identification capabilities. Furthermore, the target density was increased in the year 2000 by reducing the diameter of the target cell and operating the cell at a lower temperature. Together with improved HERA positron intensities, the overall luminosity was increased by about a factor three.

The data quality requirements on the beam burst level are given in table 4.1. The requirements were taken from [51, 54] and are generally used for measurements of double spin asymmetries at HERMES. The last requirement listed in the table, i.e. that at least one event per burst should have tracks of opposite sign implicitly removes bursts where the tracking detectors were not operational.

In order to obtain the relative statistical size of the datasets collected in each year the luminosity defined as

$$\mathcal{L} = \Phi_{Beam} N_{targ} \tag{4.3}$$

where Φ_{Beam} is the flux of beam particles and N_{targ} is the number of target atoms within the beam cross section needs to be computed. The luminosity can be determined from the detection of coincident e^-e^-, e^+e^- or $\gamma\gamma$-pairs resulting from the interaction of the beam lepton with atomic electrons of the target atoms. Three different processes can be distinguished depending on the beam lepton. For an electron beam Møller scattering of the beam electrons off the atomic electrons in the target results in e^-e^--pairs.

Table 4.1: *Data Quality Requirements.*

Criterion	Imposed requirements
Target type	Polarized proton or deuterium target
First Burst in fill	Reject
Burst Length	$0 \text{ s} \leq \Delta_{Burst} \leq 11 \text{ s}$
Luminosity trigger rate	$7.5 \text{ Hz} \leq \dot{L} \leq 1250 \text{ Hz}$
Dead time correction factor	$0.6 \leq \eta_{Dead} \leq 1.0$
Beam polarization	$0.3 \leq \lvert P_{Beam} \rvert \leq 0.8$
Target polarization	$0.8 \leq \lvert P_{Target} \rvert \leq 0.99$
Tracking performance	At least one event with two or more tracks with opposite sign

For a positron beam Bhabha scattering of the beam positrons off the atomic electrons in the target results in e^+e^--pairs, and pair annihilation of the beam positrons with the atomic electrons gives rise to the $\gamma\gamma$-pair final state. At HERMES a dedicated calorimeter (i.e. the luminosity monitor) is available, which is used to measure and identify these lepton pairs (see section 3.3.2).

Table 4.2: *Uncorrected and dead time corrected integrated luminosities in* pb^{-1} *for each of the data taking periods considered in this thesis.*

	1997	1998	1999	2000	total
$\mathcal{L}_{tot}$	36.86	33.53	37.26	163.27	270.92
$\mathcal{L}_{eff}$	35.97	32.06	35.31	154.55	257.89

The (effective) luminosities for the four different data-taking periods are listed in Table 4.2. The large increase in yield for the 2000 data is a result of the new target cell design and optimal HERA beam performance as was mentioned before. For comparison, the total luminosity corresponds roughly to 10.3 million DIS events. After subdividing the luminosities in bins with the four different relative orientations of the target and beam spins, a double spin asymmetry for the luminosity detector data has been evaluated. As no such asymmetry is expected, the evaluation of the luminosity asymmetry serves to search for sources of possible false asymmetries. The obtained double spin asymmetry, which is based on the effective luminosity, is well below one percent (with

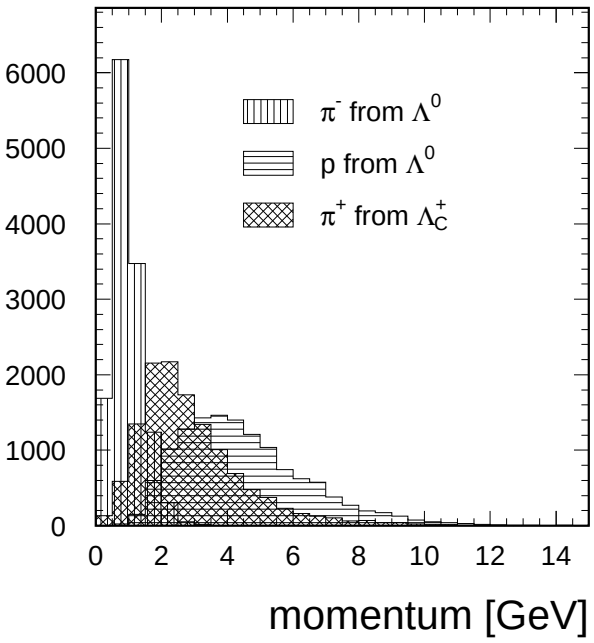

Figure 4.2: *Momenta of the Λ_c^+ decay products discussed in this chapter. These are the π^+ meson which is a direct decay product of the Λ_c^+, and the p and π^- which come from the Λ^0 which is itself a decay product of the Λ_c^+ baryon. The events were generated with the* AROMA *Monte Carlo and tracked through a model of* HERMES*. Only particles that were detected are taken into account such that the momentum distributions represent those of the data.*

a statistical uncertainty of less than 0.02% and a systematic uncertainty of about one to two percent from the relative luminosity measurement [41]) in each year apart from 1998. In 1998 a double spin asymmetry of $-2.969 \pm 0.013 \pm 1.400\%$ was found. No correction was applied for the non-zero asymmetry in the 1998 data set since only a small double spin asymmetry of -0.23% is found in the combined dataset of 1997, 1998, 1999 and 2000.

For only a small fraction of the events the DIS lepton was observed. Most of the undetected DIS leptons pass the HERMES spectrometer outside the acceptance at small polar angles ($\theta < 40$ mrad). Since no specific trigger requirement has been applied, almost all events are due to a photoproduction trigger which requires at least one track in both the lower and upper half of the detector.

For the application of the PID requirements the data sets are split in the period in which the threshold Čerenkov counter was used (1997), and the period in which the RICH was used (after 1997). The Čerenkov threshold momentum values for π, K and p detection are roughly 3.9 GeV, 13.9 GeV and 26.4 GeV. With the inclusion of the RICH the PID scheme in the data analysis has been simplified. To each particle a probability is attributed that it is of a specific type, the most probable particle type, and a ratio of the most likely probability with respect to the second best probability.

For the 1997 data, pion identification for momenta under 3.8 GeV requires the use of time-of-flight technique which was beyond the scope of this analysis. For this reason

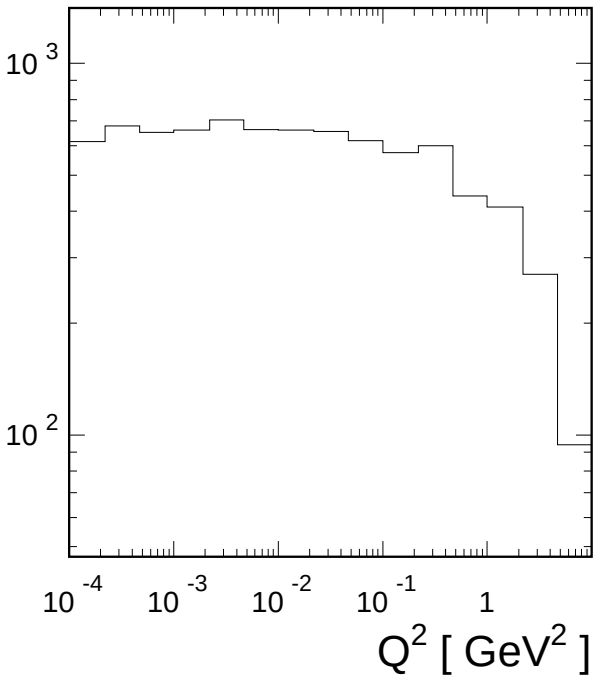

Figure 4.3: Q^2 *distribution of the events generated with the* AROMA *Monte Carlo and tracked through a model of the* HERMES *spectrometer. It is required that the particles are subsequently detected.*

these data are not used for the Ξ and $\Sigma^\star$ hyperon photoproduction described in section 4.3.1 as most of the direct Ξ or $\Sigma^\star$ decay pions fall below this threshold. The 1997 dataset is also excluded for the complete Λ_c^+ reconstruction discussed in section 4.3.2 since the K^+ contamination of the p sample is unknown in the absence of a RICH detector. On the other hand, for the partially reconstructed Λ_c^+ particles, which is the subject of section 4.5, the 1997 dataset is included as it is possible to correct for the K^+ contamination via the background subtraction. The RICH data has been used to check the validity of this approach.

In order to get a feeling for the momenta of the decay products of the Λ_c^+ baryon (i.e. the Λ^0 hyperon and the π^+ meson from the Λ_c^+ baryon) expected, the corresponding momentum distributions are shown in figure 4.2. The AROMA Monte Carlo was used to generate a sample of events which were subsequently tracked through a model of the HERMES spectrometer. It is observed that the momenta of the decay pions are almost all below 2 GeV, while the corresponding proton momenta can be as large as 10 GeV. The distribution of the direct π^+ mesons peaks at 2 GeV. In figure 4.3 the Q^2 values for the events that led to a detectable Λ^0 hyperon and π^+ meson, both coming from a Λ_c^+ baryon, are given. From the figure an average $\langle Q^2 \rangle = 0.31$ GeV^2 has been determined. The smallness of the average Q^2 is reflected in the absence of the DIS lepton which goes undetected.

4.3 Event reconstruction

The Λ_c^+ baryon (2284.9±0.6 MeV [55]) is the lightest baryon containing a charm quark. As a result it has many different decay channels with small branching ratios. The decay particles originating from the Λ_c^+ baryon which are most conveniently detected are the charged decay products coming directly from the Λ_c^+, and those coming from intermediate neutral decay products. The multiplicity of direct Λ_c^+ decay products ranges from two particles to six particles. If subsequent decays are also considered and only the 2γ decay branch is used for the π^0 meson, the multiplicity of the complete final state ranges from three to nine particles.

For the complete reconstruction of the Λ_c^+ baryon only those decay channels are of interest that result in three observable particles since the acceptance of the HERMES spectrometer drops roughly a factor of ten for every additional particle observed in the final state. Furthermore, the combinatorial background from quasireal photoproduction increases with multiplicity. For these reasons decay channels with only two decay particles are the best candidates when searching for a mass peak. Table 4.3 provides some information on Λ_c^+ decay channels involving only two particles.

Table 4.3: *Decay channels of the Λ_c^+ baryon with only two decay products. The branching ratios (in %) are given for each decay. In the last column the maximum momentum of the decay particles in the Λ_c^+ rest frame is listed. [55]*

Channel	Λ_c^+ Decay mode	total B.R. [%]	P_{CM}^{max} [MeV]
I	$\Lambda_c^+ \overset{0.9\pm0.3}{\longrightarrow} \Lambda^0\pi^+ \overset{63.9\pm0.5}{\longrightarrow} (\mathrm{p}\pi^-)\pi^+$	0.58 ± 0.18	863
II	$\Lambda_c^+ \overset{2.3\pm0.6}{\longrightarrow} \overline{\mathrm{K}}^0\mathrm{p} \overset{50}{\longrightarrow} \mathrm{K}_S^0\mathrm{p} \overset{68.6\pm0.3}{\longrightarrow} (\pi^+\pi^-)\mathrm{p}$	0.8 ± 0.2	872

Channel I is the most favorable channel to search for the Λ_c^+ baryon despite the higher total branching ratio for channel II. This is a consequence of the higher background for the $\overline{\mathrm{K}}^0\mathrm{p}$ channel as compared to the $\Lambda^0\pi^+$ channel. This is illustrated in figure 4.4 where the raw measured and reconstructed mass distributions for both decay channels are shown. At the expected location of the Λ_c^+ peak, the spectrum corresponding to the $\overline{\mathrm{K}}^0\mathrm{p}$ channel (top panel in figure 4.4) is a factor three higher than the spectrum corresponding to the $\Lambda^0\pi^+$ channel (bottom panel in figure 4.4). As the raw $\mathrm{M}(\pi^+\pi^-\mathrm{p})$ spectra do not provide any evidence for the observation of a Λ_c^+ peak, the spectra mostly represent the combinatorial background which is thus observed to be higher in

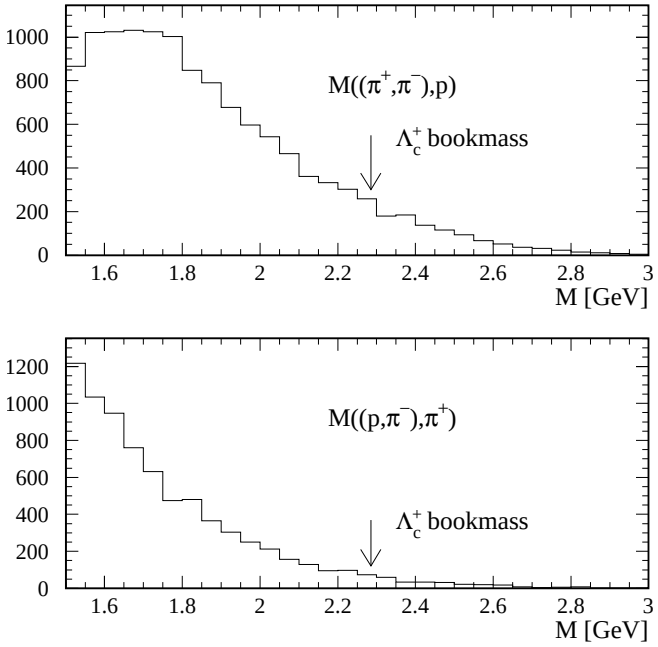

Figure 4.4: *Measured $(\pi^+\pi^-p)$-mass distribution obtained from a combination of particles which may also represent a Λ_c^+ decay; $\Lambda_c^+ \rightarrow \Lambda^0\pi^+$ or $\Lambda_c^+ \rightarrow \overline{K}^0 p$. Particles are identified using the* RICH *detector in* HERMES *and a three sigma cut around the Λ^0 (bottom) or K_S^0 mass peaks (top). The two spectra are based on the same data set.*

the $\overline{\mathrm{K}}^0$p case.

In order to investigate whether the data contain any Λ_c^+ events further requirements must be imposed on the data. These additional requirements will be developed using the Ξ and $\Sigma^\star(1385)$ hyperon spectra extracted from the same data set.

4.3.1 Ξ and $\Sigma^\star(1385)$ reconstruction

Only a small fraction of the Λ_c^+ baryons decays into a $(\Lambda^0\pi^+)$-pair. Particles decaying into a Λ hyperon and a π meson with appreciably higher branching ratios are the Ξ hyperon and the charged excited $\Sigma^\star(1385)$ hyperon. In the rest of this section the $\Sigma^\star(1385)$ will be denoted as $\Sigma^\star$. For future reference the relevant information on the Λ, Ξ and $\Sigma^\star$ hyperons is given in table 4.4. The higher branching ratios favor the detection of these particles in HERMES. Moreover, their lower mass results in lower transverse momenta of the decay products, thereby also favoring detection in HERMES.

The kinematics for particles decaying into a $(\Lambda^0\pi)$-pair is introduced using the Ξ^- hyperon decay. The same reasoning also applies to the decay of the Ξ^+, $\Sigma^{\star-}$, $\Sigma^{\star+}$ and Λ_c^+ baryons.

In figure 4.5 a schematic drawing of the decay $\Xi^- \rightarrow \Lambda^0\pi^-$ with $\Lambda^0 \rightarrow \mathrm{p}\pi^-$ is shown. The reconstruction of the Ξ^- mass spectrum is based on the following argument. The

Table 4.4: *Information on the Ξ and $\Sigma^\star$ hyperons that decay predominantly into a Λ^0 hyperon and a π^- or π^+ meson. For the Λ^0 hyperon, which is also included in the table, the decay channel $\Lambda \to p\pi$ is understood. The symbols are explained in the caption of table 4.3. The data are taken from [55].*

particle	mass [MeV]	Full width Γ [MeV]	B.R. %	P_{CM}^{max} [MeV]	$c\tau$ [cm]
Λ^0	1115.683 ± 0.006		63.9 ± 0.5	101	7.89
$\Xi^\pm$	1321.31 ± 0.13		99.887 ± 0.035	139	4.91
$\Sigma^{\star+}$	1382.8 ± 0.4	35.8 ± 0.8	88 ± 2	208	
$\Sigma^{\star-}$	1387.2 ± 0.5	39.4 ± 2.1	88 ± 2	208	

tracks of the p and π^- determine the decay or secondary vertex of the Λ^0. This point is fixed at the middle of the line connecting the π^- and p tracks where they are closest. From the four momenta of the p and π^- the Λ^0 four momentum is evaluated, thereby defining the Λ^0 track. Crossing this Λ^0 track with the π^- track from the Ξ^- hyperon enables the determination of the production or primary Λ^0 vertex, which at the same time is the Ξ^- decay vertex. Similar to the Λ^0 case the Ξ^- track is crossed with the beam-axis to give the primary Ξ^- vertex. In doing so it is assumed that the beam-axis coincides with the HERMES z-axis.

The following variables are used in the reconstruction of the various particles. Each of them can be used as a means to impose additional requirements on the selected events.

D(p, π^-): the distance of closest approach between the p and π^- tracks that both originate from the Λ^0 hyperon.

D(Λ^0, π^-): the distance of closest approach between the Λ^0 and π^- tracks that both originate from the Ξ^- hyperon.

D(Ξ^-, beam): the distance of closest approach between the Ξ^- and the beam axis. See insert in figure 4.5.

ΔZ_{Λ^0}: the vertex separation between the Λ^0 production and decay vertices in the z-direction, i.e. the projected distance between the Λ^0 vertices on the z-axis.

ΔZ_{Ξ^-}: the vertex separation between the Ξ^- production and decay vertices in the z-direction.

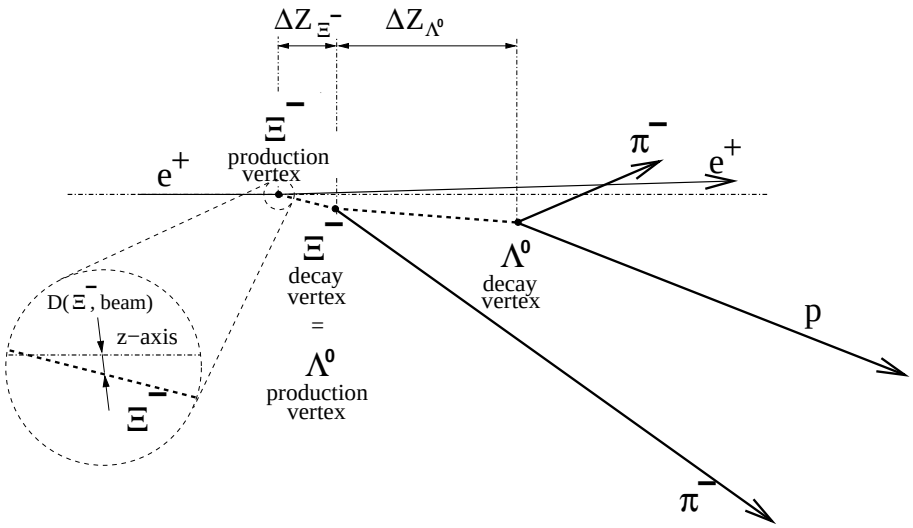

Figure 4.5: *Schematic drawing of the tracks appearing in the reconstruction of a* Ξ^- *hyperon. The symbols are explained in the text.*

CL: the collinearity of the Λ^0 hyperon is the cosine of the angle between two different determinations of the Λ^0 propagation direction; one direction is determined from the tracks of the Λ^0 decay particles, and the other follows from the position difference of the production and decay vertices.

P_{T,Λ^0}: the transverse momentum of the Λ^0 with respect to the Ξ^- direction.

As an example of how some of these variables are obtained from the data, we consider the evaluation of the vertex position of a particle. The middle of the line segment that connects the two tracks at the distance of closest approach is often used as vertex position. Instead, this distance is approximated by the minimal length of a line segment perpendicular to the Z-axis that connects the two tracks. Due to the small polar angles of the HERMES tracks this approach can be used. As a starting point it should be realized that for each track we obtain from the raw data the X^i, Y^i coordinates and the slopes δX^i and δY^i at Z_0^i. The value of Z_0^i is fixed in the middle of the magnet, i.e. 275 cm downstream the target. With

$$\vec{t^i} = \begin{pmatrix} X^i \\ Y^i \\ Z^i \end{pmatrix}, \vec{t_0^i} = \begin{pmatrix} X_0^i \\ Y_0^i \\ Z_0 \end{pmatrix}, \vec{\delta t^i} = \begin{pmatrix} \delta X^i \\ \delta Y^i \\ 1 \end{pmatrix}, \text{and } \Delta Z = Z^i - Z_0 \,, \tag{4.4}$$

where $(X_0^i, Y_0^i, Z_0)^T$ is a point on the track at Z_0 and δX^i and δY^i are the X and Y slopes, a track $\vec{t^i}$ at z-position Z^i is defined as

$$\vec{t^i} = \vec{t_0^i} + \vec{\delta t^i}\ \Delta Z \,. \tag{4.5}$$

The approximate Z-coordinate of the vertex from which two tracks originate is thus determined from the following expression

$$\Delta Z = \frac{(\vec{t}_0^{\,1} - \vec{t}_0^{\,2}) \cdot (\delta\vec{t}^{\,1} - \delta\vec{t}^{\,2})}{(\delta\vec{t}^{\,1} - \delta\vec{t}^{\,2}) \cdot (\delta\vec{t}^{\,1} - \delta\vec{t}^{\,2})} \,. \tag{4.6}$$

Substitution of Z_{vert} (from ΔZ) into formula 4.5 for $i = 1, 2$ gives the points on the tracks corresponding to the approximate distance of closest approach. From these two points the approximate distance between the tracks (defined as $\mathrm{D}(p_1, p_2)$ above) and the remaining X_{vert} and Y_{vert} coordinates follow.

A sample of Ξ^-events has been generated with the PYTHIA event generator in order to study the expected spectra for various kinematic variables. These events are tracked through a GEANT model of the HERMES detector to include all the effects introduced in the data due to decay, multiple scattering, losses and track reconstruction. The results are shown in figure 4.6 for some of the variables introduced before. The important characteristic of the mass distributions are the mean value and the width, which are listed in the figures where relevant.

The width of the mass difference, $\Delta\mathrm{M}$ = M(Ξ^-) - M(Λ^0), is smaller than that of the M(Ξ^-) spectrum expressing the correlation between the Ξ^- and Λ^0 spectra when they are reconstructed. For this reason the mass difference will be used in the rest of this chapter. For ease of interpretation the Λ^0 mass taken from [55] has been added to ΔM in each case (i.e. ΔM+1.11568 GeV). The distance distributions $\mathrm{D}(\Lambda^0, \pi^-)$, $\mathrm{D}(\mathrm{p}, \pi^-)$ and $\mathrm{D}(\Xi^-, \mathrm{beam})$ have similar shapes but the average widths differ. This is primarily due to the opening angle of the tracks involved. The collinearity distribution is seen to be sharply peaked at 1, thus providing a good means to remove background. Unfortunately, in the data a strict requirement on the collinearity appears to reduce the similarity between the background and an estimate of this background. Therefore no strict requirement was made on the collinearity. The separation between the secondary and primary Ξ^- vertices, i.e. ΔZ_{Ξ^-}, is peaked at zero with a decay distribution towards positive values of ΔZ_{Ξ^-}. It is noted that ΔZ_{Ξ^-} can be negative due to the finite resolution of the reconstructed vertices (As the decay length of the $\Sigma^\star$ hyperons is negligible the value for $\Delta Z_{\Sigma^\star}$ is taken equal to ΔZ_{Ξ^-}.).

The kinematic requirements imposed in the analysis of the Ξ and $\Sigma^\star$ hyperons are given in table 4.5. The values of these requirements are relatively generous (see the vertical lines representing the requirements in figure 4.6) to avoid a strong dependence on their value and to increase statistics. It is noted that very stringent requirements improve the S/B ratio, but at the same time the difference between the background under the Ξ and $\Sigma^\star$ peaks increases, making the background estimate more difficult (the

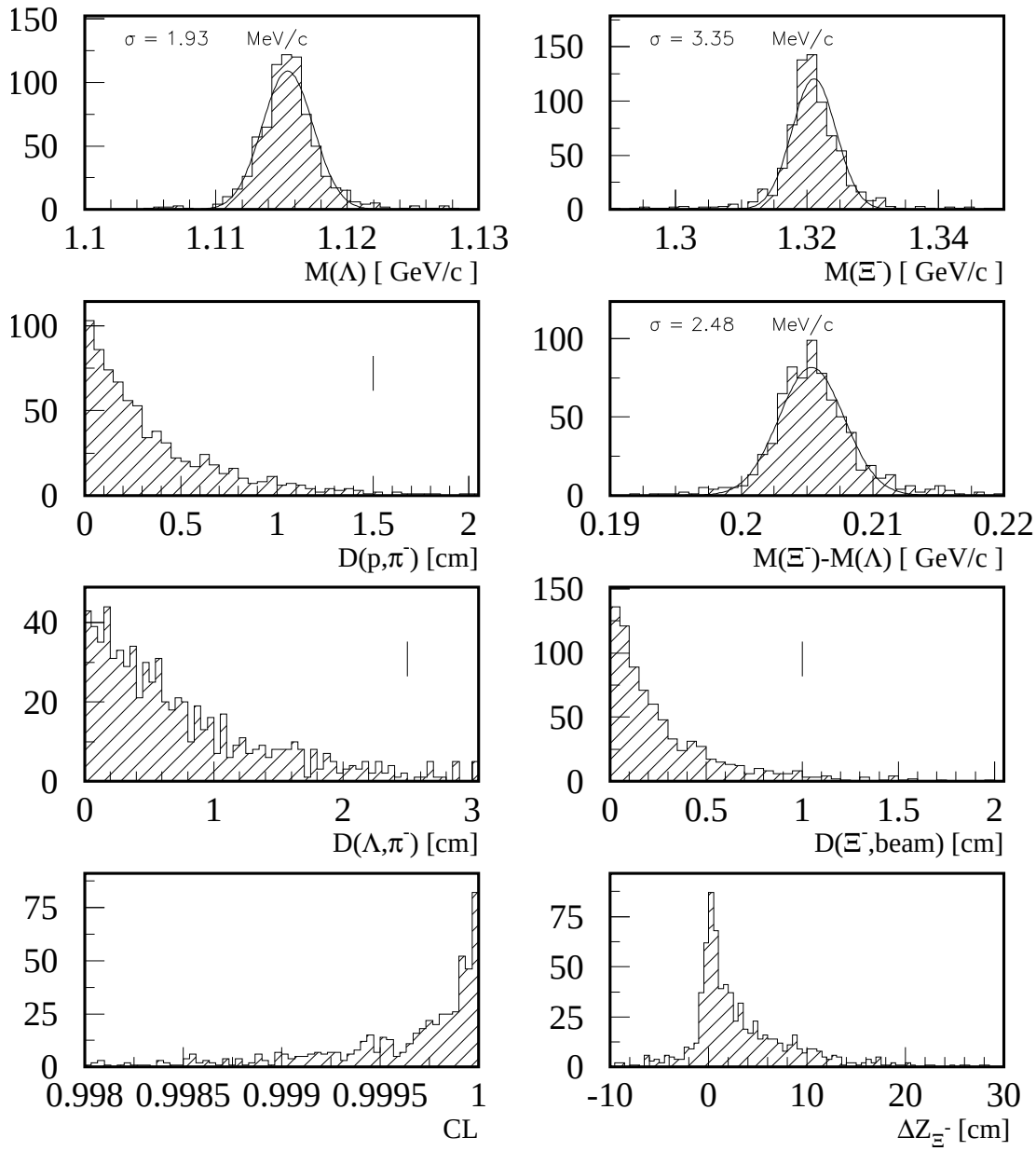

Figure 4.6: *Monte Carlo results for reconstructed* Λ^0 *and* Ξ^- *hyperons that decayed into a* Λ^0 *hyperon and a* π^- *meson. The* Ξ^- *hyperons were generated using* PYTHIA *and the decay products were tracked through a* GEANT *model of the* HERMES *detector.*

Table 4.5: *Kinematical requirements used for the selection of* Ξ *and* $\Sigma^\star$ *hyperons in the 1998, 1999 and 2000 data.*

Requirement	value
$D(\mathrm{p}, \pi^-)$	< 1.5 cm
$D(\Lambda^0, \pi^-)$	< 2.5 cm
$D(\Xi^-, \mathrm{beam})$, $D(\Sigma^\star, \mathrm{beam})$	< 1.0 cm
ΔZ_{Λ^0}	> 0.0 cm
ΔZ_{Ξ^-}, $\Delta Z_{\Sigma^\star}$	$>$ -15 cm
CL	> 0.995

background is estimated from reconstructed ((pπ) π) combinations with the (pπ) mass outside the Λ mass region). Since the kinematic requirements should not influence the yield ratio between the Ξ and the $\Sigma^\star$ hyperons it was decided to use relatively wide cuts on the spectra, and no effort was undertaken to further improve them.

As a first step in the analysis the invariant mass spectrum for the Λ^0 and $\overline{\Lambda}^0$ hyperons were extracted from the data with and without an additional $\pi^\pm$ track in the event. In figure 4.7 un-tagged Λ^0 and $\overline{\Lambda}^0$ mass spectra as well as the π-tagged mass spectra are shown. As no extra particle is used for the un-tagged reconstruction of a Λ hyperon a vertex with the beam is made. In the selection of Λ candidates the (p,π)-pair with its mass closest to the PDG value is taken, if more (p,π)-combinations can be made in one event.

For the determination of the total number of (tagged) Λ hyperons in the six different spectra the background is represented by a linear shape. The signals in the Λ^0 and the un-tagged $\overline{\Lambda}^0$ spectra are represented by a double Gaussian shape, while a single Gaussian shape is used for the π-tagged $\overline{\Lambda}^0$ mass spectra. The fits are performed in between 1.095 GeV and 1.15 GeV. After background subtraction the counts are obtained from the three σ region around the Λ mass where for the double Gaussian shape the largest σ value is taken. From the figure it is clear that the S/B ratio for the $\overline{\Lambda}^0$ hyperon is considerably smaller than the S/B ratio for the Λ^0 hyperon. This is at least partly due to a contamination of K^- mesons in the $\overline{\mathrm{p}}$ sample.

In table 4.6 the number of counts for the six different spectra of figure 4.7 are given. These results correspond to all polarized data obtained by HERMES in the years 1998, 1999 and 2000, and thus correspond to the equivalent of 8.2 million DIS events which

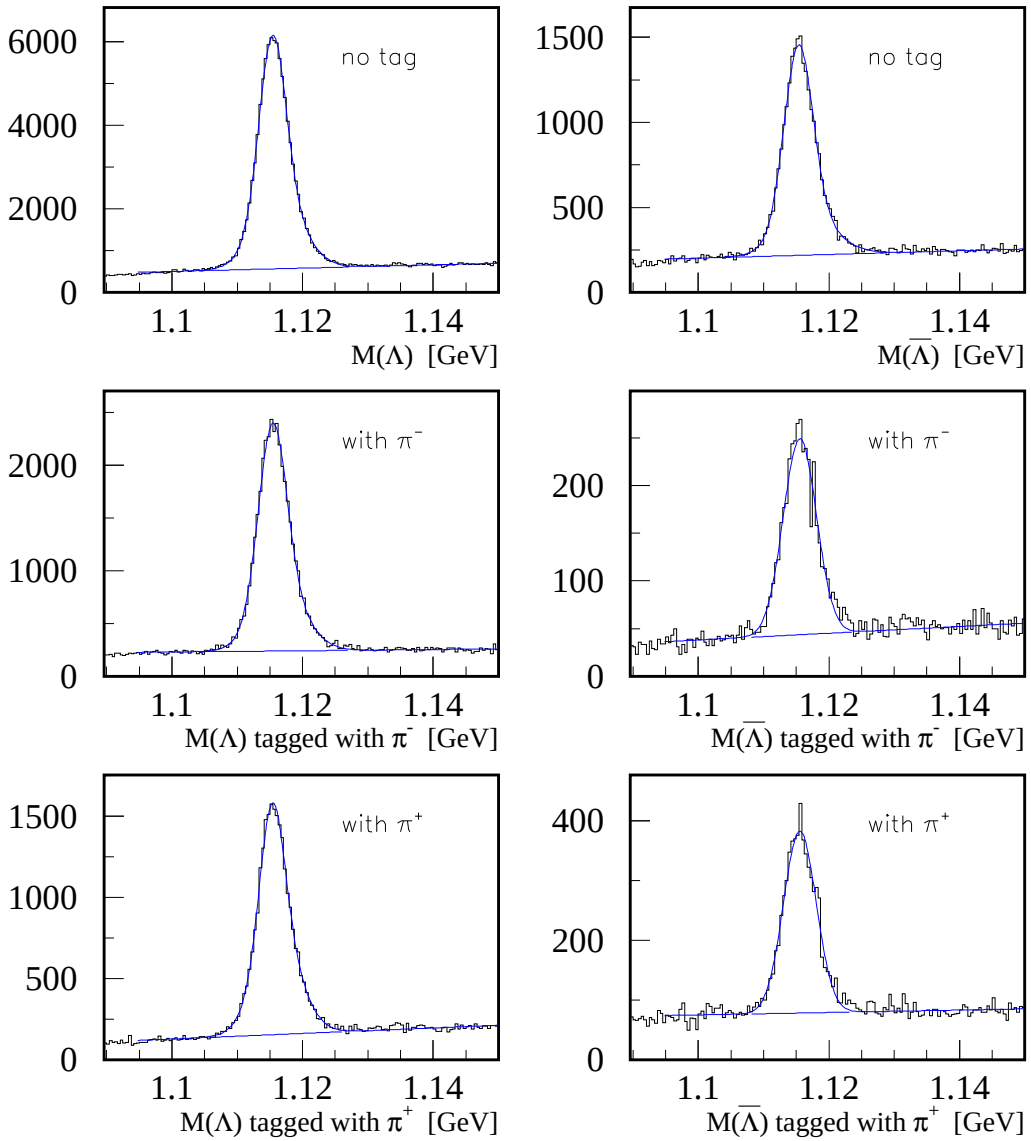

Figure 4.7: Λ^0 *(left) and* $\overline{\Lambda}^0$ *(right) mass spectra for three different situations. The upper panel shows the* Λ *spectra without requiring additional particles in the spectrometer. In the middle panel the* Λ *is tagged with a* π^- *meson satisfying the requirements of table 4.5, and in the lower panel the tagging particle was a* π^+ *meson. The fits shown are a sum of two Gaussians except for the tagged* $\overline{\Lambda}^0$*, where a single Gaussian is used.*

Table 4.6: *Number of un-tagged and π-tagged Λ^0 and $\overline{\Lambda}^0$ counts extracted from the polarized data collected in the years 1998, 1999 and 2000.*

tag	Λ^0 counts ($\times 10^3$)	$\overline{\Lambda}^0$ counts ($\times 10^3$)
none	84.0 ± 0.4	19.0 ± 0.2
π^-	33.2 ± 0.2	3.24 ± 0.08
π^+	21.35 ± 0.19	4.68 ± 0.10

Table 4.7: *Yields expressed in μb for the π-tagged Λ hyperons obtained from the data and the* PYTHIA *Monte Carlo. The effect of using a Deuterium target was simulated by combining* PYTHIA *results for both a proton and neutron target. In the last column the average of the* PYTHIA *yields on the proton and neutron were used to get the ratio between the* PYTHIA *yield and the data yield corrected for the photoproduction trigger efficiency.*

hadron pair	data	PYTHIA Monte Carlo		$\frac{N_{PYTHIA}}{N_{DATA}}$	$\frac{N_{PYTHIA}}{N_{DATA}\rfloor_{corr}}$
		neutron	proton		
	[μb]				
Λ^0, π^-	$1.50 \cdot 10^{-4}$	$6.92 \cdot 10^{-4}$	$7.05 \cdot 10^{-4}$	4.66	3.40
Λ^0, π^+	$9.6 \cdot 10^{-5}$	$5.58 \cdot 10^{-4}$	$5.59 \cdot 10^{-4}$	5.82	4.25
$\overline{\Lambda}^0, \pi^-$	$1.46 \cdot 10^{-5}$	$5.08 \cdot 10^{-5}$	$5.12 \cdot 10^{-5}$	3.49	2.55
$\overline{\Lambda}^0, \pi^+$	$2.11 \cdot 10^{-5}$	$4.70 \cdot 10^{-5}$	$4.66 \cdot 10^{-5}$	2.22	1.62

were recorded in that period. The given errors are statistical only. The table shows that Λ^0 hyperons are more abundant than $\overline{\Lambda}^0$ hyperons as expected. The requirement of a π-tag reduces the yield by a factor 3-4 for Λ^0 hyperons, while this factor increases to 4-6 for $\overline{\Lambda}^0$ hyperons.

The number of counts in table 4.6 are meant to put the Ξ and $\Sigma^\star$ results in perspective. They can, however, also be used to investigate the quality of the normalization of the PYTHIA Monte Carlo, which is important for future reference. For a comparison with the PYTHIA Monte Carlo the number of tagged Λ hyperons found in the data is expressed in μb using the total effective luminosity of 221.92 pb^{-1} collected in the years 1998, 1999 and 2000 from table 4.2. The yields, obtained from the data

and from the PYTHIA Monte Carlo[2] (using both a proton and a neutron target) for the Λ^0 and $\overline{\Lambda}^0$ tagged with a π^- or with a π^+ meson are given in table 4.7. No large differences in the yield for scattering on a proton or neutron target are observed in the PYTHIA results. Therefore, the average of the π-tagged Λ yield from PYTHIA on the proton and the neutron was used when evaluating the ratio between the data and the Monte Carlo. From these ratios it is concluded that the PYTHIA Monte Carlo largely overestimates the π-tagged Λ yield in the HERMES kinematic domain. Part of the overestimation can be accounted for by the trigger efficiency which was less than one. The mean value of the photoproduction trigger efficiency was determined in [56] to be about $\epsilon_{trig.}^{photo} = 73 \pm 0.4\%$. Using this value of the trigger efficiency, the last column of table 4.7 was evaluated. It is concluded that PYTHIA overestimates the Λ^0-channels by a factor 3 to 4 and the $\overline{\Lambda}^0$-channels by a factor 2 to 3.

Now the reconstruction of the Ξ and $\Sigma^\star$ hyperons is taken up again. In figure 4.8 the mass spectra for combinations of a (anti) Λ with a π^- or π^+ are shown as a function of M=ΔM+M$_\Lambda$. If more than one Λ^0 candidate was found in one event, the candidate having its mass closest to the PDG value is taken. A three σ region around the Λ^0 mass was used to arrive at the spectra shown in figure 4.8. Given the width of the Λ peak, $\sigma = 2.5$ MeV, the mass window on M(pπ^-) (corresponding to the mentioned 3σ interval) ranges from 1.108 GeV to 1.123 GeV. Two intervals outside the Λ^0 mass region, one from 1.08 GeV to 1.103 GeV and one from 1.13 GeV to 1.17 GeV are used to construct a background $\Lambda\pi$ spectrum. The background has been smoothed, and is represented by a darker color in figure 4.8. The $\bar{\text{p}}$ sample used for construction of the background of the $\overline{\Lambda}^0$ spectrum has a large K$^-$ contamination due to the less than optimal $\bar{\text{p}}$-K$^-$ separation provided by the RICH. For this reason the $((\text{p}, \pi^-), \pi)$ background is used to represent the $((\bar{\text{p}}, \pi^+), \pi)$ background as well. The background spectra are normalized in the mass interval from 1.45 GeV to 2.0 GeV, except for the M($\overline{\Lambda}^0$,π^-) spectrum which is normalized in the interval from 1.45 GeV to 1.55 GeV in an effort to account for the shape difference between the generated and observed background spectra. For convenience the matching regions mentioned above are shown in figure 4.8 as dark bands.

The background estimate based on the Λ^0 mass side bands gives a good representation of the (Λ^0,π)-pair mass spectrum (figure 4.8, upper panels) which thus can be used for a background subtraction. In the upper right panel of figure 4.8 a slight underestimate of the background left from the signal peak is observed. This might be caused by Λ^0 hyperons coming from one of the intermediate $\Sigma^{\star-}$ decay products, i.e. $\Sigma^{\star-} \rightarrow \Sigma^0\pi^+$ (B.R. 12%), which will be present in this region as well. While the

[2]For reference the program settings are given in the appendix.

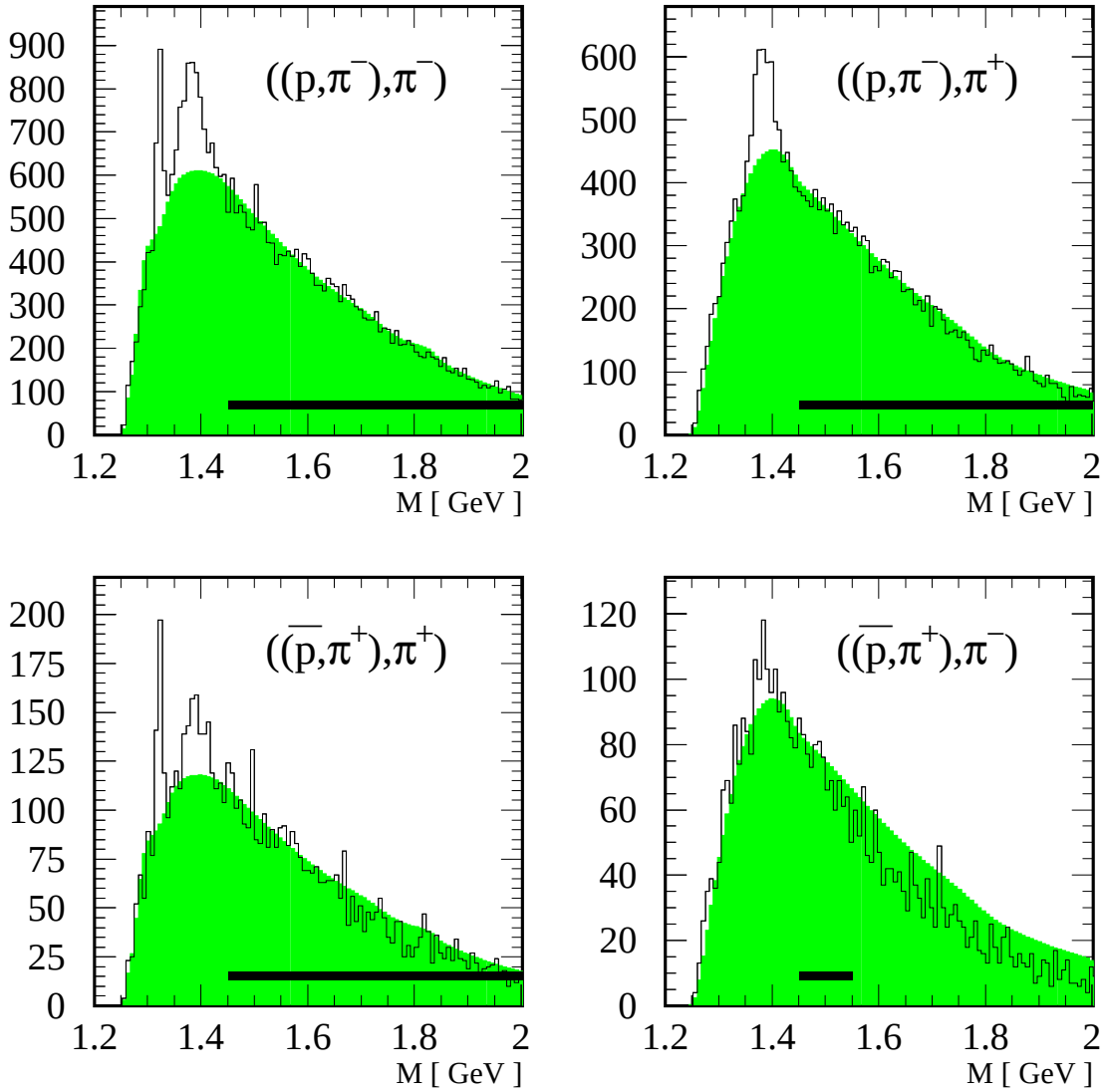

Figure 4.8: *Mass difference spectra for various 3-particle combinations of an (anti)-proton and two pions. The Λ^0 mass has been added to the mass difference. The filled histogram is obtained from the Λ^0 side-bands after normalization and smoothing. The dark bands give the interval used for the normalization of the background.*

background of the M($\overline{\Lambda}^0$,π^+) spectrum is fairly well reproduced using the method described above, for the M($\overline{\Lambda}^0$,π^-) mass spectrum the background shape derived from the (Λ^0,π^+)-side band shows a clear deviation from the data. Because of this the yield estimate for the $\overline{\Sigma}^{\star-}$ hyperon will cary a large systematic uncertainty.

The Ξ and $\Sigma^\star$ hyperon spectra after background subtraction are shown in figure 4.9 for each (Λ, π) combination. In order to extract the number of observed Ξ or $\Sigma^\star$ hyperons from the background subtracted spectra, the data were fitted using a Breit-Wigner shape with fixed full width (from the PDG [55]) for the $\Sigma^\star$ and a Gaussian shape with a free width for the Ξ. To account for residual background contributions a constant was added to the fit in the M($\overline{\Lambda}^0$,π^-) spectrum and a first order polynomial has been added in the other fits. In order to limit the sensitivity of the fit to possible fluctuations in the background at high mass difference the fit has been limited to the region from 1.275 GeV to 2.0 GeV, where again an exception for the ($\overline{\Lambda}^0$,π^-) spectrum is needed. In this case, the fit is limited to the mass difference region from 1.275 GeV to 1.5 GeV.

It has been verified that a fit with a free Breit-Wigner width results in values which are in agreement with the PDG values for the $\Sigma^\star$ hyperons. For the two lower panels of figure 4.9 an unconstrained fit yields a width which is larger than expected. This is most probably due to a combination of poor statistics and a background shape which resembles the signal shape in the region of interest. For this reason it was chosen to fix the width to those of the PDG [55].

In the upper left plot of figure 4.9 the background above 1.5 GeV shows a weak oscillation, which may be due to the presence of another resonance in the data. A candidate for such an additional resonance would be the $\Sigma^{\star-}(1670)$ with a full width of about 60 MeV. This has not been further pursued in view of the weakness of the signal.

The yields, masses and widths (where relevant) obtained from the fits together with Monte Carlo estimates of the yield are given in table 4.8. In order to estimate the systematic error on the yields the normalizations of the background were also performed using the M(Λ, π) spectrum in between 1.45 and 1.65 GeV, 1.65 and 1.85 GeV and 1.85 and 2.05 GeV, respectively. The uncertainty on the mean values and widths of the hyperon peaks were taken from the fit.

The Monte Carlo results listed in table 4.8 were generated from neutron and proton samples in equal proportions, as the data were collected on a deuterium target. As no

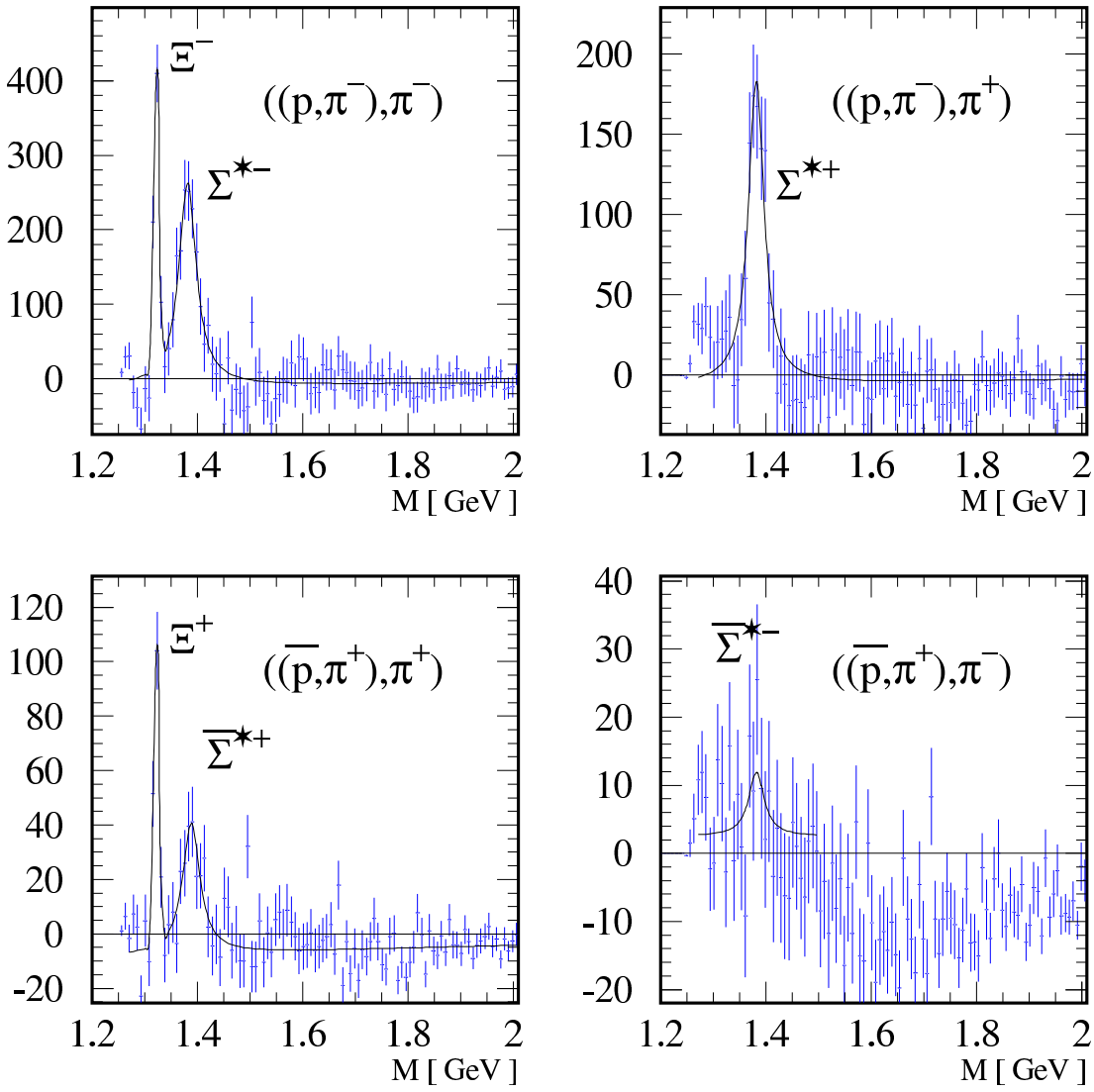

Figure 4.9: *Fits of the $p\pi\pi$ spectra after background subtraction. The results of the fits corresponding to the particles as named in the figures are given in table 4.8.*

Table 4.8: *Values for the count rates, masses and widths as obtained from the fits applied to the ($p\pi\pi$) mass spectra from the polarized 1998, 1999 and 2000 data. The fit procedure is explained in the text. For the evaluation of the yields a photoproduction efficiency of* $73\pm0.4\%$ *[56] is assumed. The last column contains the counts obtained from tracked* PYTHIA *events reconstructed under the same conditions, normalized by multiplying the* PYTHIA *counts with the measured luminosity divided by the luminosity as given by* PYTHIA.

Particle	yield	mass [GeV]	σ [MeV]	MC counts	decay particles
Ξ^-	$916 \pm 84 \pm 16$	1321.5 ± 0.3	3.1 ± 0.3	846	$p\pi^-\pi^-$
$\Sigma^{\star-}$	$3094 \pm 182 \pm 191$	1381.1 ± 1.5		4944	$p\pi^-\pi^-$
$\Sigma^{\star+}$	$1944 \pm 129 \pm 307$	1377.6 ± 1.7		14208	$p\pi^-\pi^+$
Ξ^+	$258 \pm 29 \pm 37$	1320.6 ± 0.6	3.2 ± 0.5	225	$\overline{p}\pi^+\pi^+$
$\overline{\Sigma}^{\star+}$	$547 \pm 47 \pm 247$	1383 ± 2		703	$\overline{p}\pi^+\pi^+$
$\overline{\Sigma}^{\star-}$	$96 \pm 41 \pm 299$	1374 ± 2		655	$\overline{p}\pi^+\pi^-$

clear difference between the two calculations was observed the average taken over both target nuclei is used to arrive at the value for the MC counts as given in the table.

The position of the Ξ^- and Ξ^+ peaks are in excellent agreement with the known mass of these hyperons (see table 4.4), thus confirming the validity of our energy calibration and analysis procedure. The $\Sigma^\star$ masses are all below the PDG values suggesting a remaining background decreasing with reconstructed mass. Yield comparisons can be done as the phase space of the particles are very similar, as well as the branching ratios of the Ξ and $\Sigma^\star$ hyperons (see table 4.4). It is concluded that the yield of the strangeness-2 Ξ^- hyperon is a factor 2 to 3 below that of the strangeness-1 $\Sigma^{\star\pm}$ hyperons. The yield of the anti-hyperons is a factor 4 to 30 below that of the normal hyperons.

The yields of the Ξ^- hyperon and its antiparticle Ξ^+ observed in the data is in good agreement with the Monte Carlo yields. At most ten percent yield loss in the data can be assigned to protons not used in the analysis because they were identified as kaons. On the other hand the Monte Carlo generators and spectrometer reconstruction also carry uncertainties of at least 10%. Given these uncertainties, the PYTHIA Monte Carlo gives a surprisingly good estimate for the Ξ hyperon yield.

For the $\Sigma^\star$ hyperons PYTHIA overestimates the data by a factor 1.2 to 7. The largest difference is observed for the $\Sigma^{\star+}$ hyperon and its anti-particle $\overline{\Sigma}^{\star-}$. Compared to the $\Sigma^{\star-}$ and $\overline{\Sigma}^{\star+}$ hyperons the $\Sigma^{\star+}$ yield in PYTHIA is certainly grossly overestimated, while the conclusion on the $\overline{\Sigma}^{\star-}$ is less definite in view of the large uncertainties involved. Since the $\Sigma^{\star-}$ hyperon decay channel is equal to the the Λ_c^+ decay channel this large mismatch between PYTHIA and the data has a large influence on the Monte Carlo estimate of the background for partially reconstructed Λ_c^+ baryons (discussed in section 4.5).

4.3.2 Λ_c^+ Reconstruction

As explained in the beginning of this section, the study of the Ξ and $\Sigma^\star$ hyperons was triggered by the similarity of their decay products to the most favorable Λ_c^+ decay channel. It was shown that the requirements imposed while reconstructing the Ξ and $\Sigma^\star$ hyperon led to clean signals for almost all investigated peaks. There was no need to optimize the chosen requirements as the background could be estimated from the side bands in the Λ hyperon mass spectrum and clear signal peaks were obtained. For the reconstruction of the Λ_c^+ baryon one might argue that an optimization of the requirements with respect to the signal over background ratio based on the Ξ and $\Sigma^\star$ hyperon should be used. There is, however, no guarantee that this leads to the best conditions for Λ_c^+ reconstruction as its invariant mass (2.2849 GeV) is considerably higher. Therefore, the optimization of the kinematic requirements for the Λ_c^+ reconstruction has been developed independently.

Ideally, one would like to generate Monte Carlo events for the expected Λ_c^+ signal and for the background using the same Monte Carlo program. However, while the PYTHIA program can be used for the background generation it was not used for the Λ_c^+ signal even though it has the option to generate PGF events. The reason for this is the inability of the PYTHIA program to generate exclusively events coming from PGF. Hence, a huge amount of statistics is needed in order to carry out the simulations. Therefore, the Λ_c^+ signal has been generated with the AROMA Monte Carlo. This has the additional advantage of easier comparisons with other studies as the AROMA Monte Carlo program is almost always used for charmed particle production via the PGF process.

After generating the events with the Monte Carlo programs mentioned above the final state particles are tracked through a model of the HERMES spectrometer. Care should be taken when comparing the results of both programs on the cross section or yield level. This has been illustrated above when comparing the number of counts for

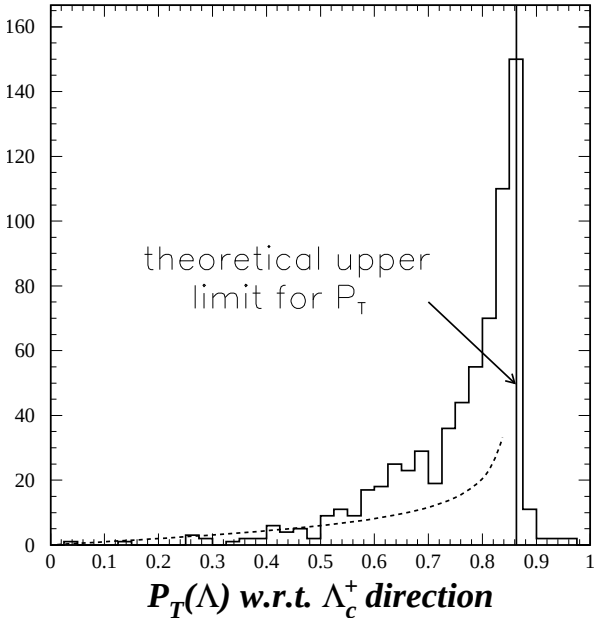

Figure 4.10: *Transverse momentum P_{T,Λ^0} of the Λ^0 hyperon in the direction of the Λ_c^+ baryon based on a* AROMA *Monte Carlo simulation. Only the decay channel $\Lambda_c^+ \rightarrow \Lambda^0\pi^+$ is considered. The dashed curve in the figure is the theoretical distribution for P_{T,Λ^0} assuming an isotropical distribution of the Λ^0 hyperon in the Λ_c^+ rest frame. It is normalized to the total number of events in the figure.*

the $\Sigma^\star$ hyperons expected from PYTHIA with those obtained from the data. Since the relative normalization of the AROMA Monte Carlo with respect to the PYTHIA Monte Carlo also carries uncertainties[3], the optimization of the S/B ratio of the Λ_c^+ peak based on these programs can only be performed in a relative fashion comparing one set of cuts to another.

Nevertheless, a sample of Λ_c^+ particles generated with the AROMA Monte Carlo can be used to study some aspects of the imposed requirements using the basic kinematic distributions of such events. For instance, if the requirement on the collinearity for the reconstruction of the $((p\pi^-)\pi^+)$ mass spectrum is set to 0.99998, the AROMA Monte Carlo events can be used to show that this leads to 33% loss in signal compared to the minimal value for the collinearity of 0.995 used for the reconstruction of the Ξ and $\Sigma^\star$ hyperons.

The transverse momentum of the Λ^0 with respect to the (Λ^0,π^+)-pair direction, P_{T,Λ^0}, has not been used in the Ξ and $\Sigma^\star$ reconstruction as it would affect the number of reconstructed Ξ and $\Sigma^\star$ particles differently. In figure 4.10 the P_{T,Λ^0} distribution for Λ_c^+ production obtained from the AROMA Monte Carlo is shown. The distribution is sharply peaked towards the theoretical maximum value of 863 MeV given in table 4.3. The dashed curve in the figure shows the theoretical P_{T,Λ^0}-distribution not corrected

[3]It has to be realized that AROMA and PYTHIA have been largely developed having higher-energy processes in mind. Also their use for hyperon production processes at modest energy was never pursued before.

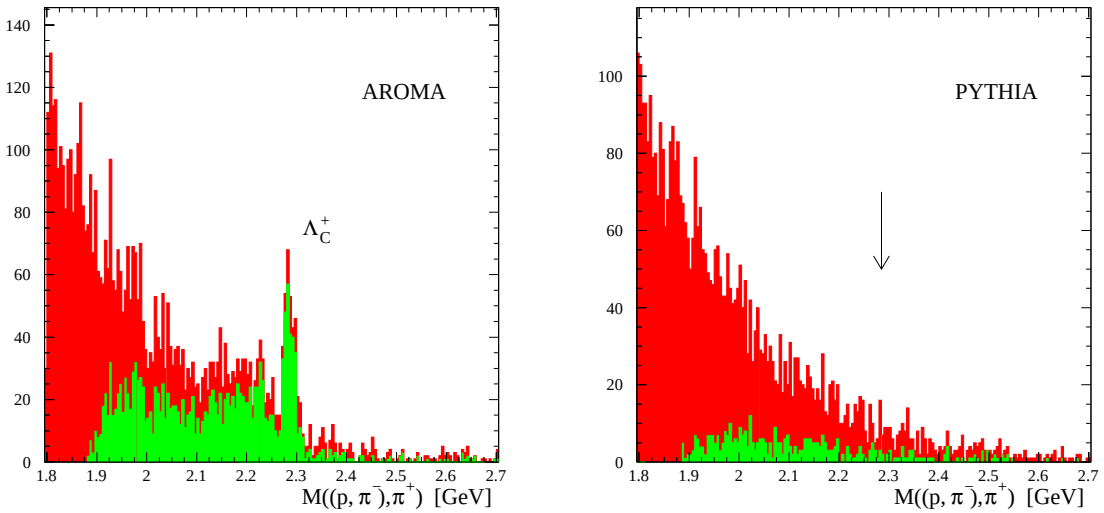

Figure 4.11: *(Λ^0,π^+)-pair mass distributions generated by two different Monte Carlo simulations. In the left panel the events are generated with* AROMA *yielding a clearly visible Λ_c^+ peak . After imposing the requirement 0.6 GeV $< P_{T,\Lambda^0} <$ 0.88 GeV (light histogram) the minimum reconstructable mass shifts up showing the correlation of this requirement with the reconstructed mass range. In the right panel the background simulated with* PYTHIA *is shown. No peak around the Λ_c^+ mass of* 2.285 *GeV is visible, even after imposing the P_{T,Λ^0} requirement.*

for acceptance effects. As the distribution of transverse momenta of single particles produced in deep-inelastic scattering in general decreases monotonically an additional requirement on P_{T,Λ^0} will be most useful when extracting Λ_c^+ events.

The ((p,π^-),π^+)-triple mass spectrum obtained from the AROMA Monte Carlo is shown in figure 4.11 (left panel). The difference between the light and dark grey histograms is due to an additional requirement on P_{T,Λ^0}, which is confined to the range from 0.6 GeV to 0.88 GeV for the light histogram. The entries in the AROMA mass spectrum outside the Λ_c^+ peak correspond to partially reconstructed Λ_c^+ events, and thus can be used as a tag on the PGF processes. The background below the Λ_c^+ peak comes from Λ_c^+ particles that result in a Λ^0 via an intermediate Σ^0 and from Λ_c^+ particles where there are other decay products besides the Λ^0 and π^+. Notice that the extra requirement on P_{T,Λ^0} shifts the minimal mass of the system that can be reconstructed upwards. The minimum reconstructable mass depends on the lower limit for P_{T,Λ^0} and can be calculated from

$$M_{min}(\Lambda^0,\pi^+) = \sqrt{P_{T,\Lambda^0}^2 + M_{\Lambda^0}^2} + \sqrt{P_{T,\Lambda^0}^2 + M_{\pi^+}^2}. \tag{4.7}$$

A minimal mass of 1.88 GeV, corresponding to the value in the figure, is found after

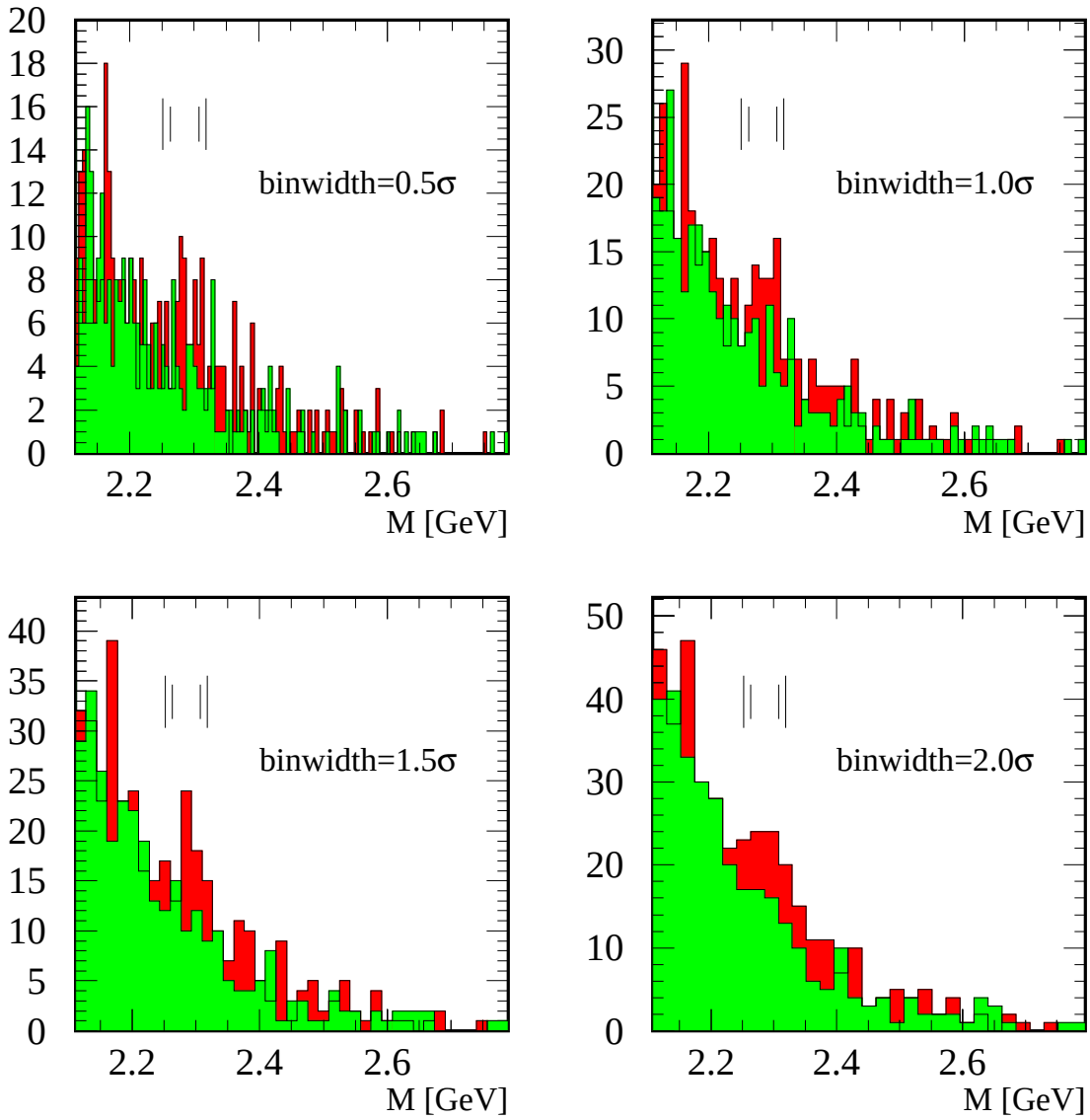

Figure 4.12: *Four mass spectra for a Λ^0 hyperon combined with a π^+ or π^- meson using bin widths equal to* 0.5, 1.0, 1.5 *and* 2.0 *times the nominal Λ_c^+ width (σ) from the Monte Carlo. The light grey (Λ^0,π^-) spectrum is plotted on top of the dark grey (Λ^0,π^+) spectrum. The transverse momentum P_{T,Λ^0} was required to lie in the interval from* 0.6 *GeV to* 0.88 *GeV. The four vertical lines denote the 2σ and 3σ regions around the Λ_c^+* PDG *mass with $\sigma = 11.1$ MeV. The spectra are obtained from the 1998, 1999 and 2000 data.*

substituting $P_{T,\Lambda^0} = 0.6$ GeV. Not shown in figure 4.11 but deduced from the left panel of the figure is the width of the Λ_c^+ peak, which amounts to $\sigma = 11.1 \pm 0.6$ MeV.

While the clear Λ_c^+ peak seen in the AROMA spectrum is hardly affected by the imposed requirements on P_{T,Λ^0}, a yield reduction near the Λ_c^+ mass is visible in the PYTHIA spectrum. Furthermore, no structure near the Λ_c^+ mass, that could lead to a false Λ_c^+ peak, is obtained with the PYTHIA Monte Carlo if the additional P_{T,Λ^0} requirement is imposed. This comparison demonstrates that the P_{T,Λ^0} requirements can be used when searching for Λ_c^+ events in the data. It also shows that the P_{T,Λ^0} constraints are very effective for partially reconstructed Λ_c^+ events leading to a modest reduction of the signal (left panel). This is further explored in section 4.5.

The experimental M(Λ^0,π^+) mass spectrum after imposing the additional requirement on P_{T,Λ^0} (0.6 GeV $< P_{T,\Lambda^0} <$ 0.88 GeV) and the stricter requirement on the collinearity (CL$>$ 0.99998) is shown in figure 4.12 for four different bin widths. (The other requirements on the data are similar to those described in section 4.3.1 for Ξ and $\Sigma^\star$ production.) The binning is set up such that the PDG mass lies in between two bins. In the figures an enhanced signal in the region of the Λ_c^+ mass is visible for each one of the chosen bin widths. The spectra containing the wrong charge combination, ($\Lambda^0\pi^-$), are also shown in figure 4.12. No evidence for a peak is seen in the wrong charge combination spectra, which shows that the values used for the P_{T,Λ^0} requirements do not explicitly lead to a peak structure. This confirms the aforementioned conclusion from the Monte Carlo study. It is noted that the (Λ^0,π^+) mass spectrum also contains Λ_c^+ strength outside the peak, which can be understood qualitatively in view of the Monte Carlo mass spectra displayed in figure 4.11.

Table 4.9: *Counts obtained in different regions of the (Λ^0,π^+) and (Λ^0,π^-) mass spectra near the Λ_c^+ peak at 2.285 GeV.*

$M_{p\pi^-\pi^+}$ range		Number of counts		$\frac{N_{(\Lambda^0,\pi^+)}}{N_{(\Lambda^0,\pi^-)}}$
bin width (in σ)	in GeV	N(Λ^0,π^+)	N(Λ^0,π^-)	
$[-6,-3]$	$[2.2184, 2.2517]$	33	28	1.18
$[-2,+2]$	$[2.2628, 2.3072]$	48	33	1.45
$[-3,+3]$	$[2.2517, 2.3183]$	74	47	1.57
$[+3,+6]$	$[2.3183, 2.3516]$	21	18	1.17

Comparison of the (Λ^0,π^+) spectrum with the (Λ^0,π^-) spectrum in figure 4.12 shows that the (Λ^0,π^-) spectrum can be used as an estimate of the background. In table 4.9 the counts in four different mass regions are given for the (Λ^0,π^+) and (Λ^0,π^-) spectra. The ratio of the number of counts in the four mass ranges for the two cases are

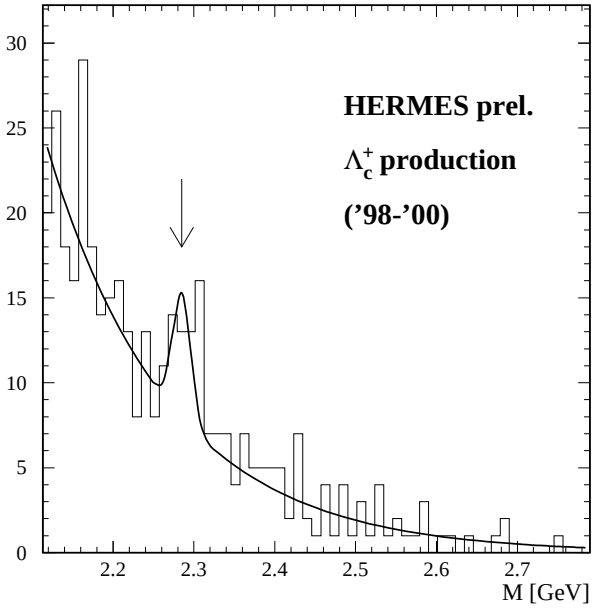

Figure 4.13: *(Λ^0,π^+)-pair mass distribution with fitted Gaussian with fixed position and width together with exponential background.*

also listed in the table. The ratio is observed to be significantly larger in the 2σ and 3σ ranges centered at the Λ_c^+ mass peak as compared to the sideband ranges. This provides additional evidence supporting the observation of an enhanced signal in the Λ_c^+ mass region. Due to the poor statistics and the small signal over background ratio for the Λ_c^+ the total yield depends on the method used to determine the background. Therefore, the background will be determined using different methods.

After subtraction of the wrong sign background 15±9, respectively 27±11, Λ_c^+ events are found within a two, respectively three, σ region surrounding the Λ_c^+ mass. Only the statistical error is given. Alternatively, the background can be determined from the $\Lambda^0\pi^+$ counts in the lower and upper side band mass regions, given in table 4.9, assuming a linear shape of the background, yielding 36 ± 4.9 and 54 ± 7.3 background counts in the two and three σ mass region around the Λ_c^+ mass, respectively. With these alternative background estimates 12 ± 9, and 20 ± 11, Λ_c^+ particles are found in the two and three σ mass regions, respectively, centered at the Λ_c^+ mass. If we take the average of these 4 determinations of the Λ_c^+ yield, we find 18 ± 9 counts.

It has also been tried to determine the Λ_c^+ yield by fitting the $(p\pi^-)\pi^+$ spectrum using a Gaussian shape with a fixed position (2.285 GeV) and width (11.1 MeV). The background is described using an exponential shape which is fitted through the mass spectra of figure 4.12 and through the spectra obtained after shifting the bins by half a bin width. In figure 4.13 the fit is shown for the one σ bin width, and in table 4.10 the number of Λ_c^+ particles resulting from the various fits is given. The average result

Table 4.10: *Determination of the yield of Λ_c^+ particles obtained from a fit using a Gaussian shape, with fixed position and width, together with an exponential shape. The fit was carried out for 8 spectra, which only differ in their binning. In four cases the same binnings is used as in figure 4.12 (with $M(\Lambda_c^+)^{\mathsf{PDG}}$ as bin border) and four times the bins where shifted by half a bin size. The uncertainties are taken from the fit.*

bin size	Counts	
$[\sigma]$	$M(\Lambda_c^+)^{\mathsf{PDG}}$ as bin border	$M(\Lambda_c^+)^{\mathsf{PDG}}$ as bin center
0.5	15.7 ± 7.2	9.9 ± 6.8
1.0	18.5 ± 7.0	13.3 ± 7.1
1.5	20.2 ± 7.3	16.5 ± 6.7
2.0	14.9 ± 7.4	18.4 ± 6.5
average	15.9 ± 7.0	

of $N_{\Lambda_c^+} = 15.9 \pm 7.0$ is in agreement with the estimates obtained after counting bins in different regions. It is chosen to use the latter number as a starting point for the evaluation of the Λ_c^+ photoproduction cross section discussed in section 4.3.3.

To quantify the uncertainty on the number of Λ_c^+ particles obtained from the (Λ^0,π^+) mass spectrum including the effect of the relatively large background the significance of the signal is determined. The significance is defined as $N_{sig}/\sqrt{N_{sig} + N_{bg}}$. It is a quantity which is inversely proportional to the uncertainty. Keep in mind that the denominator is a measure for statistical fluctuations. An average background of 49 ± 7 counts from the 8 fitted exponentials within the three σ region around the Λ_c^+ mass is obtained. From the above values for the signal and background a significance of 2.0 is obtained.

4.3.3 Λ_c^+ photoproduction cross section

In order to evaluate an estimate of the Λ_c^+ photoproduction cross section, the probability $\mathcal{P}_{\Lambda_c^+}$ that a generated Λ_c^+ particle is being detected has been calculated from events generated by the AROMA Monte Carlo program after tracking the simulated events through a model of HERMES. This probability factorizes into a part representing the branching ratios $\mathcal{P}^{B.R.}_{\Lambda_c^+}$, and a part that takes the acceptance of the detector into account $\mathcal{P}^{acc.}_{\Lambda_c^+}$. The first part which is intrinsic to the decay channel under consideration

is equal to $(0.58 \pm 0.18) \cdot 10^{-2}$ (see table 4.3).

The second part has been evaluated by S. Brons to be $0.37 \cdot 10^{-2}$ [57] under the assumption that $\mathcal{P}^{acc.}_{\Lambda_c^+}$ is equal to the product of the probabilities to detect a Λ^0 (3.26%) and a π^+(11.45%). In this evaluation possible correlations between the Λ^0 and π^+ yields are ignored. Using the same assumption the quoted value for $\mathcal{P}^{acc.}_{\Lambda_c^+}$ has been confirmed with the presently used Monte Carlo codes. However, the Λ^0 and π^+ yields are not uncorrelated, as can be seen from the probability for coincident detection of Λ^0 and π^+ particles in HERMES , which amounts to $0.22 \cdot 10^{-2}$ a number close to but different from the uncorrelated probability of $0.37 \cdot 10^{-2}$ quoted above. After imposing the same kinematic requirements as were applied to the data, and using a set of parameters describing the fragmentation function which are optimized for photoproduction [58] the probability for coincident $(\Lambda^0\pi^+)$ detection reduces to $0.123 \cdot 10^{-2}$. The reduction is primarily due to the omission - as compared to Ref. [57] - of the magnet tracks for the π^- candidates. For the event generation a charm mass of 1.35 GeV was assumed. Changing it to 1.2 GeV or 1.5 GeV gives a Λ_c^+ detection probability which is 12.9% lower or 16.7% higher, respectively. Therefore, a 15 percent uncertainty has been taken for the Λ_c^+ detection probability, $\mathcal{P}^{acc.}_{\Lambda_c^+}$. Combining the numbers given above, the probability for detection of a Λ_c^+ with the HERMES spectrometer is found to be $\mathcal{P}_{\Lambda_c^+} = (7.1 \pm 2.4) \cdot 10^{-6}$.

The Λ_c^+ electroproduction cross section follows from

$$\begin{aligned} \sigma^{lN \to \Lambda_c^+ \; X} &= \frac{N_{\Lambda_c^+}}{\mathcal{P}_{\Lambda_c^+} \epsilon^{photo}_{trig.} \mathcal{L}_{eff}} = \frac{15.9}{7.1 \cdot 10^{-6} \; 0.73 \; 221.92 \text{ pb}^{-1}} \\ &= (14 \; \pm \; 6_{stat} \; \pm \; 5_{syst}) \text{ nb}, \end{aligned} \tag{4.8}$$

where the effective luminosity over the years 1998, 1999 and 2000 is 221.92 pb^{-1} (see table 4.2) and 15.9 ± 7.0 was used as an estimate for the number of observed Λ_c^+ particles. For the statistical error the uncertainty in the number of observed Λ_c^+ particles is used and for the systematic error the uncertainty in the Λ_c^+ detection probability.

It is not possible to compare this electroproduction cross section with existing charm production cross sections as these data were obtained utilizing a real photon beam. Therefore, the electroproduction cross section is converted into a photoproduction cross section using the same method as employed by [51] and [56]. For this conversion it is assumed that the incoming lepton beam is equivalent to a broad spectrum of virtual photons, and that the associated photon spectrum is calculable in QED. Furthermore, the photoproduction cross section is assumed to depend linearly on the photon energy. With these assumptions the photoproduction and electroproduction cross sections are

related by

$$\sigma^{\gamma N}(\nu_0) = \frac{\sigma^{lN}}{\Phi}, \tag{4.9}$$

where ν_0 is equal to the flux weighted average energy, $\langle\nu\rangle$, under the assumption that the cross section depends linearly on the energy, and Φ is the integrated flux or flux factor. The values obtained in equations 6.26 and 6.27 from Ref. [51] are,

$$\Phi \;=\; 0.0260 \;\pm 0.0013, \tag{4.10}$$

$$\langle\nu\rangle \;=\; 15.5 \;\pm 1.0 \text{ GeV}. \tag{4.11}$$

These values are also applicable to the cross section for Λ_c^+ photoproduction at HERMES[4] [5]. Application to the Λ_c^+ electroproduction cross section $\sigma^{lN \to \Lambda_c^+ X}$ given by Eq. 4.8 results in a Λ_c^+ photoproduction cross section of

$$\sigma^{\gamma N \to \Lambda_c^+ X} = (538 \;\pm\; 231_{stat} \;\pm\; 188_{syst}) \text{ nb} \tag{4.12}$$

at a mean photon energy of 15.5 GeV. The uncertainty in Φ has been quadratically added to the systematic error.

As no previous Λ_c^+ photoproduction cross section measurements have been performed near threshold a direct comparison to other Λ_c^+ cross sections is not possible. For this reason the Λ_c^+ photoproduction cross section is shown in figure 4.14 together with other cross section measurements on open charm photoproduction. The curves in the figure are theoretical predictions based on PGF (as implemented in leading order in AROMA), and on a model using an effective Lagrangian [28] approach. In the figure a distinction is made between cross section measurements based on the explicit observation of a Λ_c^+ baryon (Alvarez et al [59] and present work, full symbols) and total charm cross sections derived from the observation of one or more D mesons. It is noted that the total charm cross sections are derived assuming a certain probability for a (anti)-charm quark to fragment into D-meson. As this probability is poorly known, the various data should be compared with care. For that reason, the other cross sections appearing in figure 4.14 are discussed in separate paragraphs below. The key question is whether the relatively high Λ_c^+ cross sections obtained in the present work is consistent with the total charm production cross section obtained elsewhere.

[4] Under the assumption that the photon is transversely polarized, I found $\Phi = 0.025$ and $\langle\nu\rangle = 15.5$.

[5] No model uncertainty has been includded in the error on $\langle\nu\rangle$. For Λ_c^+ hyperons simulated with the AROMA Monte Carlo $\langle\nu\rangle = 20$ GeV was found. As no flux factor could be obtained from the AROMA Monte Carlo it was decided to use the mean photon energy given in equation 4.11.

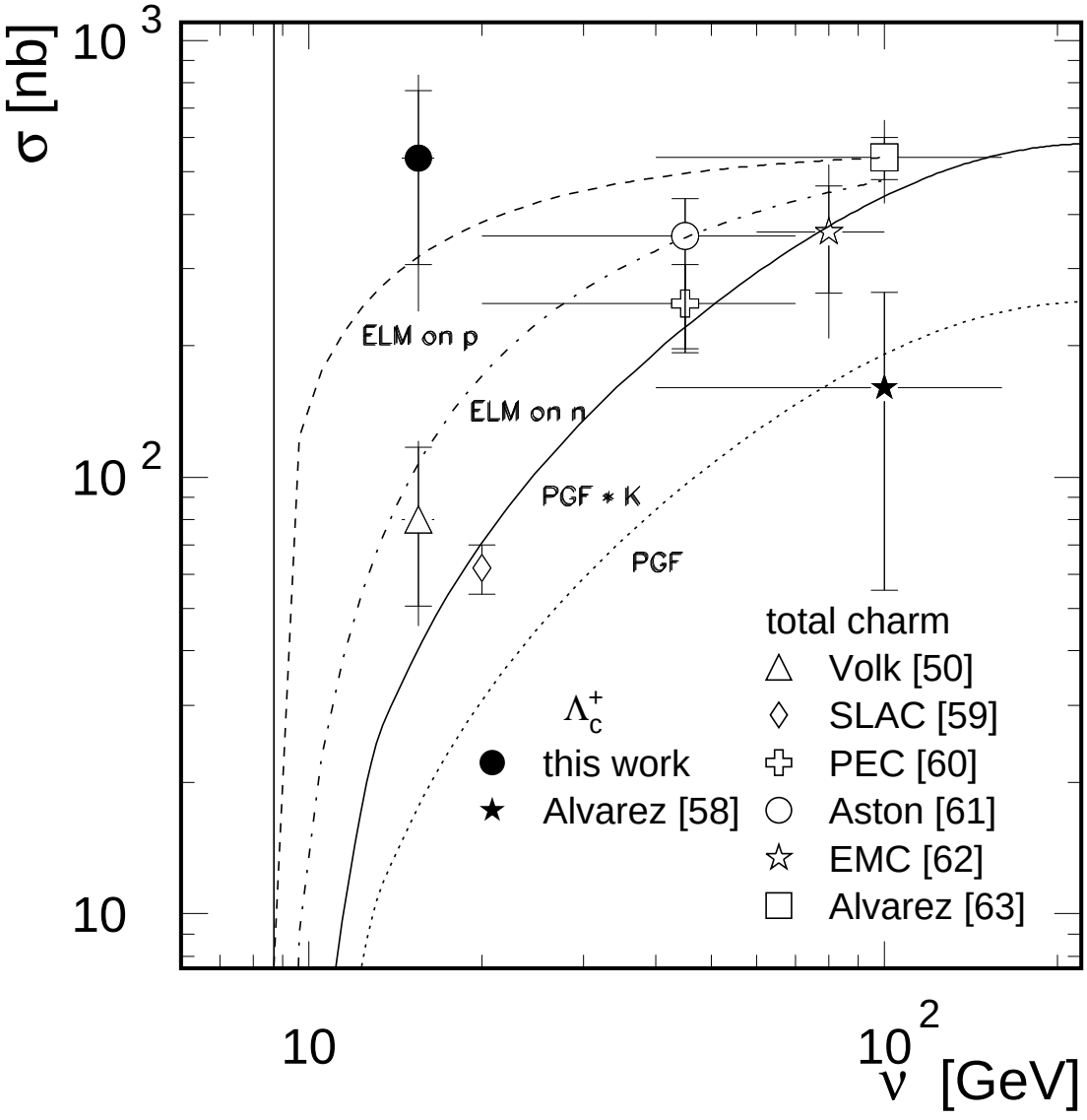

Figure 4.14: *Cross sections for charm photoproduction as a function of the photon energy ν. The filled symbols represent cross sections for Λ_c^+ production [59], while the open symbols [51, 60, 61, 62, 63, 64] are total charm cross sections derived from D meson production. The dashed and dash-dotted lines are taken from an effective Lagrangian model [28] for exclusive Λ_c^+ production on a p and n target, respectively, while the dotted line represents an LO* PGF *prediction with the charm mass set to* 1.5 *GeV. The solid line shows the same* PGF *prediction multiplied by a fudge factor K of* 2.3. *The threshold for open charm production at* 8.71 *GeV is represented by a vertical line.*

Alvarez et al [59] obtained a value for $BR \times \sigma^{\gamma N \rightarrow \Lambda_c X}$ of (8 $\pm$ 5) nb using the pKπ decay channel at a mean photon energy of 105 GeV. From this value a Λ_c^+ photo-production cross section of (160 $\pm$ 100) nb was derived assuming a branching ratio for this decay channel of 0.05 $\pm$ 0.01 [55]. The obtained cross section is below the Λ_c^+ cross section determined in this work. Taken on face value this suggests the existence of a Λ_c^+ threshold enhancement. In Ref. [65] such an enhancement is suggested as an explanation for a bump with a height of several μb observed in the total photo-production cross section on a proton target at a photon energy of about 10 GeV. However, in Ref. [66] an upper limit for such a charm production enhancement near threshold of 270 to 450 nb is reported, based on the observation of $\gamma p \rightarrow D^- \Sigma_c^{++}$ events (where only the D^- meson is explicitly detected), and similar channels using a 10 GeV photon beam. It is stressed though, that this upper limit (which is consistent with our measurement) is not based on the observation of a Λ_c^+ baryon. Since no other Λ_c^+ photoproduction cross section data on a nucleon are available the other existing data are all based on D-meson production.

At SLAC [60] the total open charm cross section was derived from the measurement of D-mesons produced with a real photon beam and observed in a bubble chamber. From a $D\bar{D}$ photoproduction cross section of

$$\sigma^{\gamma N \rightarrow D\bar{D} X} = (17^{+8}_{-6}) \text{ nb} \tag{4.13}$$

they obtained a value for the total open charm photoproduction cross section of

$$\sigma^{\gamma N \rightarrow c\bar{c} X} = (62 \pm 8^{+15}_{-10}) \text{ nb} \tag{4.14}$$

at a photon energy of 20 GeV. This cross section strongly depends on the assumed fraction of D-mesons produced (and detectable) in $c\bar{c}$-production. From the observed $D^{*\pm}$ meson yield at HERMES a photoproduction cross section of

$$\sigma^{\gamma p \rightarrow c\bar{c} X} = (37.1^{+16.9}_{-13.3\ stat} \pm 2.6\ _{MC\ stat}) \text{ nb} \tag{4.15}$$

at a mean photon energy of 15.5 GeV can be deduced (Ref. [51]). Using an Ansatz similar to that of Ref. [60] for $c\bar{c} \rightarrow$D fragmentation a value for the open charm cross section of

$$\sigma^{\gamma p \rightarrow c\bar{c} X} = (79.9^{+37.0}_{-29.2\ stat} \pm 8.4\ _{syst/exp} \pm 16.0\ _{syst/frag}) \text{ nb} \tag{4.16}$$

could be determined. Both experiments rely on a Monte Carlo estimate of the total charm to D-meson production cross section ratio. There is, however, evidence in the literature suggesting that the models used for estimating charm fragmentation are incorrect. For instance in Ref. [67] it is reported that the fragmentation program

JETSET 7.3 (which is also used in AROMA albeit version 7.4) is not able to reproduce the relative yield of Λ_c^+, $\bar{\Lambda_c}^-$, $\overline{\mathrm{D}}^0$ and D^- as observed in two-jet $e^+e^- \to c\bar{c}$ events at $\sqrt{s} = 10$ GeV. The data give a factor 3 more Λ_c^+ yield as compared to the Monte Carlo. Furthermore, in [59] it is shown that the observed Λ_c^+/D production ratio in different experiments is a factor 2 to 4 higher than expected from the Monte Carlo. It is of interest to note that a factor 4 enhancement of the Λ_c^+/D fragmentation ratio would bring the HERMES results for total charm production based on either Λ_c^+ baryons or D-mesons ([51]) in agreement with each other.

The total charm photoproduction curve in figure 4.14 represented by the dotted line is based on LO PGF and produced by the AROMA Monte Carlo code. The curve is below the data. Multiplication of this curve with a fudge factor of 2.3 to take higher order contributions to the PGF cross section into account gives the solid line which describes the data well at high energy. It is noted that the dotted curve in figure 4.14 will also shift up if the charm mass in AROMA is lowered, especially near threshold energies but this has not been pursued. It is concluded that the LO PGF cross section is about a factor 28 ± 12 below the photoproduction cross section for the Λ_c^+ baryon as determined in this work.

The dashed (for the proton) and dash-dotted (for the neutron) curves in figure 4.14 are calculated by [28] using an effective Lagrangian model (ELM) for the exclusive photoproduction of charmed particles near threshold. The only parameters entering this model are a coupling constant $g_{\mathcal{N}\mathcal{B}_\mathrm{C}\mathcal{D}}$ for the vertex of nucleon-charmed baryon-D meson interactions, and the anomalous magnetic moment κ_c of the charmed baryon. As can be seen in Eq. 2.33 the quantity $g_{\mathcal{N}\mathcal{B}_\mathrm{C}\mathcal{D}}$ is effectively a normalization factor. For the curves displayed in figure 4.14 $g_{\mathcal{N}\mathcal{B}_\mathrm{C}\mathcal{D}} = 1$ and $\kappa_c = 0.86\ \mu_\mathrm{N}$ was taken. Besides the channels $\gamma\mathrm{p} \to \Lambda_c^+\overline{\mathrm{D}}^0$ and $\gamma\mathrm{n} \to \Lambda_c^+\mathrm{D}^-$ the exclusive production of Σ_c^{++} and Σ_c^+ baryons on a proton target and Σ_c^+ and Σ_c^0 production on a neutron target are also calculated in Ref. [28]. As the Σ_c baryon decays almost completely into a Λ_c this contribution is added to the Λ_c curve, for each of the two targets. The result roughly corresponds to the curves given in the figure scaled up by a factor three. Altogether it is concluded that the effective Lagrangian model is in good agreement with the Λ_c^+ cross section found in this work. However, the values for $g_{\mathcal{N}\mathcal{B}_\mathrm{C}\mathcal{D}}$ and κ_c used in [28] which are listed above are not a priori known. Data of the type presented in this thesis can be used to fix such parameters.

In the effective Lagrangian model the dynamics appearing at the parton level are untouched as the entire problem is treated at the meson-baryon level. This is in contrast to PGF (as used in AROMA) where the calculation is performed at the partonic level. For this reason it is not possible to combine the two models. At best one can argue

that the ELM result effectively captures the higher order corrections not contained in the LO PGF calculations.

Another process contributing to exclusive Λ_c^+ production is quark interchange [27] QI, introduced as a source of contamination for the measurement of $\Delta G/G$. In principle this process could also contribute to the obtained Λ_c^+ cross section. However, the QI process is believed to result in less transverse momentum for the Λ_c^+ baryon [68] than the PGF process. Therefore, the P_T-cut applied to the data may effectively have removed the QI contribution. As no event generator was available for the QI process, this could not be verified using a Monte Carlo simulation. Alternatively, it has been tried to look for a Λ_c^+ peak in different ranges of the transverse momentum of the Λ_c^+. However, the statistics are insufficient to split up the data in more than one P_T bin.

Although the Λ_c^+ photoproduction cross section near threshold has not been determined with great precision, the value found in this work is surprisingly high. Possible reasons to explain this are a threshold enhancement in charm photoproduction [65], Λ_c^+ baryons produced via other mechanisms than contained in leading order PGF, or QI . It is also observed that the total charm cross section near threshold usually quoted in the literature might well be low due to an inadequate description of the fragmentation probabilities of charmed quarks into charmed hadrons. The small significance of the Λ_c^+ signal implies that the cross section $\sigma^{lN\to\Lambda_c^+\ X}$ should be handled with care. For this reason it would be desirable to obtain additional data. A significance of 3.0 for the Λ_c^+ peak can be achieved roughly by doubling the statistics used in this analysis.

4.4 Spin asymmetries for Ξ and $\Sigma^\star$ hyperon production

Using the results obtained in section 4.3 for Ξ and $\Sigma^\star$ photoproduction, the double spin asymmetry for the production of these hyperons is determined. These asymmetries are of importance since the hyperons involved each have a different quark content and can thus provide information on the polarization of individual quark flavors in the nucleon. It should be noted, however, that this method is not expected to be competitive with the usual methods used to decompose the flavor dependence of the nucleon spin, since (i) the production mechanism may involve more than 1 process which will typically wash out the asymmetries; (ii) in photoproduction the x-dependence cannot be measured; and (iii) the statistics is low.

Nevertheless, it is of interest to evaluate the asymmetries in particular for the Ξ^+ (Ξ^+=$\bar{d}\bar{s}\bar{s}$) and the $\overline{\Sigma}^{\star\pm}$ hyperons which are all-sea objects. Assuming that these

hyperons are produced by scattering off an sea anti-quark, the asymmetry gives information on the sea quark polarization. This information is otherwise hard to obtain.

From the counts obtained with the beam and target polarization oriented parallel ($\uparrow\Uparrow$) or anti-parallel ($\downarrow\Uparrow$) an asymmetry can be built:

$$A_{\parallel} = \frac{N_s^{\downarrow\Uparrow} - N_s^{\uparrow\Uparrow}}{N_s^{\downarrow\Uparrow} + N_s^{\uparrow\Uparrow}}, \tag{4.17}$$

where $N_s^{\uparrow\Uparrow}$ and $N_s^{\downarrow\Uparrow}$ are the number of counts obtained with the beam and target polarizations oriented parallel and anti-parallel. On page 37 it was shown that the asymmetry obtained with the luminosity detector is zero within errors when all data from '98 - '00 are taken together. Therefore, no luminosity weighting has been performed for the determination of $A_{\parallel}$. The subscript s denotes signal and will in this section mean the count rate of the hyperon under consideration, after background subtraction.

The number of counts needed to calculate the asymmetry is obtained from the appropriate interval in the (p, π^-, π) and $(\overline{p}, \pi^+, \pi)$ mass distributions. Events tagged with a Λ hyperon give the number of signal plus background events. The number of background events is determined by requiring M(p,π) outside the Λ mass interval. For the Ξ mass interval the PDG mass value plus or minus 3σ ($\sigma = 3.1$ MeV as taken from table 4.8) is used, and for the Σ* the mean mass plus or minus the full width (both from [55]) defines the interval. In table 4.11 the actual mass ranges used are given together with the counts obtained from the mass spectra for the two relative polarization states. In the column labeled Λ candidates the number of counts is a combination of signal and background. In the column where the (p,π^-)-pair was required not to be a Λ an estimate of the background is given, while the mass regions in which the counting is performed are also given in the table. The normalization regions for the background estimate are the same as the one mentioned in section 4.3.1.

From the number of counts listed in table 4.11 two different asymmetries are evaluated which are listed in table 4.12. After subtraction of the number of counts outside the Λ region from the number of counts inside the Λ region for the same relative spin orientation the raw asymmetries $A_{||}^{NBG}$ for the Ξ and Σ* hyperons are obtained. It is realized that the background obtained from the number of counts outside the Λ peak may also have an asymmetry which can influence the extracted asymmetry $A_{||}^{NBG}$ due to the relatively small signal over background ratio. In order to study this effect the asymmetry has also been calculated using a background which has been averaged over the two polarization states. The result is listed as $A_{||}^{aver}$ in table 4.12.

Table 4.11: *Number of counts obtained in the mass regions where* Ξ *and* $\Sigma^\star$ *hyperons are observed. In the columns marked* Λ *candidate the mass of the* (p,π^-) *or* $(\overline{p},\pi^+)$ *pair was required to be between* 1.108 *GeV and* 1.123 *GeV. For the column where no* Λ *candidate was required the mass intervals ranged from* 1.08 *GeV to* 1.103 *GeV and from* 1.13 *GeV to* 1.17 *GeV.*

Particle	mass interval	Λ candidate		no Λ candidate	
	[MeV]	anti-parallel	parallel	anti-parallel	parallel
Ξ^-	$[1312.0, 1330.6]$	958	957	580	620
$\Sigma^{\star-}$	$[1347.8, 1426.6]$	4003	3961	3210	3091
$\Sigma^{\star+}$	$[1347.0, 1418.6]$	2541	2611	2142	2173
$\overline{\Sigma}^{\star-}$	$[1347.0, 1418.6]$	478	464	379	322
Ξ^+	$[1312.0, 1330.6]$	206	199	90	96
$\overline{\Sigma}^{\star+}$	$[1347.8, 1426.6]$	760	695	502	543

For the double spin asymmetries of the Ξ^-, $\Sigma^{\star-}$, $\Sigma^{\star+}$, Ξ^+ and $\overline{\Sigma}^{\star+}$ hyperons consistent results are obtained for the two different background subtraction methods. The difference between the asymmetries obtained from the two methods shows no systematic effect for these five hyperons. Furthermore the asymmetries of the $\Xi^\pm$ and $\Sigma^{\star\pm}$ are each consistent with zero while a positive asymmetry is found for the $\overline{\Sigma}^{\star+}$ for both background subtraction methods. For the $\overline{\Sigma}^{\star-}$ the two background subtractions show a large influence on the subtraction method used. The average of these is, however, consistent with zero. In this case ($\overline{\Sigma}^{\star-}$) the inconsistency of $A_{||}^{NBG}$ and $A_{||}^{aver}$ also reflects the large uncertainties in the yield of this hyperon due to the background subtraction problems for this hyperon discussed in sect 4.3.

In the last column of table 4.12 the actual double-spin asymmetries for 5 of the 6 hyperons are listed using

$$A_1 \;=\; \frac{1}{\langle P_{Target} P_{Beam}\rangle \langle D\rangle} A_{||}^{aver}. \tag{4.18}$$

where $\langle P_{Target} P_{Beam}\rangle = 0.476$ and the average depolarization factors have been calculated for each particle separately using the PYTHIA Monte Carlo. It ranges from 0.57 to 0.76 where the lower limit applies to the hyperons and the upper limit to the anti-hyperons.

No value for A_1 is listed for the $\overline{\Sigma}^{\star-}$ hyperon as no stable result for $A_{||}$ could be

Table 4.12: *Double-spin asymmetries for the Ξ and Σ^0 particles after normal background subtraction $A_{||}^{NBG}$, and after subtraction of a background averaged over the relative polarization states $A_{||}^{aver}$.*

Particle	quark content	$A_{||}^{NBG}$	$A_{||}^{aver}$	A_1
Ξ^-	dss	0.06 ± 0.06	0.00 ± 0.05	0.00 ± 0.18
$\Sigma^{\star-}$	dds	-0.05 ± 0.06	0.03 ± 0.04	0.11 ± 0.14
$\Sigma^{\star+}$	uus	-0.05 ± 0.09	-0.08 ± 0.07	-0.3 ± 0.3
$\overline{\Sigma}^{\star-}$	$\bar{u}\bar{u}\bar{s}$	-0.18 ± 0.11	0.06 ± 0.09	
Ξ^+	$\bar{d}\bar{s}\bar{s}$	0.05 ± 0.08	0.03 ± 0.08	0.1 ± 0.2
$\overline{\Sigma}^{\star+}$	$\bar{d}\bar{d}\bar{s}$	0.26 ± 0.08	0.16 ± 0.07	0.44 ± 0.19

obtained. In most other cases A_1 is consistent with zero , while for $\overline{\Sigma}^{\star+}$ production a positive value is observed. The asymmetries observed for the various hyperons cannot be compared to existing predictions as these are not available. In general the interpretation of these asymmetries is complicated because various processes may contribute to the production of the Ξ and $\Sigma^\star$ hyperons:

- direct coupling of the photon to a pre-existing quark in the nucleon.
- photon-gluon fusion, i.e. the photon splits into a quark-antiquark pair, of which one interacts through gluon exchange with an other quark in the nucleon. (see fig. 4.1)
- production of a heavier hyperon which decays into one of the observed Ξ or $\Sigma^\star$ hyperons.

As both PGF and heavy meson production are suppressed at our energy scale, it is likely that the direct coupling is dominant (a careful Monte Carlo study is required to confirm this Ansatz). The initial coupling will typically involve the quark flavor of which two are present in the hyperon (s in Ξ^-, $\bar{d}$ in $\overline{\Sigma}^{\star+}$, etc.). If this is true, the asymmetries measured imply that the quark polarizations at very low x ($\sim 3 \cdot 10^{-3}$) are mostly zero, which is consistent with existing data on Δu, Δd and Δq_{sea} (see [6]). It also implies that the strange quark polarization is zero at low x, which represents new information. Most surprisingly, however, is the observation that $\Delta\bar{d}$ could be large and positive at very low x since we measured that $A_{\overline{\Sigma}^{\star+}} \approx 0.44 \pm 0.19$. This is potentially a very interesting observation since it leads, under the assumption that $A_{\overline{\Sigma}^{\star-}}$ is consistent with zero[6], to

[6] Although no value for $A_{\overline{\Sigma}^{\star-}}$ is given in table 4.12 the assumption that $A_{\overline{\Sigma}^{\star-}} \approx 0$ appears reasonable

the conclusion that the quantity $\Delta\bar{u} - \Delta\bar{d} < 0$ at very low x. The quantity $\Delta\bar{u} - \Delta\bar{d}$ is also accessible at HERMES in semi inclusive DIS analysis. In Ref. [69] it was found to be consistent with zero with large error bars, i.e. not inconsistent with the present result. In Ref. [70], on the other hand, $\Delta\bar{u} - \Delta\bar{d}$ was predicted to be positive using an instanton model for the quark structure of the nucleon. Therefore, the obtained double spin asymmetries for the $\overline{\Sigma}^{\star+}$ and the $\overline{\Sigma}^{\star-}$ hyperons might possibly reject this model. However, while these arguments show the potential interest in measurements of this kind, careful Monte Carlo studies involving each of the mentioned mechanisms are needed before more definite conclusions can be drawn.

4.5 Spin asymmetries for partially reconstructed Λ_c^+ baryons

The number of counts obtained in the complete reconstruction of the Λ_c^+ baryon through the $\Lambda^0\pi^+$ decay is insufficient for an asymmetry calculation. Therefore, more Λ_c^+ decay channels need to be taken into account. In table 4.13 the Λ_c^+ decay channels involving a Λ^0, or a Σ^0 subsequently decaying into a Λ^0 and a γ, and at least one π^+ are given. The Σ^0 decays almost exclusively into a Λ^0 and γ (B.R. $\approx 100\%$). Instead of reconstructing the Λ_c^+ baryon for each of these decay channels, only a partial reconstruction of the final state, i.e. the Λ_c^+ baryon, is presented in this section. In the data we require a Λ^0 and a π^+ to reconstruct a (Λ^0,π^+)-spectrum. To determine the fraction of events coming from a Λ_c^+ baryon, Monte Carlo simulations for both Λ_c^+ production and the background are performed.

The simulations are used to identify a kinematic domain which is likely dominated by partially reconstructed Λ_c^+ events. For these events a double-spin asymmetry is determined.

When searching for partially reconstructed Λ_c^+ baryons, we consider the $\Lambda^0\pi^+$-spectrum in the invariant mass range from 1.45 GeV to 2.32 GeV. The lower limit on the mass range is needed to exclude the $\Sigma^{\star+}$ from the sample and the upper mass limit corresponds to the PDG Λ_c^+ mass plus 3σ with $\sigma = 11.1$ MeV as taken from the Monte Carlo (see Sect. 4.3.2).

From the analysis which led to the complete reconstruction of the Λ_c^+ baryon it is clear that the transverse momentum P_{T,Λ^0} of the Λ^0 with respect to the Λ_c^+ direction is a good quantity to put restrictions on in order to improve the signal. In the case of partially reconstructed Λ_c^+ events this is also true albeit less pronounced. This can be

in view of the values for $A_{||}^{NBG}$ and $A_{||}^{aver}$ listed in the same table.

Table 4.13: *Λ_c^+ decay channels involving a Λ^0 or Σ^0 hyperon in the final state with their branching ratios as taken from [55]. As the Σ^0 decays predominantly to a $\Lambda^0\gamma$ (B.R.= $99.51 \pm 0.05\%$), all the listed decays are included when a $\Lambda^0\pi^+$ final state is considered.*

decay channel	B.R.
$\Lambda^0\pi^+$	0.0090 ± 0.0028
$\Lambda^0\pi^+\pi^0$	0.036 ± 0.013
$\Lambda^0\pi^+\pi^+\pi^-$	0.033 ± 0.010
$\Lambda^0\pi^+\eta$	0.018 ± 0.006
$\Sigma^0\pi^+$	0.0099 ± 0.0032
$\Sigma^0\pi^+\pi^0$	0.018 ± 0.008
$\Sigma^0\pi^+\pi^+\pi^-$	0.012 ± 0.004
total	0.14 ± 0.02

understood by considering the decay in the Λ_c^+ rest frame. As more decay products are present less energy is available per decay product because the energy is shared with more particles, and because it results in a smaller mass difference between the initial and final state particles. Thus the average momentum for a decay product becomes smaller as compared to the 2-body $\Lambda^0\pi^+$ decay which consequently means a lower average transverse momentum with respect to the Λ_c^+ direction.

Another quantity, not used so far, to put requirements on is the transverse momentum P_{T,Λ_c^+} of the Λ_c^+ baryon with respect to the (virtual) photon or beam direction. The motivation to place requirements on P_{T,Λ_c^+} is the relatively large transverse momentum of charm quarks produced by the PGF mechanism that hadronize into a Λ_c^+ baryon.

For nine different intervals in $(P_{T,\Lambda^0}, P_{T,\Lambda_c^+})$-space the (Λ^0,π^+) signal, where the Λ^0 originates from a Λ_c^+ decay, and the (Λ^0,π^+)-background yields are generated using Monte Carlo simulations. The signal events originate from a charm PGF event generated with the AROMA Monte Carlo. The mass of the charm quark was set to 1.35 GeV. The background is generated with the PYTHIA event generator. The normalization of the Monte Carlo results is not taken from the generator programs themselves as AROMA was shown to underestimate the Λ_c^+ photoproduction cross section by a factor 27.4 (see section 4.3.2), while PYTHIA was seen to overestimate the $\Sigma^{\star+}$ ($\rightarrow \Lambda^0\pi^+$) cross section by a factor 7.3 (see sect. 4.3). For this reason we have multiplied the Monte Carlo results by factors of 27.4 and 1/7.3, respectively. The results are expressed in μb for both signal and background events, and listed in table 4.14 together with the S/B

Table 4.14: *Signal and background yield together with their ratio from Monte Carlo for nine intervals in (P_{T,Λ^0},P_{T,Λ_c^+})-space. The normalization of the signal events is determined from the Λ_c^+ cross section found in this work (see Eqn. 4.8). The normalization of the background events is based on the $\Sigma^{\star+}$ yield from the* PYTHIA *Monte Carlo compared to the yield found in the data (see table 4.8).*

P_{T,Λ_c^+} [GeV]	P_{T,Λ^0} [GeV]	S	B	S/B
$[0.0, 0.6]$	$[0.0, 0.3]$	$1.4 \cdot 10^{-6}$	$1.2 \cdot 10^{-5}$	0.11
	$[0.3, 0.6]$	$2.1 \cdot 10^{-6}$	$1.2 \cdot 10^{-5}$	0.17
	$[0.6, 0.9]$	$2.9 \cdot 10^{-7}$	$6.0 \cdot 10^{-7}$	0.49
$[0.6, 1.2]$	$[0.0, 0.3]$	$1.1 \cdot 10^{-6}$	$5.4 \cdot 10^{-6}$	0.20
	$[0.3, 0.6]$	$1.3 \cdot 10^{-6}$	$2.9 \cdot 10^{-6}$	0.45
	$[0.6, 0.9]$	$1.8 \cdot 10^{-7}$	$1.3 \cdot 10^{-7}$	1.4
$[1.2, 1.8]$	$[0.0, 0.3]$	$1.2 \cdot 10^{-7}$	$2.4 \cdot 10^{-7}$	0.51
	$[0.3, 0.6]$	$1.4 \cdot 10^{-7}$	$1.2 \cdot 10^{-7}$	1.2
	$[0.6, 0.9]$	$4.0 \cdot 10^{-8}$	$1.3 \cdot 10^{-8}$	3.1

ratios evaluated from these values (before they where rounded). From the table it can be seen that the PGF signal improves (as compared to the background) from 0.11 at lowest P_T values to 3.1 at the highest P_T values. It is concluded that transverse momentum requirements are very effective in isolating PGF events. It should be realized, however, that the absolute value of the quoted S/B ratios is uncertain. The quoted renormalization factors of AROMA and PYTHIA are not rigorously determined in the absence of precise charm production cross sections at threshold and in view of the difficulties (see sect. 4.3.1) in reproducing the $\Lambda^0\pi$ spectrum. Moreover, the AROMA Monte Carlo results depend on the value of the charm mass. For example, the P_{T,Λ_c^+} distribution is shifted to larger values (and hence the S/B ratios increase) if the charm mass is reduced from 1.35 GeV to 1.2 GeV.

The same intervals for P_{T,Λ^0} and P_{T,Λ_c^+} as used for table 4.14 are used for the determination of the asymmetries shown in figure 4.15. The other requirements used are the same as for the reconstruction of the Λ_c^+ peak (see sect. 4.3).

The asymmetry is determined from the number of Λ^0 hyperons observed in coincidence with a π^+ meson found for the relative polarization states of the target and beam. The counts are taken within three standard deviations of the center of the

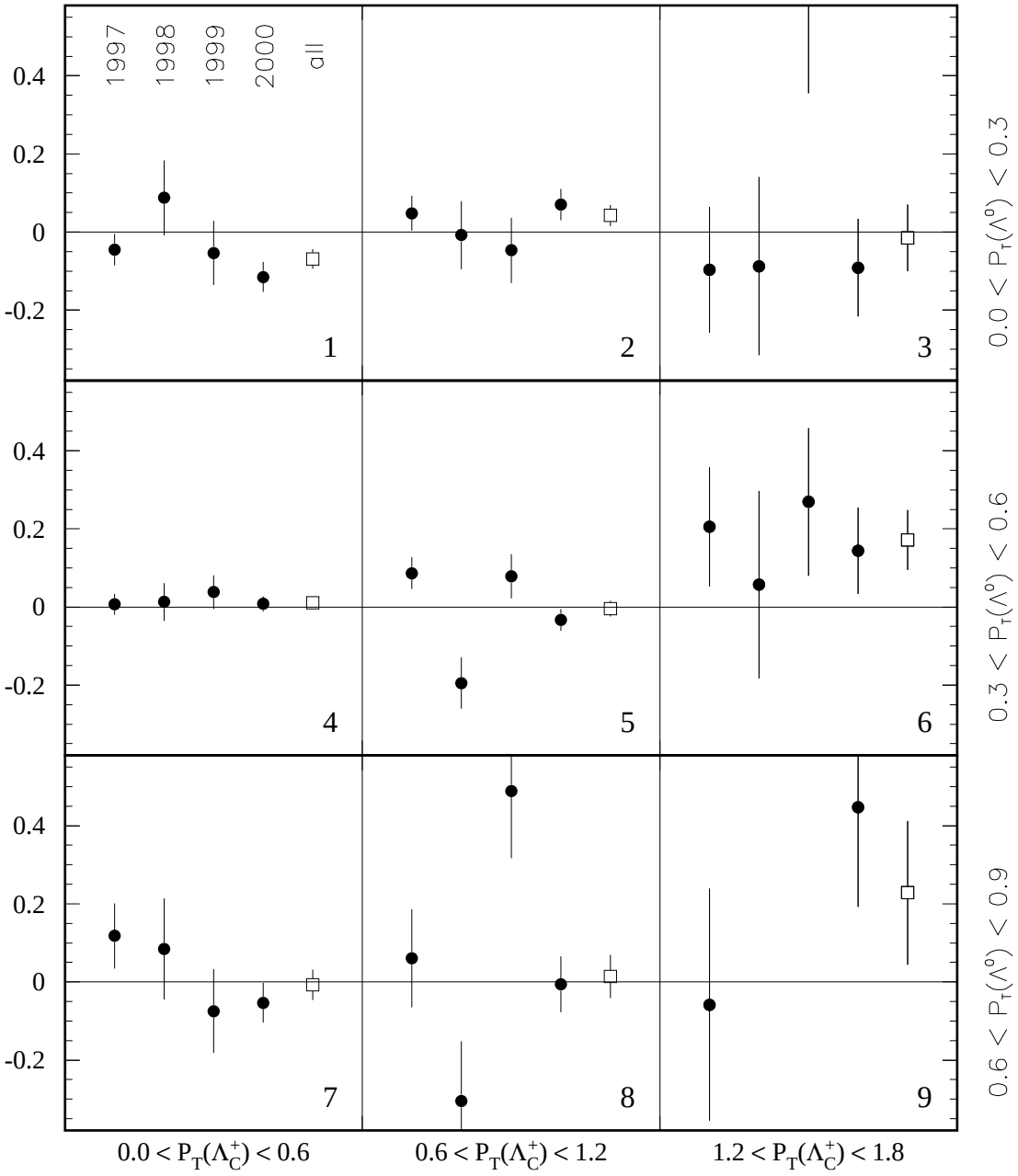

Figure 4.15: *Raw asymmetries for a Λ^0 hyperon tagged with a π^+ meson. The mass of the (Λ^0,π^+)-system ranges from 1.45 GeV to 2.32 GeV. The errors are statistical only. No data are shown for 1998 and 1999 in the right-lower panel (9) due to lack of statistics. The rightmost data point in each panel (open symbols) represents the 4-year average.*

Λ^0 mass peak as determined from fits for each year separately. The Λ^0 peak widths (σ values) are given in table 4.15. The subtracted background is determined from the

Table 4.15: *Value for the standard deviation obtained after fitting a Gaussian shape for the signal plus a first order polynomial for the background through the π^+-tagged Λ^0 mass spectra for four different data-taking periods. The different values for the widths are due to changes in the* HERMES *detector set-up. Notably, in 1998 a* RICH *detector was installed, which caused a deterioration of the resolution.*

year of data-taking	σ [MeV]
1997	1.99
1998	2.24
1999	2.65
2000	2.52

counts in the mass region which is 5σ to 9.5σ away from the PDG Λ^0 mass. The mass of the Λ^0 π^+ system had to be above 1.45 GeV and under 2.32 GeV as explained before.

In each of the nine panels of figure 4.15 the asymmetry derived from each of the four years for which data were analyzed, is shown separately with 1997 always the first point on the left. If there is no data point displayed no events are found for one or both of the relative polarization states. From the figure it can be seen that the asymmetries obtained in the different years generally agree within their errors. However, the 1998 values are low compared to the all-years average in two panels, and the 1999 values are high in two other cases. It is noted, however, that several 2σ and 3σ deviations are to be expected in a collection of 36 independent measurements. For that reason, the outlying data points are considered to be the result of statistical fluctuations. To arrive at the asymmetry for the complete data sample, shown as the rightmost data point in each panel, the counts obtained in the four years are first added for each combination separately, where-after the asymmetry calculation is performed.

As both electron and positron beams, and both hydrogen and deuterium targets were used over the four years investigated, we need to consider whether these differences might affect the measured asymmetry. An effect coming from the beam lepton is unlikely since the available energy is too low for Z or W exchange which otherwise could cause differences between electron and positron scattering. The effect of using two different targets was investigated by simulating events with the PYTHIA Monte Carlo for a proton and a neutron target. No significant difference for the production of (Λ^0,π^+)-

pairs was observed (see table 4.7). With the AROMA Monte Carlo lepton scattering on only a proton can be simulated. However, application of an isospin transformation (exchange of u and d quarks) on the proton can be used to simulate scattering on a neutron. At the threshold for production of a Λ_c^+ baryon in lepton-proton scattering an associated $\overline{\mathrm{D}}^0$ meson will be produced. The isospin transformed process corresponds to the production of a Λ_c^+ baryon associated with a D^- meson on a neutron target. As the difference in the masses of the $\overline{\mathrm{D}}^0$ ($\mathrm{M}(\overline{\mathrm{D}}^0)$=1864.5 MeV) and D^- ($\mathrm{M}(\mathrm{D}^-)$=1869.3 MeV) mesons is only a few MeV the cross section of the Λ_c^+ baryon on a neutron target is expected to be similar to that on a proton target. Therefore, there is no reason for not adding the results of the four different years of data taking.

In section 4.2 it was found that the double spin asymmetry of the events collected with the luminosity monitor was consistent with zero, as it should be since no special requirements were made. In order to arrive at a double spin asymmetry different from zero a spin dependent scattering process should occur such as scattering of polarized, i.e. spin-aligned quarks or gluons in the proton. In figure 4.15 the asymmetries for the combined data set are equal to zero in most panels, as expected for background processes such as heavy hyperon production (see sect. 4.4). However, we observe 2 exceptions. In the upper left panel a small negative asymmetry is found, and in the upper middle, middle right and lower right panel a small positive asymmetry is found. In view of the results displayed in table 4.14 the small asymmetries in two upper panels cannot be connected to PGF, but are more likely connected to different mixtures of hyperon production processes in which the P_{CM}^{max} is much lower (see table. 4.4) and the asymmetries are close to zero (see table 4.12). Moreover, according to PYTHIA there is no evidence of specific channels dominating the events of the two upper panels, where an asymmetry can be observed. Therefore, no further attempts have been made to understand the cause of these small asymmetries. Since the S/B ratio for the PGF process was shown to increase when going from the upper left panel in figure 4.15 to the lower right panel (table 4.14) an asymmetry that can be associated with the PGF process is only expected in panels 6, 8 and 9, each corresponding to high P_T values for the Λ^0 and Λ_c^+. As indeed a non-zero double spin asymmetry is observed in panel 6 and 9, while no such asymmetries are seen in the preceding panels it is possible to associate the asymmetry partially with the PGF process.

Let us therefore examine the actual number of counts obtained in the nine areas in (P_{T,Λ^0},P_{T,Λ_c^+})-space. For this the counts are first expressed in μb such that comparisons with table 4.14 are easily made. For the determination of the ratio between the yields from the two Monte Carlo programs and the data the values listed in table 4.14 are used.

Table 4.16: *Number of π^+-tagged Λ^0 counts in the two relative beam-target polarization states for nine intervals in (P_{T,Λ^0},P_{T,Λ_c^+})-space, together with their sum. The total number of counts is also expressed in μb for comparison with table 4.14. The conversion factor of 257.89 pb^{-1} is taken from table 4.2. The ratio of the number of counts from the data and from the* PYTHIA *and* AROMA *Monte Carlos are given in the last two columns.*

P_{T,Λ_c^+} [GeV]	P_{T,Λ^0} [MeV]	$N^{\downarrow\Uparrow}$	$N^{\uparrow\Uparrow}$	N^{sum}		$\frac{N_{PYTHIA}}{N_{DATA}}$	$\frac{N_{AROMA}}{N_{DATA}}$
					[μb]		
[0.0, 0.6]	[0.0, 0.3]	607.1	711.5	1319	$5.11 \cdot 10^{-6}$	2.43	0.26
	[0.3, 0.6]	2283	2213	4496	$1.74 \cdot 10^{-5}$	0.74	0.12
	[0.6, 0.9]	300.8	301.7	602.4	$2.34 \cdot 10^{-6}$	0.26	0.12
[0.6, 1.2]	[0.0, 0.3]	650.8	570.3	1221	$4.73 \cdot 10^{-6}$	1.15	0.23
	[0.3, 0.6]	1100	1099	2199	$8.53 \cdot 10^{-6}$	0.34	0.15
	[0.6, 0.9]	153.0	148.5	302	$1.17 \cdot 10^{-6}$	0.11	0.15
[1.2, 1.8]	[0.0, 0.3]	63.5	62.8	126.2	$4.90 \cdot 10^{-7}$	0.48	0.25
	[0.3, 0.6]	87.6	60.8	148.3	$5.75 \cdot 10^{-7}$	0.21	0.22
	[0.6, 0.9]	17.0	10.7	27.7	$1.08 \cdot 10^{-7}$	0.12	0.37

Even though the PYTHIA cross section was normalized to the observed $\Sigma^{\star+}$ yield an overestimation of PYTHIA for P_{T,Λ^0} under 0.3 GeV can be seen in the table (i.e. in total for $P_{T,\Lambda^0} < 0.3$ GeV $N_{PYTHIA}/N_{DATA} = 1.75$). In the region where the relative contribution of the PGF process increases the PYTHIA estimate falls below the data, thereby enabling other possible processes not generated in PYTHIA to account for the remaining strength. This is especially true for P_{T,Λ^0} between 0.6 GeV and 0.9 GeV. However, the AROMA yield does not completely fill the room left over by PYTHIA. This could mean that the charm quark mass of 1.35 GeV used for the generation of PGF events should be lowered as this shifts the average transverse momentum of the generated Λ_c^+ baryons to larger values. In view of the S/B ratios listed in table 4.14, the positive double spin asymmetries in the middle and lower right panel of figure 4.15 could be due to the PGF process. However, the uncertainty associated with the normalization of the Monte Carlo codes prevents us from a precise estimate of the background contribution at high P_T.

Driven by the asymmetries in figure 4.15 for the total dataset, and the S/B ratios listed in table 4.14, a subdivision into two (P_{T,Λ^0},P_{T,Λ_c^+})-regions is made. Region I

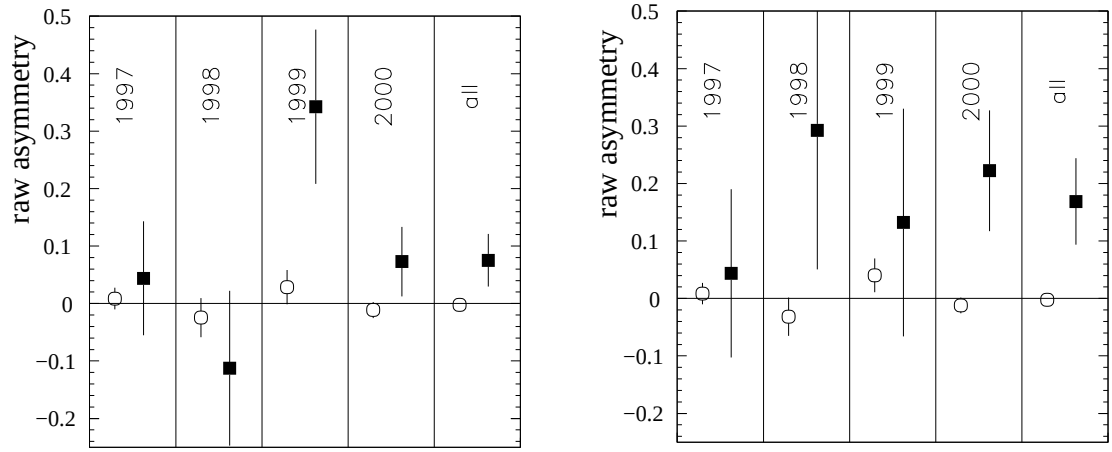

Figure 4.16: *Raw asymmetries for signal region (filled squares) and for the background region (open circles). For the left plot the events in panel 6, 8 and 9 were combined to represent the signal and the left-over panels for the background. In the right plot panel 6 and 9 were used for the signal and the other panels for the background.*

comprises the panel 6, 8 and 9 in figure 4.15 and Region II the other panels. In the left panel of figure 4.16 the results are shown. The filled squares correspond to region I and the open circles to region II. In region I a positive asymmetry of 0.08 ± 0.05 is found while the observed asymmetry of -0.003 ± 0.010 in region II is consistent with zero. For the right panel in the figure the minimal value for P_{T,Λ_c^+} has been increased to 1.2 GeV in order to set an additional hard scale. Comparison of the two panels in figure 4.16 shows that the requirement of a hard scale leads to a more pronounced raw asymmetry.

An estimate for the signal and background in the data is made using the S/B ratio listed in table 4.14. If we assume that the background process is not contributing to the asymmetry A can be connected to the gluon polarization $\Delta G/G$ according to

$$\frac{\Delta \mathrm{G}}{\mathrm{G}} = \frac{\mathrm{A}}{f_{\mathsf{PGF}}\ \hat{a}_{\mathsf{PGF}}\ \mathrm{D}\ P_{Target}\ P_{Beam}}. \tag{4.19}$$

The variables $\hat{a}_{\mathsf{PGF}}$, D, P_{Target} and P_{Beam} in the formula have been introduced before on pages 16 and 32 but were not quantified. The average value for the combined beam and target polarization is equal to 0.476 and $\langle \hat{a}_{\mathsf{PGF}} D \rangle = 0.67$ ($\langle \hat{a}_{\mathsf{PGF}} \rangle = 0.71$ and $\langle D \rangle = 0.95$) as determined from the Monte Carlo, where the same restrictions as in the data were used. The fractional contribution of the PGF process, f_{PGF} follows from the S/B ratios given in table 4.14 using:

$$f_{\mathsf{PGF}} = \frac{\mathrm{S/B}}{\mathrm{S/B} + 1}. \tag{4.20}$$

Table 4.17: *Raw asymmetries in the '97 -'00 data, and the $\Delta G/G$ values obtained from these asymmetries, for the (P_{T,Λ^0},P_{T,Λ_c^+}) regions where the S/B ratio (see table 4.14) is above one. For reference the f_{PGF} which were used are also shown.*

panel	P_{T,Λ_c^+}	P_{T,Λ^0}	f_{PGF}	A	$\Delta G/G$
6	$[1.2, 1.8]$	$[0.3, 0.6]$	0.54	0.18 ± 0.08	$1.05 \pm 0.46 \pm 0.46$
8	$[0.6, 1.2]$	$[0.6, 0.9]$	0.58	0.01 ± 0.06	$0.05 \pm 0.32 \pm 0.02$
9	$[1.2, 1.8]$	$[0.6, 0.9]$	0.75	0.23 ± 0.18	$0.96 \pm 0.75 \pm 0.42$

For each panel in figure 4.15 with an S/B ratio above one (table 4.14) $\Delta G/G$ is evaluated assuming that the observed asymmetry in the data is due to the PGF process. In table 4.17 the raw asymmetries obtained from the data (panel 6, 8 and 9) and the $\Delta G/G$ values determined from these are listed.

In the statistical uncertainty of $\Delta G/G$ only the contribution of the errors in the measured asymmetry is taken into account. The statistical errors associated with $\langle \hat{a}_{\mathsf{PGF}} \rangle$, $\langle D \rangle$, P_{Target} and P_{Beam} are much smaller and are thus not considered. The systematic uncertainty of $\Delta G/G$ is driven by the uncertainty in f_{PGF} wich is unknown and possibly very large. The quoted systematic uncertainty has been evaluated by assuming that the uncertainty in the Λ_c^+ yield, which drives the AROMA normalization is directly driving the uncertainty in f_{PGF}. From the statistical error for the Λ_c^+ cross section a relative systematic uncertainty of 44%[7] is obtained. In order to reduce this uncertainty the analysis needs to be continued with new data. Especially the observation of a Λ_c^+ peak with larger significance will be helpful.

The combined data of panel 6, 8 and 9 result in an asymmetry of 0.08 ± 0.05. Making use of $f_{\mathsf{PGF}} = 0.58$ evaluated from the normalized signal (S) and background (B) yields (given in table 4.14) a value for $\Delta G/G$ of

$$\frac{\Delta \mathrm{G}}{\mathrm{G}} = 0.43 \ \pm \ 0.27 \ _{stat} \ \pm \ 0.19 \ _{syst}. \tag{4.21}$$

at an average $\langle \mathrm{Q}^2 \rangle = 0.31$ GeV^2 is obtained. After requirement of an additional hard scale (i.e. $P_{T,\Lambda_c^+} > 1.2$ GeV), the data corresponding to panel 6 and 9 give $A = 0.17 \pm 0.08$. With $f_{\mathsf{PGF}} = 0.58$ the value of $\Delta G/G$ becomes

$$\frac{\Delta \mathrm{G}}{\mathrm{G}} = 0.92 \ \pm \ 0.38 \ _{stat} \ \pm \ 0.40 \ _{syst}. \tag{4.22}$$

[7] A consequence of a percentual error is a systematic uncertainty in $\Delta G/G$ that scales with the value of $\Delta G/G$.

The obtained positive value for $\Delta G/G$ with the inclusion of an additional hard scale is somewhat high but consistent with the value of $\Delta G/G$=$0.63^{+0.20}_{-0.19}$ at $Q^2 = 1$ GeV^2 [11] obtained from a fit to the world data on inclusive spin-dependent scattering using the Altarelli-Parisi equations. It is also consistent with the result of the HERMES high-p_T analysis [13], i.e. $\Delta G/G = 0.41 \pm 0.18$ (stat) $\pm$ 0.03 (syst) and the value for $\Delta G/G$ of 0.85 $\pm$ 0.17 $(stat)$ $\pm$ 0.16 $(syst)$ obtained in [52] on the basis of D^0 mesons and the value of 1.08 $\pm$ 0.76 $(stat)$ $\pm$ 0.81 $(syst)$ obtained in [6] from a Δq_f analysis.

Although the exact value of the model uncertainty on the obtained value of $\Delta G/G$ is hard to estimate, it is gratifying that all results obtained for $\Delta G/G$ are consistent despite large uncertainties for each individual determination. In fact the situation for the presently obtained value for $\Delta G/G$ is quite similar to the value obtained from the high-p_T pair analysis: a clear indication is found for a large positive gluon polarization, but the systematic uncertainty due to possible background contributions is hard to quantify.

4.6 Conclusions

In this chapter a search for Λ_c^+ photoproduction events in the HERMES 1997-2000 data is presented with the aim of determining the double spin asymmetry for the production process, which is possibly related to the gluon polarization $\Delta G/G$.

For the Λ_c^+ decay channel $\Lambda^0\pi^+$ 16 events were identified with a significance of 2. This number of events results in a Λ_c^+ electroproduction cross section of $(14 \pm 6\ _{stat} \pm 5\ _{syst})$ nb which can be transformed into a Λ_c^+ photoproduction cross section of $(538 \pm 231_{stat} \pm 188_{syst})$ nb. A comparison of the measured value of the Λ_c^+ photoproduction cross section with existing estimates of the total open charm photo-production cross sections at the same energy indicates that the present value is high. As the open charm cross sections are derived from D meson photoproduction cross sections, they depend on an assumed probability for a charmed quark to fragment into a D meson. Examples in the literature demonstrate that the existing Monte Carlo model for this fragmentation process does not always reproduce the data. Therefore, the total open charm photoproduction cross sections might have been underestimated - at least at threshold. Furthermore, a threshold enhancement for the production of Λ_c^+ and Σ_c particles might result in a larger cross section than anticipated from the D meson measurements alone.

The Ξ and $\Sigma^\star$ hyperons which decay into a Λ and π were identified as well in the analysis. Comparison of the yield with that expected from the PYTHIA Monte

Carlo shows that this simulation sometimes grossly overestimates the data. Double spin asymmetries for the Ξ and $\Sigma^\star$ hyperons are mostly zero, except in the case of the $\overline{\Sigma}^{\star+}$ hyperon where a positive asymmetry of 0.44 ± 0.19 is found. This value with an zero asymmetry for the $\overline{\Sigma}^{\star-}$ hyperon possibly imply that $\Delta\bar{u} - \Delta\bar{d} < 0$ for small x values under the assumption that the quark on which the scattering took place is the one most abundant in the observed hyperon.

Non-zero asymmetries for partially reconstructed Λ_c^+ baryons are found if the transverse momenta P_{T,Λ^0} and P_{T,Λ_c^+} are taken sufficiently high. These results were found to be stable in different data taking years. The AROMA and PYTHIA Monte Carlo simulations confirm that the sensitivity to PGF increases in the region of (P_{T,Λ^0},P_{T,Λ_c^+})-space where an asymmetry is observed. The asymmetry can be associated with PGF if the AROMA Monte Carlo is normalized to the observed Λ_c^+ cross section obtained in this work and the PYTHIA background Monte Carlo is normalized using the observed $\Sigma^{\star+}$ yield.

After proper normalization of the AROMA Monte Carlo yield a value for $\Delta G/G$ of $0.92 \pm 0.38_{\,stat} \pm 0.40_{\,syst}$ is found. This value is consistent with the value found in the HERMES high-p_T analysis [13] and also comparable to the value of $\Delta G/G$ of $0.85 \pm 0.17\,(stat) \pm 0.16\,(syst)$ determined from the asymmetry from D mesons [52]. Despite remaining model uncertainties, which are hard to estimate, in each of these determinations of $\Delta G/G$, it is striking that all the values are consistent. As the associated uncertainties are entirely independent, the obtained results reinforce each other. In fact the available analyses provide strong support for a positive gluon polarization at high x_g.

Chapter 5

The Lambda Wheels

5.1 Introduction

In 1997 a new silicon-detector system, comprised of a wheel-shaped array of silicon detectors directly down-stream of the target (Lambda Wheels) and a flat array of silicon detectors below the target (Recoil Detector), was proposed for the HERMES front region [71]. In order to demonstrate the feasibility of operating a silicon detector in the harsh environment of an electron scattering target, a Silicon Test Counter (STC) has been developed in 1998. The STC was placed near the target cell and has been successfully used to detect spectator products in deep-inelastic scattering [72]. Subsequently, the Lambda Wheels were developed, leading to the installation of a prototype Lambda Wheel module in 2000. In this chapter the design of the Lambda Wheels is motivated and explained, and first operational results obtained with the prototype module are presented.

After the HERA shut down of 2001 the full Lambda Wheel was installed and commissioned in 2002. The Lambda Wheels represent the first silicon detector which is completely incorporated in the HERMES detector system. Recently, the design of the Recoil Detector has been extended [73], resulting in a larger acceptance and profiting from the experience obtained from the development and operation of the STC and Lambda Wheels. It is noted that also the physics case for the HERMES recoil detector has shifted from spectator tagging to the observation of recoil products of exclusive reactions such as Deeply Virtual Compton Scattering.

The design of the Lambda Wheels has been motivated by the desire to enlarge the angular acceptance of HERMES in order to improve the prospects for hyperon and charm physics. As shown in Ref. [71] the Lambda Wheels increase the acceptance for Λ and J/Ψ production by about a factor 4 (if the so called short tracks which have no

PID are also considered the increase is a factor 2). Moreover, the introduction of the (azimuthally symmetric) Lambda Wheels leads to a large reduction of the false asymmetry present in the measurement of the Λ^0 polarization, and gives access to the target fragmentation region ($x_F < 0$), which is otherwise not accessible at HERMES.

For charm physics the increased detection probability of the Λ_c^+ baryon ($\Lambda_c^+ \rightarrow \Lambda^0\pi^+X$), and the J/$\Psi$ vector meson (J/$\Psi \rightarrow e^-e^+$) is important as the charm photoproduction cross section is very small. Detection of the Λ_c^+ particle provides a means to study charm production at threshold and possibly gives access to the gluon polarization. The observation of J/Ψ production enables the study of its production mechanism through the decay angular distributions [16].

The self-analyzing (parity violating) decay of the Λ^0 hyperon makes it possible to determine the polarization of the Λ^0 from the relative orientation of its decay products. For this reason the Λ^0 hyperon can be used to carry out polarization (transfer) measurements. For instance, the polarization transfer from the u-quark to the Λ^0 hyperon can be measured in the current fragmentation region. If the polarization of the Λ^0 hyperon originates partly from the polarization of the u or d quark in the Λ^0 , a non-zero polarization transfer is expected. Such measurements have been done at HERMES using both the '96-'97 data [30] and the '99-'00 data [74]. The collected statistics is, however, not enough to demonstrate convincingly that $\Delta u \neq 0$ as predicted by the model of Burkardt and Jaffe [29]. In this model the u-quark polarization was calculated to be -0.2 in the polarized Λ^0 hyperon.

In the target fragmentation region the longitudinal Λ^0 polarization is predicted to be sensitive to the relative orientation of the u and s quarks in the nucleon. According to Ref. [3], the spin of the s-quark is predicted to be anti-parallel to that of the u-quark, and -more importantly- this can be measured from the polarization of Λ^0 hyperons if they are produced in sufficiently large quantities in the target fragmentation region. No such data exist to date.

At HERMES, however, a large false asymmetry (≈ 35 %) is present in the Λ^0 polarization measurements as a substantial part of the low momentum pions from Λ^0 decay are not detected. Depending on the direction in which one wants to measure the Λ^0 polarization corrections are possible. For a longitudinal polarization measurement the false asymmetry can be partially corrected using a Monte Carlo program to calculate the false asymmetry, or using a helicity balanced data set. It can be shown (Ref. [75]) that in a helicity balanced dataset, i.e. a dataset that consists of parts with equal luminosity for both beam helicities, no false helicity is present provided that no changes in the detector took place during data taking. For transverse polarization measurements the false asymmetry becomes very small due to the up-down symmetry of HERMES and

can be neglected provided this up-down symmetry holds.

The Lambda Wheels give an enlarged angular acceptance for Λ^0 hyperon production. Moreover, the false asymmetry for Λ^0 polarization measurements at the HERMES spectrometer is reduced to the few percent level, which is important as the longitudinal Λ^0 polarization is known to be close to zero. Measurements with the Lambda Wheels will increase the statistics by a factor two, and at the same time the systematic uncertainty in the Λ^0 polarization measurement will be reduced by comparing results obtained with the helicity balanced data sets and those obtained with the Lambda Wheels (for which all statistics can be used). At the same time an increased angular acceptance enables sampling of Λ^0 hyperons further into the target fragmentation region, thus enabling first measurements of the relative orientation of u and s quarks [3].

The latter subject is of particular interest now that the most recent flavor decomposition of the nucleon spin has given hints for a positive s-quark polarization [6], while an SU(3)-based analysis of inclusive spin-dependent DIS indicated a negative s-quark polarization.

The HERMES beam energy lies in the threshold regime for charm production. Therefore, the charm cross section is small and any improvement in the probability to detect charmed particles is welcome. The Lambda Wheels will actually improve the detection of charmed particles like the J/Ψ meson and the Λ_c^+ baryon in two ways. On the one hand, the Lambda Wheels will increase the acceptance for the detection of charmed hadrons. On the other hand the signal to background ratio for Λ_c^+ and J/Ψ production is improved due to the wider acceptance. The relatively large mass difference between these charmed particles and their decay products results in on average higher transverse momenta. As a result the decay products tend to have larger transverse momenta with respect to their parent than normal DIS final state particles. This event characteristic is amplified if the event is produced via the PGF process which is believed to be one of the primary processes for charm production. Hence, the Lambda Wheels do not only increases the detection probability for Λ_c^+ and J/Ψ particles but also improve the chance to separate these particles from the background.

Thus, on physics grounds, there is a strong case to install a new detector in the HERMES front region that enables the detection of tracks leaving the primary interaction point under wide angles. The very restricted space in the HERMES front region made the pumping cross, which is connected to the vacuum chamber surrounding the target cell, the best location for the placement of the new detector. Unfortunately, this restricts the maximum distance between the detector and the target. Monte Carlo simulations show that detector planes (that give position information), with an outer

diameter of about 33 cm, positioned at 45 and 50 cm downstream of the target makes it possible to reconstruct $75 - 80$ % of the Λ^0 hyperons and thus lead to a factor 2 increase of the hyperon yield, a reduction of the false asymmetry to a few percent and an opening up of the target fragmentation domain as was all mentioned above. Placement in the pumping cross does, however, have a strong impact on the mechanical design of the Lambda Wheels.

This chapter is organized as follows. In section 5.2 the considerations that led to the basic design of the new detector are presented. Next a description of the overall mechanical system is given. The silicon specifications and the electronics needed for the detector are described in sections 5.4 and 5.5, respectively. Some of the results obtained with a prototype module of the Lambda Wheels are given in section 5.6 and, finally, conclusions are drawn in the last section.

5.2 Design considerations

The positioning of the Lambda Wheels in the pumping cross complicates the design appreciably. For instance, the inner diameter of about 34 cm leaves little room for the read-out electronics. The most important requirements to be fulfilled in the design are listed below. Subsequently, the impact of some of these requirements on the design are described resulting in the conceptual design of the detector.

1. In the middle of the target cell, through which the HERA lepton beam passes, (polarized) atoms are injected. These atoms travel to the open ends of the target cell, where they are pumped away in order not to destroy the beam vacuum. For this purpose holes have been made in the so-called target extension pieces, tapered pipes with an elliptical cross section inside the vacuum vessel, connecting the target cell to the actual downstream beam pipe. To keep the beam vacuum at an acceptable level the allowed contribution to the pressure near the target was set at 10^{-7} mbar by the HERA vacuum group. Thus, new materials brought into the vacuum chamber are required to have a low out-gassing rate, and should have little or no effect on the pump capacity.

2. Part of the electromagnetic field can escape into the vacuum chamber through the openings of the target extension piece. This field gives an additional noise contribution to the electronic signals in the Lambda Wheels and might even result in a detector which is unable to function properly if the control signals are distorted too much. For this reason the sensitivity of the detector to this RF field

should be low and the residual field at the location of the Lambda Wheel read-out electronics should be reduced to acceptable levels.

3. The amount of extra material in front of the existing tracking chambers should be as small as possible.

4. The accessibility to the pumping cross is very limited. Under normal circumstances it is only possible to enter the pumping cross through two C250 flanges, on the right and left (top) sides of the vacuum chamber. The system needs to be designed such that maintenance can occur through these flanges.

5. Due to the absence of cooling by convection, heat produced in the detector will result in high temperatures. In order to avoid high temperatures of the detector and the read-out electronics forced cooling is necessary.

6. The angular resolution of the detector should be comparable to that of the existing HERMES front tracking system. Together with the small lever arm in the detector this determines the required position resolution of the detector.

The first requirement points to silicon as the best candidate for the sensitive detector material, provided a detector open to the beam vacuum is chosen. Other detector materials have appreciable out-gassing rates and should therefore be separated from the beam vacuum. The extra material needed for such a separation would partially cover the existing HERMES acceptance which is in conflict with the third requirement. Furthermore, an open design is almost unavoidable as the pumping cross needs to be in open connection to the target chamber in order to enable the removal of the target atoms by means of the pumps connected to the pumping cross. For a reduction of the RF field strength (requirement 2) to acceptable levels an RF-shield with small radiation length and a small impact on the pumping capacity should be installed in between the part of the beam-line containing the target extension piece with holes in it, and the vacuum chamber containing the detector. Maintenance of any detector situated inside the pumping cross through the C250 vacuum flanges is hard. It is therefore advisable that the detector can be taken out, piecewise, through one of the vacuum flanges (requirement 4). Consequently, the detector should consist of a series of relatively small sized modules, which is also needed if silicon is used as detector material as the silicon detector is limited in size due to the maximum diameter of 6" available from any manufacturer. For ease of maintenance the cooling system (requirement 5) should be mounted on the second C250 flange. The 6^{th} requirement will be discussed in sect. 5.4.

5.3 Detector mechanics

The design requirements listed in the previous section resulted in a silicon detector consisting of 12 identical modules which are mounted on a maintenance free wheel-shaped frame which is completely outside the HERMES standard acceptance. The design has been described in [76, 77, 78]. The frame also carries part of the cooling system and it holds the cabling. Outside the vacuum a cooling tower removes the heat from the coolant. Each of the 12 modules contains two pieces of silicon and the corresponding front-end electronics. In front of the Lambda Wheels a metal grid is placed which acts as RF-shield. A computer aided drawing of the detector mechanics holding one silicon module is shown in figure 5.1. In the next four subsections the detector frame, a silicon module, the RF-shield and the cooling system are discussed separately in more detail.

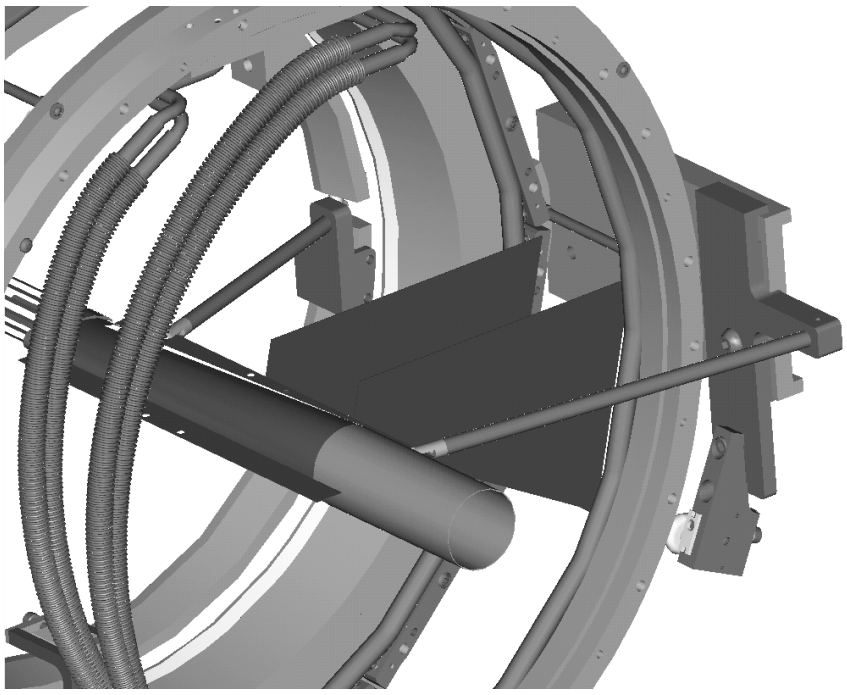

Figure 5.1: *Computer aided drawing of the frame of the* Lambda Wheels *with one module installed for ease of reference. The lepton beam enters the tapered wake field suppressor from the left.*

5.3.1 Detector frame

The frame is made of two stainless steel rings connected to each other with stainless steel frame spacers. It can rotate as both rings rest on three PEEK[1] wheels enabling the one-by-one installation of each module by rotating the wheel such that the desired position is located in front of the C250 flanges. The mechanical structure on which the rolls are mounted is fixed to the vacuum vessel with braces. The same structure is also used to mount the wakefield suppressor. A locking system fixes the frame after rotation during the installation of modules.

A reproducible alignment of the modules is provided by dowel pins on the interface where the modules are joined to the frame. The analog and digital circuitry on each module is electrically connected to the cabling in the frame with two 18 pin LEMO plugs. The plugs are made from PEEK, which was verified to be Ultra-High Vacuum (UHV) compatible [79]. The frame is made out of two parts. On each half a cable tree made from Kapton wire (UHV compatible) connects the 12 LEMO plugs to a PEEK 132 pin connector from where a Kapton coated UHV compatible cable takes the signals to several D50 connectors mounted on the aforementioned C250 flange.

The heat generated in the module is removed with alcohol that flows through a tube soldered to Oxygen Free High Conductivity (OFHC) copper bars using silver solder. These bars are mounted to the inside of the frame. Both the module and the bar have a flat surface and are pressed together with bolts to provide for a good thermal contact. Stainless steel bellows transport the alcohol to the cooling tower where it is cooled and circulated by a pump (see sect. 5.3.4).

5.3.2 Module

Each module contains two double sided silicon detectors and the local front-end read-out electronics for these two detectors (see figure 5.2). The pieces of silicon are separated 5 cm from each other and are glued to Al braces. Per module two carrier boards contain the read-out electronics, one for each silicon detector. The carrier boards consist of a multi-layer Kapton-Copper (OFHC) structure, which was extensively tested to verify its UHV compatibility [79]. To both sides of a 2 mm OFHC plate 2 layers of Kapton, with electronic circuits on it, are glued using epoxy. The electronics for each silicon detector is placed on one carrier board. Each side of the carrier board contains 4 HELIX chips and its drivers to read out one side of the corresponding silicon detector. A Kapton foil connects the input channels of the HELIX chip with the Al strips on the

[1]PEEK is an abbreviation of polyether-etherketone, an Ultra-High Vacuum compatible synthetic material.

silicon. The outer channels on each chip are not connected enabling a study of the noise in the read-out electronics. The bonds between the foil and the HELIX chips as well as the silicon are made from 17 μm Al wire. The two carrier boards are connected to the OFHC copper bars to form a rigid structure, well connected to the frame. On top of the module a stainless steel protection plate is mounted to protect the electronics. This is especially important for the bond wires which are very fragile.

Figure 5.2: *Computer aided drawing of a* Lambda Wheels *silicon detector module.*

5.3.3 RF shield

The passage of the high energy electron/positron beam through the HERMES experiment induces radio frequencies (RF) up to 30 GHz that leak into the vacuum containing the Lambda Wheels through the holes necessary to pump away the target atoms. An attenuation of the RF field strength is necessary for a proper functioning of the HELIX chips. Especially the distortion of the control signals would make it impossible to operate the chips at nominal beam currents. Furthermore, it is desirable to reduce

the field strength near the Lambda Wheels as it will decrease the noise in the silicon strips which will end up in the measured signal.

For these reasons, an RF shield is placed in between the vacuum vessel containing the Lambda Wheels and the internal target area. The RF shield is made from custom made 75 μm Cu foil which has 2 mm diameter holes in it on a 2.1 mm pitch. The 82% transparent foil is placed in front of the Lambda Wheels. A ring clamps the foil to the inside of the vacuum vessel with an Indium ring providing for a good electrical contact.

The noise present in the HELIX output signals increased from 5 mV (measured without beam) to 7 mV RMS for a 30 mA positron beam in HERA with the RF shield present. It was not possible to measure the noise contribution without RF shield as the HELIX chips could not be operated in that case.

5.3.4 Cooling system

A cooling system that controls the temperature of the Lambda Wheels is included for several reasons. First, the Lambda Wheels are situated in the vacuum and its cooling can thus only be accomplished using forced cooling. The heat load due to the HELIX chips is about 0.4 W per chip corresponding to about 6 W per module. Not removing this heat would result in too high temperatures and may destroy the chips and other front-end electronics. Secondly, a low temperature of the silicon is advantageous as the effects of radiation damage and leakage currents are reduced by lowering the temperature [80]. Also possible damage caused by the diffusion of hydrogen into the silicon is reduced if the temperature is low.

The reduction of the radiation damage comes from the lower diffusion speed at lower temperatures. The interaction of radiation with silicon may lead to a silicon atom knocked from its lattice position, with a vacancy and an interstitial defect as result. Combination of defects can lead to temporary traps in the crystal. A low diffusion rate will make it less probable that defects of this kind combine. As the Lambda Wheels are placed near the target cell in which atomic hydrogen or deuterium is injected, recombined molecular hydrogen is always present near the Lambda Wheels. A reduced diffusion of hydrogen diminishes its impact on the silicon lattice structure. The leakage current determines a large fraction of the noise present at the inputs of the HELIX chips. Lowering the temperature of the silicon gives a reduction of the leakage current. It has been measured that the leakage current halves approximately every 8 °C of temperature drop. For all those reasons it was decided to operate the Lambda Wheels at temperatures between -5 °C and -10 °C.

The cooling system for the Lambda Wheels consists of a closed loop of ultra pure

alcohol which is cooled outside the beam vacuum in a secondary vacuum chamber situated in a cooling tower. The alcohol transports the heat produced by the HELIX chips to the cooling tower mounted on the pumping cross. In the cooling tower a pump regulates the alcohol flow and Peltier elements are used to deliver the heat of the alcohol to cooling water of about 18 °C. The pump speed is set to a constant value such that turbulent flow occurs. The voltage over the Peltier elements is used to control the cooling power. It is regulated by monitoring the temperatures measured on the modules. Up to 100 W of heat can be removed from the detector at a minimum temperature of -35 °C.

A failure of the cooling system can have dramatic consequences for the Lambda Wheels. Therefore, the functioning of the cooling system is checked by means of an independent electronic control system. If a problem is signaled the power to the read out electronics and the bias voltage of the silicon is switched off. This will also happen, for instance, if the temperature of the cooling water is above 18 °C.

5.4 Silicon detectors

5.4.1 Principle of operation

Charged particles which traverse a gas will ionize some atoms present in the gas. If an electric field is present, the ionized electrons and positive ions will move along the field lines, thereby increasing their kinetic energy. They may subsequently ionize other atoms and the resulting charged particles can do the same, etc. Altogether an avalanche will result which gives a measurable pulse on the conductors used to create the electric field.

In silicon, a traversing charged particle enables electrons to go from the valence band to the conduction band allowing the electrons to move freely. The hole left behind after the electron is displaced is analogous to the gas ions. Contrary to the gas, no avalanche will occur under influence of the electric field used but many more primary ionizations occur because of the higher density and lower ionization potential. As a result only a small but measurable charge can be collected at the electrodes, and precautions are needed to reduce the leakage current. If pure silicon is used for instance, the leakage currents are much larger than the signal current[2]. A reduction of the leakage current is possible after implantation of p+ implants in intrinsic silicon (in practice low doped n-type silicon is used) resulting in a pn-junction. A depletion zone in which no free carriers are present is created when a reverse bias voltage is applied, which means that the junction side, i.e. the one with the p+ implants, is given a negative potential with

[2]It is noted that the decrease of the purity due to radiation damage cannot be compensated for if pure silicon is used.

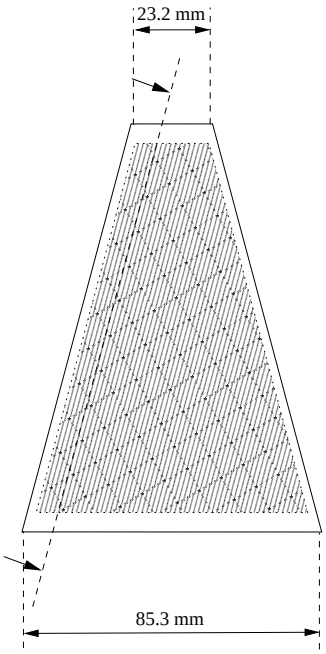

Figure 5.3: *Schematic drawing of a silicon plane. The arrows indicate where the silicon was cut through to arrive at figure 5.4.*

respect to the ohmic side, i.e. the one with the n+ implants. Electron-hole pairs created in this zone travel along the field lines in opposite directions and are collected at the implants (electrons at the ohmic side and holes at the junction side). In this way n-type silicon can be used for particle detection.

5.4.2 Silicon specifications

For the present application, silicon counters are cut out of a 6 inch n-type wafer of 300 μm thickness. It has a trapezoidal shape with an apex of 30°, a base of 85.3 mm and a top of 23.2 mm. As a consequence of this shape the length of the strips is not constant (see figure 5.3). The strips are read out at the base and are oriented parallel to the oblique sides. Every side has 516 strips of which 499 are coupled to the read out electronics. The 17 strips left over are too short to be connected. As a result 93% of the detector material is sensitive. A schematic view of the silicon counter is shown in figure 5.4, which represents an intersection along the middle of a strip at the junction side (see figure 5.3).

The reverse bias voltage is applied at the strip implants connected through 2 MΩ poly-silicon resistors. Each strip is AC-coupled to the read out electronics to avoid partial

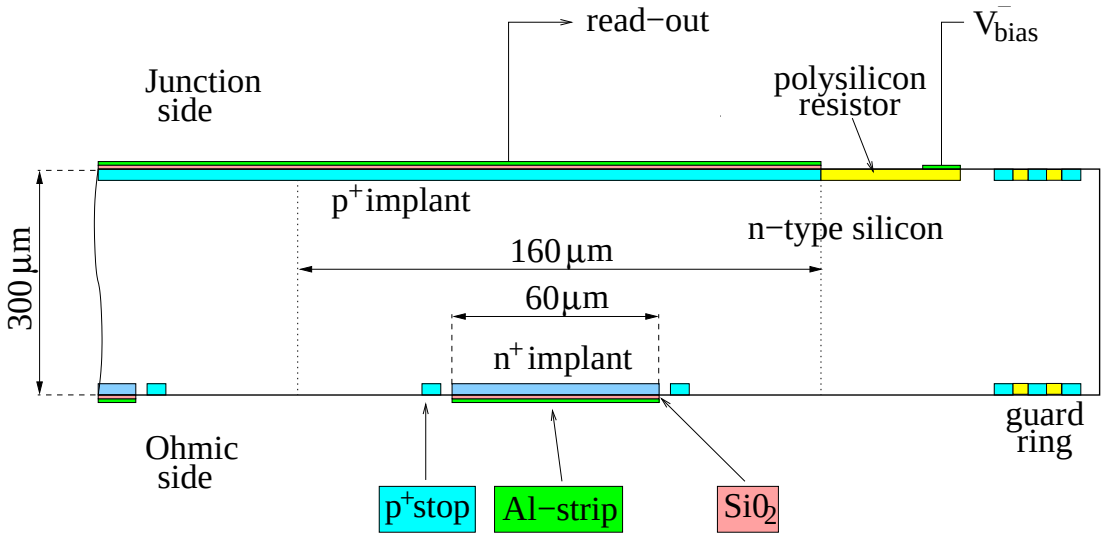

Figure 5.4: *Schematic drawing of the silicon detector which was cut through along the dashed line in figure 5.3.*

flowing of the leakage current through the read out electronics. This coupling is realized by putting a thin layer of SiO_2 used as dielectric material between the Al-strips, to which the read out is connected, and the implants giving rise to a capacitance of 75 pF/cm. Due to the high conductance of this layer the bias voltage is decoupled from the read out strips.

The strips have a width of 60 μm and a pitch of 160 μm. The pitch is determined by the required angular resolution (see sect. 6.2) and the required low occupancy, mainly set by Møller and Bhabha scattering. In Ref. [76] it is shown that these requirements lead to a maximum strip pitch of 444 μm. The strips on the n-side are isolated from each other by a ring of p+ implants (p-stops) around the strips. Three rings of p+ implants around all the strips isolate the strips from the edges of the silicon where the bulk of the leakage current flows. These rings are held at an intermediate voltage. In this way a stepwise drop from the bias voltage on the inside to ground potential on the outer ring is achieved. The detector is passivated with a 2 μm thick polyimide layer.

5.5 Electronics

The electronics used to operate the Lambda Wheels comprise the front-end electronics, electronics for the digitization and transfer of data to the HERMES Data Acquisition System (DAQ), and a slow control system for the control of the bias voltage and the control of the temperature of the Lambda Wheel modules. Each of these systems is

discussed in a separate subsection below.

5.5.1 Front end electronics

The local read out on the Lambda Wheels modules is performed with the 128 channel analog readout HELIX 128-2.2-chips [81]. One side of the silicon is connected to a daisy chain of four HELIX chips using a 50 μm Kapton foil. The HELIX chips are designed to be operated at the HERA bunch frequency of 10.4 MHz and thus sample the charge collected at the Al-strips of the silicon detectors every 96 ns. Each channel consists of a low noise charge sensitive pre-amplifier, a shaper which converts the transient present in the input signal into a voltage pulse proportional to the input charge and 141 capacitors (pipeline cells) which can store the pulse information corresponding to the charge collected at the strips. A maximum latency of 128 sampling intervals corresponding to 12.288 μs is possible. The chip is clocked with a signal derived from the HERA machine clock after giving it a delay to optimize the charge collection. Due to the smaller drift speed of the holes an extra delay is given to the chips connected to the junction side. When a trigger is given to the HELIX chip the pipeline cell in which the signal corresponding to this trigger is stored is tagged. At this moment the pipeline cell is not available anymore for the storage of new pulse information. Up to 8 triggers can be accepted without the tagged pipeline cells being read out, and the occurrence of trigger number 8 is signaled. When the DAQ is ready to receive the HELIX chip information, the signals of the 128 channels are multiplexed into a serial signal. A trailer containing the 8 bit address of the pipeline cell number is added. After the first HELIX chip is read out completely the next chip in the daisy chain is read out. This is continued until the fourth chip is read out. At that moment the pipeline cells which were read out are ready again to store new signals.

Before the HELIX output signal is taken from the carrier board to the outside connection the analog output current of a dummy channel is subtracted from the analog output signal and transformed into a differential current signal. Both steps reduce the presence of common noise. In the first step the common noise interference present on the HELIX chip is reduced, and in the second the common noise picked up during transmission is taken out.

The operational points of all amplifiers in the HELIX chip are controlled via registers. The settings of these registers can be set using a serial protocol. This makes it possible to tune the chip and to account for possible radiation damage in the chip. The content of these registers controls 7 current Digital to Analog Converters (*DAC*s) which provide the bias currents for the amplifiers, and 6 voltage *DAC*s that control the values of the feedback resistors of these amplifiers. One register is used to set the

latency for the pipeline cell to be tagged if a trigger occurs.

The controls of the local readout electronics of the Lambda Wheels (as described in this paragraph) are organized in one custom made electronic module, the *Hermes Lambda wheels Control Unit* (HLCU).

5.5.2 Analog to Digital Converter

The signals produced by one Lambda Wheel module are brought to one custom made ADC module, the *Hermes Analog Digital Converter* (HADC). All HADC modules are located close to the experimental set-up (< 5 m). Each HADC module samples four differential current outputs (one for each side of the two silicon counters) coming from four daisy chained HELIX chips per side. The complete readout of a module takes 52.224 μs. This time is the same for the readout of the complete Lambda Wheels system due to parallelisms in the read out. The HADC can handle up to four triggers. The HELIX output is capacitively coupled to the HADC input to decouple the bias voltage present on the carrier board (see sect. 5.5.1).

As a first step the analog signals are digitized with a 10-bit ADC. The pedestal subtraction and hot channel suppression (i.e. channels that always give a high ADC value) is accomplished through the subtraction of a bit pattern. This pattern is constructed and results in ADC values grouped around a positive baseline. In the next step the common mode noise present in the signals is reduced. The common mode signal is determined as the average value of the first 16 channels out of 32 channels that have their ADC value below a certain threshold. This threshold is set such that strips where a signal is present are not used for the common mode subtraction. After common mode subtraction a second threshold is applied and all strips with ADC values above this threshold are transferred to the central HERMES DAQ system.

5.5.3 Slow control

The operational voltage of the HELIX chips and other front-end electronics present at the carrier boards is called low voltage in contrast to the somewhat higher voltage used to bias the silicon counters. It has been decided to shift the average of the low supply voltages at -2 and +2 V to the bias voltage. This has been done for the following reason. Although the read out of the HELIX chip is decoupled from the bias voltage a break down of the insulating SiO_2 layer, due to a pinhole for instance, might occur. This would induce a current flow through the HELIX chip. Furthermore, the electric field near the strips with the pinhole is distorted, thus lowering the charge collecting efficiency. The above effects are minimized when the average supply voltage of the

HELIX chip is taken to be equal to the bias voltage.

The (high) bias voltage for complete depletion of the silicon is about 50 V. In due time the bias voltage most likely has to be increased to compensate for possible radiation damage. In the design a maximum bias voltage of 100 V is assumed, which is safe regarding possible breakdowns of the silicon. The bias voltage is controlled continuously. This makes it possible to turn it down (like for the low voltage) during the injection and energy increase operation of the HERA positron/electron beam. During injection the radiation level is much higher than during normal operation. If the bias voltage would be applied in these periods the corresponding currents would enhance possible radiation damage.

A second independent slow control system has been built to operate and monitor the cooling system. This system monitors a range of temperature sensors located throughout the Lambda Wheel system and stabilizes the temperature around a given set temperature.

5.6 Detector performance

In Ref. [82] some first operational experiences obtained with a prototype of the Lambda Wheels are described. Some of these results are presented here as well to show the performance of the new detector system.

In the year 2000 the entire Lambda Wheel infrastructure was installed at HERMES including one prototype silicon module. In this section (and in the following chapter) the results obtained with this single module are described.

In the left panel of figure 5.5 the measured (un-triggered) pulse height distribution of the prototype module is shown. The overlap between the signal and the steeply falling noise contribution for lower ADC values is apparent. From the figure it can be deduced that a threshold value of about 20 ADC channels is appropriate to significantly reduce the noise contribution, while hardly affecting the signal.

Due to the change in strip length over the silicon counter the capacitive load on the HELIX chips changes. The electronic noise charge increases with capacitance (and thus with strip length) while the gain of the HELIX chip decreases. As a result the Signal to Noise ratio changes with strip number as is illustrated in figure 5.5. The noise contribution is defined as the RMS value of the measured noise signal. Using a random trigger the noise contribution has been isolated from the signal due to particle hits. It

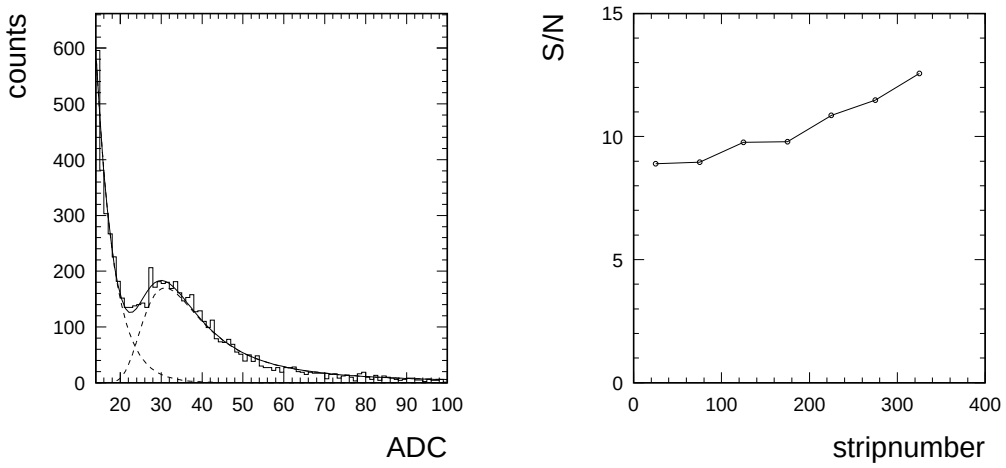

Figure 5.5: *On the left side a pulse height spectrum measured with a prototype module of the* Lambda Wheels *at* HERMES *is shown. Only the long strips from the ohmic side are used and no clustering has been performed. The solid line is a fit of a Landau distribution and an exponential shape to the data. On the right the Signal over Noise ratio measured for the* Lambda Wheels *is shown. Both figures are taken from Ref. [82].*

can be seen from the figure that the S/N ratio is about 10, which is adequate for a tracking detector.

In order to study the effect of the radiation damage on the silicon the leakage currents are frequently measured as a function of the applied voltage (while keeping the temperature constant). The results of such a studies can be found in Ref. [80]. It is concluded that increases of leakage currents are observed, and can be associated with excessive radiation. However, the total increases observed do not limit the practical life span of the Lambda Wheels.

The resolution and tracking efficiency have also been investigated. The results, which are described separately in chapter 6, are in agreement with the expectations.

5.7 Conclusions

A new wheel-shaped array of silicon detectors, known as the Lambda Wheels, has been developed for the HERMES experiment at DESY. The purpose of the system is to increase the acceptance of the HERMES spectrometer for slowly decaying particles such

as the Λ^0 hyperons, reduce the false asymmetries entering the determination of the Λ^0 polarization and giving access to the kinematic domain at $x_F < 0$.

The design considerations and chosen solutions have been presented in this chapter. It was found possible to install and operate a system consisting of 12 modules, each comprising two double-sided silicon counters **inside** the HERA lepton beam vacuum. Custom made front-end electronics, read-out boards and analogue-to-digital converters were built and shown to operate according to expectations.

Following the installation of the Lambda Wheel infrastructure at HERMES the performance of the system was investigated with one prototype module. All systems were found to operate satisfactorily, and a signal-to-noise ratio of about 10 was determined, which is sufficient for the foreseen applications.

In the next chapter the tracking of events which are (partially) recorded with the Lambda Wheels prototype module is discussed. From these studies it is shown that the efficiency and resolution of the system is according to expectations.

Chapter 6

External tracking

The studies described in this chapter are based on measurements performed with a prototype module of the Lambda Wheels which was installed in the HERMES experiment in the year 2000. The data taken with the prototype made it possible to study tracking of events passing the module and to determine its efficiency.

Thus far the analysis of data collected by the HERMES experiment is based on the existing Hermes Reconstruction Code [83] (HRC). The algorithm used by HRC is based on the orientation of the wires in the existing tracking chambers which is either vertical (measures the x direction) or tilted by plus or minus 30°(measures the u and v directions, respectively). The program HRC translates the decoded data from the experiment into partial tracks corresponding to the space points recorded before or after the spectrometer magnet; the code combines the front and back tracks in complete tracks representing a particle, determines the energy and momentum of this track and carries out particle identification. The most important task of HRC is, however, the tracking. For this it uses a tree-search algorithm based on pattern recognition by using look-up tables consisting of hit patterns for each plane orientation. After combination of the hits in planes of the same orientation a tree-line is reconstructed. In the next step the tree-lines for the different orientations are combined resulting in a partial track. The details can be found in Ref. [83].

The structure of the Lambda Wheels, its wider acceptance and different orientation of the strips, made it unnatural to incorporate in HRC the tracking of events passing the Lambda Wheels. Similar arguments apply to other additional detectors that were installed outside the standard HERMES acceptance in the framework of the HERMES Charm Upgrade program [84]. Coordinates in these additional detectors can only come from tracks reconstructed in either the Lambda Wheels and/or the DVCs. For this reason it was chosen to incorporate the Lambda Wheels tracking software and the software

produced for the other new tracking detectors in an eXtended Tracking Code (XTC). The program XTC runs after HRC such that it can use reconstructed HRC tracks.

The track reconstruction in the Lambda Wheels is relatively simple. First, a cluster algorithm combines information collected by adjacent strips, where after coordinates are formed in the silicon counters. From the coordinates in the silicon counters belonging to one module one or more tracks are constructed. A difficulty arises in the selection of the clusters that belong to a track as there is typically more than one cluster seen in each silicon counter. One cannot simply take all geometrically possible combinations and use these as physical tracks as most of these tracks will be ghost tracks due to e.g. clusters caused by noise fluctuations. Identification of the clusters connected to real particles traversing the detector is necessary. For instance, the correlation between clusters on either side of one piece of silicon can be used to reduce the number of possible track candidates. Further improvements are realized by making use of other detectors, and the assumption that good tracks are directed towards the target or originate from the vicinity of the beam line.

Due to the small overlap of the Lambda Wheel acceptance and the standard HERMES acceptance the Drift Vertex Chambers (DVC) which also feature a relatively wide acceptance, are used to improve the selection of clusters in the Lambda Wheels[1]. Two different cases were studied. In one case tracks reconstructed from the DVC hit information are intersected with the Lambda Wheels, while in the other case the Lambda Wheel tracks are intersected with the DVC wire planes. In section 6.1.3 the results of these two studies are presented. In both cases a positively identified track reduces the total multiplicity. Furthermore, tracks are selected based on the relative position of their vertex with respect to the beam. A quality parameter is introduced to define the goodness of the selected combination of clusters to give a track. It is emphasized that the additional information and/or criteria are only used to positively identify valid tracks, in order to reduce the multiplicity. The absence of data in the DVC is not used to remove a track combination, as this track may have been caused by a low momentum proton not reaching the DVC.

In this section the Lambda Wheel geometry is also described. For tracking purposes it is important to know that the prototype module has been placed in the upper right corner of the HERMES xy-plane when viewed in the propagation direction of the beam. The strips either make an angle of 30° or 60° with respect to the horizontal (or

[1]The DVCs have a somewhat larger acceptance than the rest of the HERMES spectrometer, and are incorporated in HRC because of their standard wire geometry. However, the Lambda Wheel acceptance is still considerably larger and - because of their position - serve different physics objectives.

HERMES x-axis).

The track resolution of the Lambda Wheels has also been studied using some assumptions for the cluster resolution. Its determination from the Lambda Wheel data is not straightforward as the corresponding tracks originating from the standard tracking detectors are of insufficient precision themselves. Nevertheless an estimate of the resolution has been made, which is presented in section 6.2.

Thirdly, in section 6.3 a method to determine the efficiency of the Lambda Wheel prototype module is described. This method is applied to the data, yielding a measured tracking efficiency for the module.

The major conclusions of our Lambda Wheel tracking studies are summarized in section 6.4.

6.1 Track reconstruction

If exactly one particle traversed the two silicon counters in the prototype module causing exactly one strip to fire with its pulse height above threshold in each plane, tracking is reduced to a simple geometrical problem. However, more strips could have collected part of the charge liberated by the particle, and have an ADC value above threshold. If these strips are adjacent, the pulse heights can be combined into a group of strips to give a cluster. Complications arise if one plane has more clusters above threshold coming, for instance, from other passing particles or noise. Furthermore, inefficiencies may cause the signal due to a particle not to be above threshold. Consequently, it is the selection of clusters that belong together which needs most attention when developing a tracking algorithm.

The tracking of particles passing through the Lambda Wheels is organized in such a way in XTC that each module is treated separately, whereafter a loop over all modules is performed. The first step in the tracking procedure is the clustering (section 6.1.1). Next, clusters on the two sides of the same silicon counter are combined to give coordinates. A threshold is applied to a specially defined Figure-Of-Merit (section 6.1.2), which is a measure of the probability that the clusters on the two sides originate from the same particle. Now, tracks are reconstructed. Tracks that have a vertex downstream of the module are considered false. In section 6.1.3 it is described how the DVC is used to reduce the multiplicity by investigating whether the track is shared between the Lambda Wheels and the DVC. Selection criteria are also applied on the distance to the beam line in front of the Lambda Wheel, and on the maximum polar angle of the

track (section 6.1.4). If a track is positively identified either due to a hit in the DVC or based on its distance to the target, it is used to discard other tracks that use the same clusters. In the last subsection the results of the event selection are presented.

6.1.1 Clustering

With clustering the combination of all adjacent strips with a pulse height above threshold is meant. Note that a single strip without neighbors is considered a cluster as well.

The charge liberated while a particle traverses the sensitive part of the silicon is collected on the strips nearest to the particle track. In general this results in the charge being collected on one strip per side, which is enough to give a signal above threshold. It is, however, possible that adjacent strips also have a signal above threshold. In that case it is assumed that these strips are part of a cluster that resulted from a single traversing particle. The signal of this cluster is taken to be equal to the sum of the pulse heights of the strips in the cluster. The position of the cluster is calculated from the positions of the adjacent strips weighted by their pulse heights. This gives a better position measure as compared to the case of a single strip. The clustering reduces the amount of false tracks that are reconstructed, and it gives a better value for the pulse height if a real particle passed the detector. As few strips are disconnected due to pinholes, which short the coupling capacitors, two strips that have an unconnected strip in between them are also treated as a cluster. A cluster can maximally consist of four adjacent strips. If more strips form a cluster this cluster is not considered in the reconstruction anymore.

6.1.2 Coordinate reconstruction

The summed pulse height recorded in one cluster is a measure of the charge liberated by a passing particle. The pulse heights are approximately distributed according to a Landau distribution. Therefore, hardly any correlation exists between the pulse heights of different events, or in different pieces of silicon for the same event. However, for the two sides of one piece of silicon a correlation is present as the same liberated charge is sampled. In figure 6.1 this correlation is seen as an increase in the number of pulse height pairs around ADC channel 40 for the pulse heights recorded from two sides of the same silicon counter. A Figure-of-Merit (FOM) [85] is introduced in an attempt to quantify this correlation and reduce the effect of outliers with a large pulse height and noise contributions. The FOM is defined as

$$FOM = 0.5(pls_1 + pls_2) \exp\left(-0.3/R_{\mathrm{pls}}\right) F_1 F_2 \tag{6.1}$$

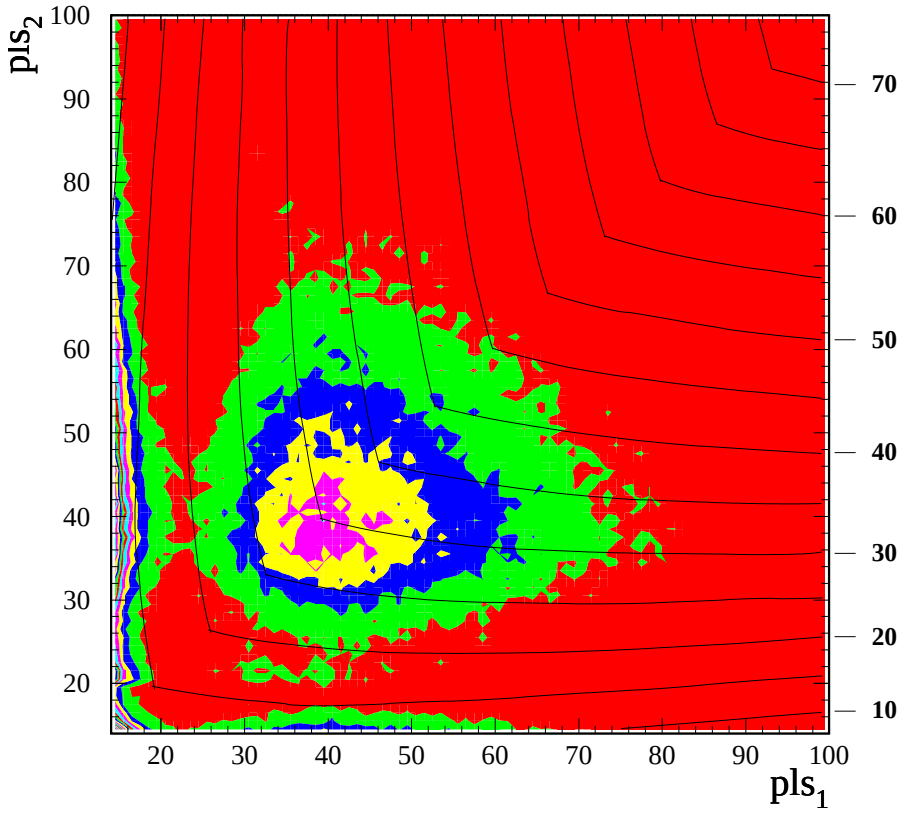

Figure 6.1: *Contour plot of the correlation between the pulse height spectra of two sides of one silicon counter. Lines of a constant Figure-of-Merit (see Eq. 6.1) are also shown in the figure. The value of the corresponding* FOM *are shown on the right-hand scale of the figure. The data represent events recorded with the* Lambda Wheel *prototype module.*

with pls_1 and pls_2 the pulse heights (above threshold) observed in the two sides, R_{pls} the smallest value of pls_1/pls_2 and pls_2/pls_1, and $F_i = \exp((250 - pls_i)/50)$ for pls_i above 250 and 1 for lower values. The factors F_i are needed to discard outliers. The lines of constant FOM showed in figure 6.1 demonstrate that a threshold applied on the FOM (as calculated with Eq. 6.1) can be used to suppress unwanted coordinate combinations. In practice we have chosen the following constraint: FOM > 20.

6.1.3 Track reconstruction

For part of the tracks which have been reconstructed from combinations of coordinates in the two silicon counters, it is possible to determine the probability that they correspond to a particle also observed with the DVC. In this subsection two different methods are presented that can be used to find such a matching track in DVC and Lambda Wheels. In the first case one starts from a DVC track, and in the other from a

Lambda Wheel track.

Selection of a LW strip

The Drift Vertex Chambers (DVC) can be used to assign clusters to a track as it overlaps partially with the larger Lambda Wheels acceptance. The DVC chamber consists of six planes, i.e. two sets of three planes with a x, u and v wire orientation. It is possible to reconstruct a track from the information provided by the DVC alone. The procedure to evaluate such a track has been incorporated in XTC. However, the angular resolution of these tracks is not good enough to use them for the identification of unique coordinates in the two silicon planes. The poor DVC resolution is a consequence of its positional plane resolution of about 200 μm and a lever arm of only about 8 cm. If projected onto the Lambda Wheels (at a distance of 70.9 cm for the first Lambda Wheel plane), this corresponds to a positional uncertainty of 2.5 mm which is significantly larger than the 160 μm spacing of the silicon strips. Therefore, reconstructed DVC tracks cannot be used for the selection of coordinates in the Lambda Wheels.

Selection of a DVC wire

Particle tracks reconstructed in the Lambda Wheels that also traverse the DVC should give signals in the DVC from which a coordinate can be reconstructed. As compared to the Lambda Wheels the DVC are larger. As a consequence fewer particles traverse the DVC per unit area and the positional resolution needed to select a coordinate in the DVC is smaller than is the case for the Lambda Wheels. Furthermore, the angular resolution of the Lambda Wheels is slightly better than that of the DVC. In contrast to the case in which DVC tracks were used as pointers, a comparison of the reconstructed DVC coordinate (in the middle of the DVC) and the position where a reconstructed Lambda Wheel track intersects the middle of the DVC is, therefore, possible.

A simplified approach to reduce the Lambda Wheel multiplicity using DVC information is offered by investigating how many wires in the DVC that gave a signal are close to the intersection of a reconstructed Lambda Wheel track. For this test no evaluation of a DVC coordinate is needed. Instead a quality factor based on the number of wires found along the reconstructed Lambda Wheel track is introduced. The criterion that has to be fulfilled in order to select the clusters used for tracks is that at least four wires within 0.6 cm of the Lambda Wheel track must have fired. Furthermore, each wire orientation should be present. Clusters which are positively identified according to the above requirements are not used in other combinations of Lambda Wheel clusters.

6.1.4 Geometric selection criteria

The ambiguities left after the DVC selection are small. It is, however, possible to achieve some extra filtering based on a geometrical selection. A Monte Carlo study showed that there is almost no contribution of Λ^0 decay pions with a polar angle above 0.5 rad. For this reason tracks with a polar angle above 0.5 rad are not taken into account. As a consequence tracks that have their vertex with the beam line behind the first Lambda Wheel plane are removed as well. Here it is assumed that the HERMES z-axis represents the lepton beam. A track is selected and used to deselect other tracks that use the same clusters if the distance of a track with this z-axis is smaller than 0.75 cm and the vertex falls in the target cell, i.e. -20 cm $< Z_{vert} < 20$ cm.

6.1.5 Observed multiplicities

The selection criteria introduced in the previous sub-sections reduce the number of tracks that are reconstructed. In table 6.1 this reduction is quantified. First, one should notice the difference between the ohmic and junction sides. The higher amount of strips that gave a signal above threshold on the ohmic side is mainly caused by a broken HELIX chip reading out one of the junction sides. Furthermore, the larger count rate of strips per event in the ohmic side must be partially attributed to the enhanced noise level on the ohmic side. Clustering reduces the number of possibilities to make a track per plane with a factor 3.6 and 1.4 for the junction and ohmic sides, respectively. The reduction for the ohmic side is less due to a larger presence of noise strips (with small cluster multiplicity), and a higher cluster multiplicity for particle induced clusters. After clustering the strips on each side of one counter, combining clusters of the two sides of one silicon counter gives the number of coordinate pairs per event. Here, a reduction in possibilities occurs as some of the clusters do not give a coordinate in the sensitive silicon. After application of a threshold on the FOM (see paragraph 6.1.2), the number of coordinates to be considered in the track reconstruction is reduced by a factor 2.5. In a final step the good coordinate pairs in the two silicon counters of one module are combined. On average 5.3 tracks can be reconstructed per event for the prototype module. The DVC selection criteria reduce the track multiplicity per event by a factor 4.4. The geometric selection criteria give a small improvement. The final track multiplicity of only 1.2 tracks per event per module is a very promising figure, as no physics requirements were used. If the track multiplicity had been higher this could have resulted in more ambiguities and background in the physics analysis.

Table 6.1: *Strip and cluster multiplicities in the junction and ohmic side of a silicon counter, coordinate multiplicities in a counter after combination of clusters and track multiplicities after combination of good coordinate pairs.*

Multiplicity		junction side	ohmic side
1 side of 1 counter	strips/event	4.3	7.3
	strips/cluster	1.8	1.9
	clusters/event	1.2	5.1
2 counters	coordinate pairs/event	5.5	
	good coordinate pairs/event	2.2	
1 module	tracks/event	5.3	
	good tracks/event	1.2	

6.2 Angular resolution

Based on the number of strips present in a cluster an upper limit can be given for the resolution that can be achieved in the position measurement perpendicular to the strips. If there is one strip in a cluster, with pitch p, the resolution is easily evaluated according to $\sigma = \sqrt{\int_{-p/2}^{+p/2} x^2 dx / \int_{-p/2}^{+p/2} dx} = p/\sqrt{12}$ for the resolution. If a cluster consists of two strips a resolution improvement of 17% can be obtained if the middle between two strips is taken as an estimate for the coordinate where the particle passed through the silicon. If also the pulse height information is used for the estimate of the coordinate an even better resolution can be obtained. For a realistic evaluation of the resolution in which the pulse height information is also used the noise signal should be taken into account. This has not been carried out in the present analysis, but it is believed that the enhancement of 17% given above is a good estimate. When the evaluation is done for three or four strips a resolution improvement of 27.3% or 28.5% (with respect to $1/\sqrt{12}$) is achieved.

In the rest of this section it is assumed that a cluster always consists of one strip. This is a conservative choice as a larger cluster size will lead to a better resolution as was argued above.

The orientation of the modules of the Lambda Wheels in the x and y-direction is different for the various modules. Due to the symmetry present in the location of the modules in the ring shaped frame only the modules in one quadrant need to be considered. As a first step the coordinate resolutions in the x and y-direction (σ_x and σ_y

respectively) for modules with three different orientations are evaluated. From these coordinate resolutions, the angular resolution of the tracks is determined.

Consider the intersection of two strips on both sides of a piece of silicon that gave a signal[2]. The two strips must have fired due to a hit in the diamond shaped area around the intersection point. These diamonds are shown in figure 6.2 for three different orientations of the module. As we are interested in the resolution in the x and y direction the three diamonds are projected on both axes. Now the coordinate resolutions are obtained from

$$\sigma_x = \left[\frac{\int_0^{x_{max}} x^2 L(x)dx}{\int_0^{x_{max}} L(x)dx}\right]^{-\frac{1}{2}}, \text{and } \sigma_y = \left[\frac{\int_0^{y_{max}} y^2 L(y)dy}{\int_0^{y_{max}} L(y)dy}\right]^{-\frac{1}{2}}, \tag{6.2}$$

where $L(x)$ and $L(y)$ describe the relative weight of the corresponding part of the diamond at that x and y value. The calculation of σ_y is similar and follows from σ_x on the basis of symmetry arguments, i.e. σ_y of module I is equal to σ_x of module III. The resulting resolutions are listed in table 6.2 for the three different module orientations. The resolutions of all the other modules follow from those in the table.

Table 6.2: *Resolution in the x and y direction for modules orientated like those shown in figure 6.2 under the assumption that a cluster contains one strip. For two strips per cluster the numbers have to be multiplied by 0.826.*

Module Orientation	Resolution μm	
	x-direction	y-direction
I	46	122
II	92	92
III	122	46

Under the assumption that the coordinate resolutions have Gaussian distributions the angular track resolution for the different modules can be inferred from the coordinate resolutions. The resolution in the position difference in the x direction is given by $\sigma_{\Delta x} = \sigma_x\sqrt{2}$. In order to calculate the angular resolution the separation between the two pieces of silicon is (50 mm) needed. The resolution depends on the angle of incidence of a particle. In the case of perpendicular incidence an angular resolution for module II of 2.6 mrad in both projections is obtained. Taking into account that the

[2]The thickness of the silicon is neglected.

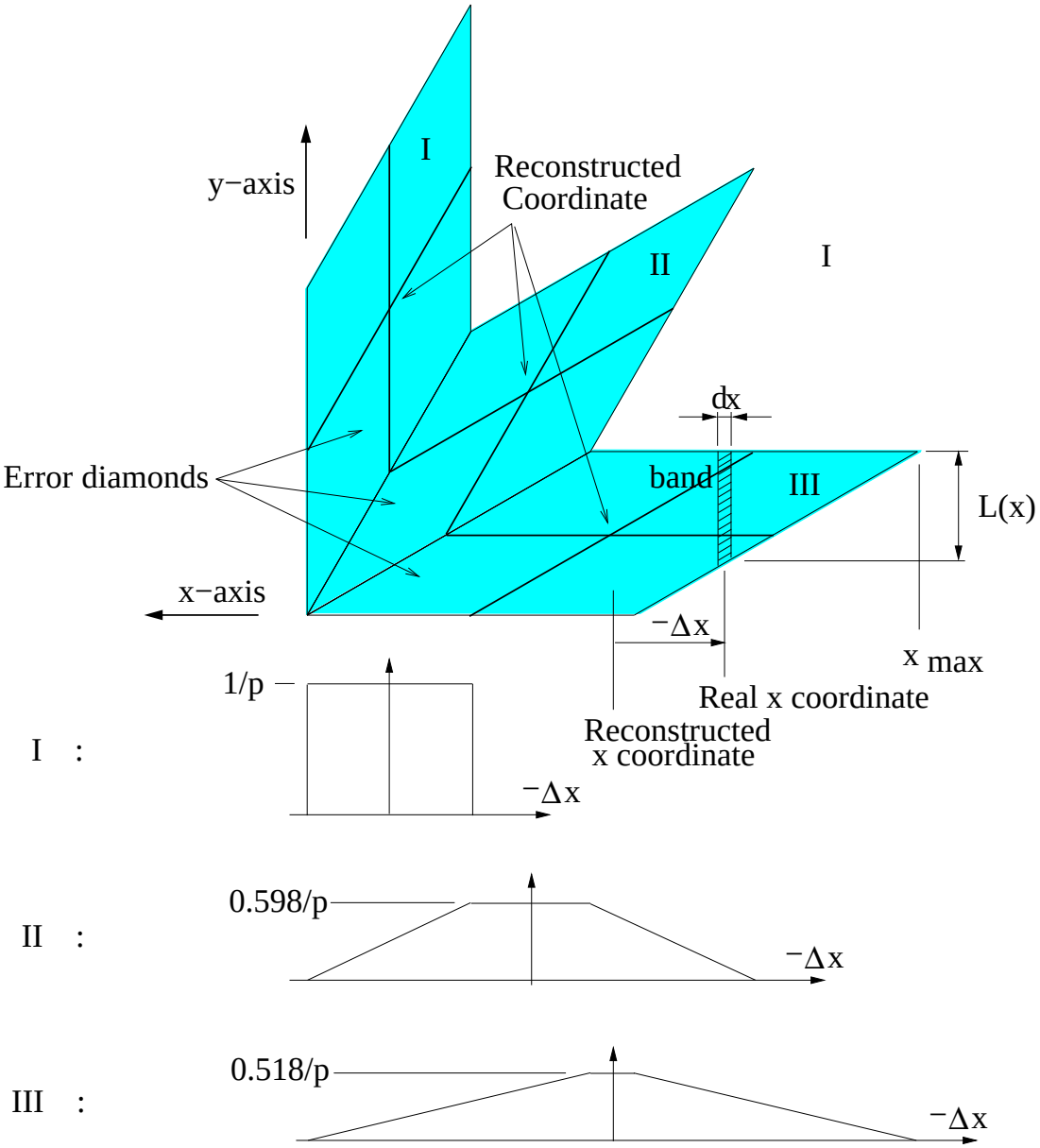

Figure 6.2: *Error diamonds for three different positions of the module (denoted with I, II and III) in the support structure. Under the three diamonds the projections of the x-axis used for the determination of the resolution in the x-direction are shown. The maximum heights of the distributions are a consequence of the normalization of these distributions to unit area.*

strip multiplicity is close to 2 an improvement of a factor 0.826 can be achieved. Therefore, the angular resolution for tracks that only use Lambda Wheel information becomes 2.1 mrad. This number is indeed of similar size as the resolution of the HERMES front region, which amounts to about 0.6 mrad at best (see section 5.2).

6.3 Module efficiency

There are a number of reasons why not all particles produced in the primary interaction are reconstructed in the HERMES spectrometer. One of them, its relatively small angular acceptance is partly accounted for through the addition of the Lambda Wheels. Another one is the inefficiency of the tracking devices which is made up from the single-plane inefficiencies.

In this section the (in)efficiency of the prototype silicon module of the Lambda Wheels is evaluated. For the Lambda Wheels the single-plane efficiency is especially important as there are no redundant planes, i.e. if one plane does not give a signal the particle cannot be reconstructed. Even though silicon detectors have efficiencies close to one hundred percent the absence of redundant hit information for the Lambda Wheels could degrade the total tracking efficiency significantly. For instance, a single-plane efficiency of 95% gives a total tracking efficiency of only 81.5% ($=0.95^4$).

To determine the single-plane efficiency the number of particles going through the sensitive silicon and the number of clusters that fired due to these particles need to be measured for a large number of events. Tracks reconstructed by HRC, i.e. particles observed in the standard HERMES acceptance, are used to estimate the number of particles that went through the silicon counters.

Physics analyses mainly rely on the angular information contained in the HRC tracks. The positional information is mainly used to determine if the track came from the target. For the efficiency determination, we also need to determine the position of the HRC tracks to decide whether a particle went through the silicon, i.e. the hit coordinate needs to be determined. However, due to the resolution of the HRC tracks and multiple scattering the hit coordinates are smeared. The method used to determine the efficiency should account for the smearing of the hit coordinates as estimated from the HRC tracks. This is discussed in section 6.3.1. The actual efficiency determination including a correction for unconnected or dead strips is presented in section 6.3.2.

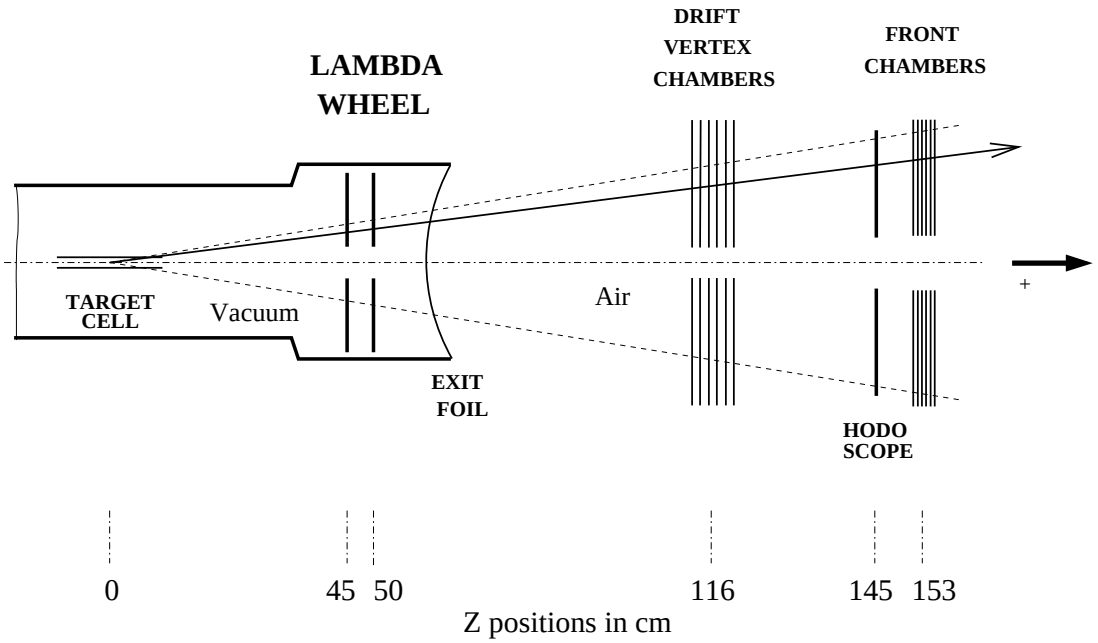

Figure 6.3: *Side view of the HERMES front region.*

6.3.1 HRC Residuals

For the determination of the efficiency front tracks reconstructed with HRC based on the Front Chamber[3] only are used. The intersection of the HRC front tracks with the silicon planes of the module at 45 and 50 cm gives the hit coordinate, which is an estimate of the position where the particle traversed the silicon. As can be seen from figure 6.3 a sizable amount of material is present between the FC and the Lambda Wheel module. Multiple scattering and fit errors in the reconstruction of the HRC tracks result in smeared hit coordinates in the silicon. The residual, i.e. the distance between the hit coordinate and the cluster belonging to the particle, gives a measurement of this smearing. Here, it is assumed that the resolution of the Lambda Wheel detector, which is 46 μm or less perpendicular to the strips, can be neglected as compared to the HRC front track resolution. More than one cluster can be present in a plane due to the passage of more than one particle or due to noise. The contribution of noise clusters is reduced by selecting the cluster with the highest or second highest pulse height. If two clusters are present the one closest to the hit coordinate is taken.

In figure 6.4 the residuals found in the four silicon planes are shown. Besides the smaller number of entries for the junction side of the silicon counter at 50 cm the four

[3]This is the option used during the normal data processing of the HERMES data (FC). In principle the DVC could also be included resulting in more precise tracks.

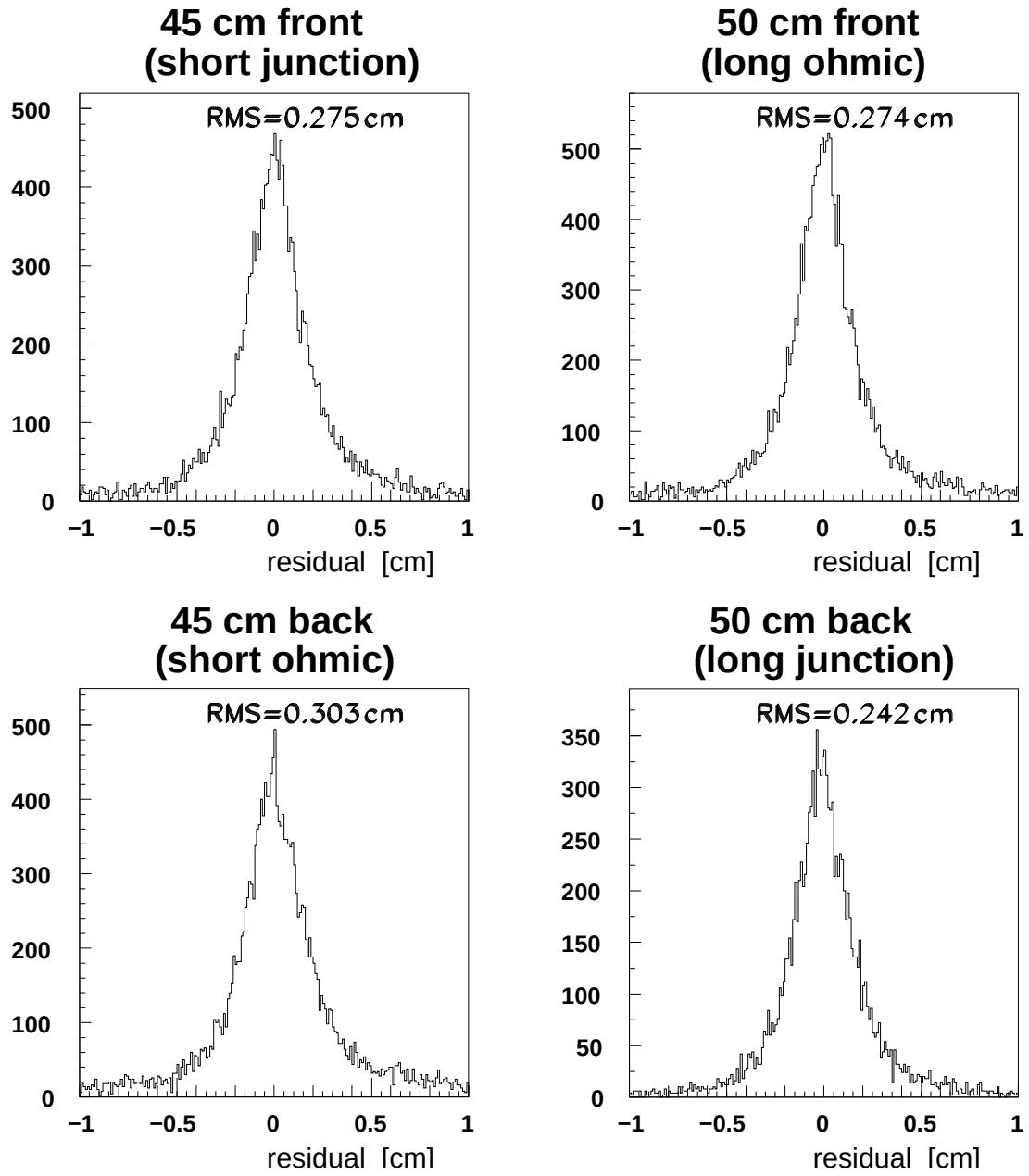

Figure 6.4: *Residuals obtained by comparing* HRC *tracks and* Lambda Wheel *clusters for the four sides of the two silicon planes. The RMS value is evaluated in between -1 cm and 1 cm.*

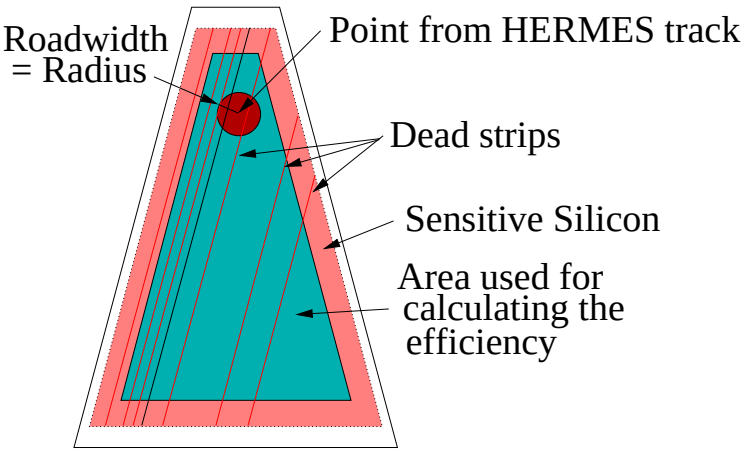

Figure 6.5: *Sketch of a silicon plane. If the coordinate corresponding to the* HERMES *track falls in the darkest area* N_{exp} *is incremented. If a strip with a pulse height above threshold was found in the circle around the hit coordinate* N_{cls} *is incremented.*

residual distributions are comparable. The reason for the smaller count rate in the long junction is a broken chip. The actual RMS value of the residuals (RMS_{res}) of 0.27 cm (average of four planes) can also be understood. Given the resolution of the standard HERMES spectrometer (of 0.6 mrad at best [83]) a standard deviation of $\sigma_{hrc} = 0.06$ cm is expected for a position determination in the Lambda Wheel planes. The difference between RMS_{res} and σ_{hrc} can be accounted for by multiple scattering in the material in between the FC and the Lambda Wheels. From Ref. [85] an estimate of the influence of multiple scattering on the position determination from HRC tracks in the Lambda Wheel planes was obtained as $\sigma^{\pi}_{MS} = 0.18$ cm and $\sigma^{p}_{MS} = 0.25$ cm (for 1 GeV pions and protons, respectively). By comparing these numbers to the observed residuals of 0.27 cm, it is concluded that multiple scattering is the main contributor to the positional resolution of HRC tracks at the position of the Lambda Wheel.

6.3.2 Efficiency determination method

Assuming that there are no dead strips the raw efficiency can be evaluated from

$$\epsilon_r = \frac{N_{\text{cls}}}{N_{\text{exp}}}, \tag{6.3}$$

where N_{cls} is the number of clusters that gave a signal in the Lambda Wheel module, and N_{exp} is the number of clusters expected to give a signal due to the passage of a particle, as determined from HRC. One is added to N_{exp} if the hit coordinate falls in the area used for the efficiency calculation(see figure 6.5). In the efficiency determining

algorithm the number $N_{\rm cls}$ is increased by one, if a cluster is found in the circle around the hit coordinate with radius equal to the roadwidth (see figure 6.5). In order to take care of edge effects not the complete sensitive area of the silicon is taken into account. Instead the sensitive area is reduced by a band along the rim that has a width equal to the roadwidth. In the figure the reduced area is denoted as the area used for calculating the efficiency.

There is a certain freedom in choosing the roadwidth. As an initial guess one could take the RMS_{res} obtained from the measured residuals in the silicon counters. However, assuming that this resolution is Gaussian this choice of roadwidth will only encompass 68% of the tracks. Full efficiency can only be expected if $3\sigma = 0.81$ cm or more is chosen. In the upper left panel of figure 6.6 the measured efficiencies as a function of the roadwidth are shown. The data qualitatively confirm the estimates given above. Differences originate from the non-Gaussian distribution of the residuals (see figure 6.4), and several corrections that need to be applied.

The figure also shows that the obtained efficiency increases with roadwidth as expected, but it is also seen that the efficiency does not become constant for a road width much larger than 3 $\sigma = 0.81$ cm. This is probably due to falsely selected clusters, and hit coordinates which fall outside the Gaussian distribution.

The probability to find a particle cluster in a circle around the hit coordinate increases with the roadwidth, i.e. the radius of the circle. If only real particle clusters are selected the efficiency versus road-width curve will have the real efficiency as its asymptotic value. However, the probability to find a noise cluster also increases with the roadwidth. Ordering the clusters in decreasing pulse height and selecting the first cluster within the roadwidth will reduce the probability to select a noise clusters. Still, for a proper evaluation of the total efficiency, a correction has to be applied for incorrectly selected noise clusters and for the unconnected strips. In the next paragraph the correction of incorrectly selected cluster is explained. Thereafter, a dead strip correction is evaluated.

Correction for incorrectly selected clusters

In order to correct the measured efficiency for incorrectly selected clusters, use is made of the slope of the tracks in the Lambda Wheel module. The reason is that the error introduced in the slope of a track due to multiple scattering is smaller than the error in the position. Therefore, a comparison of the slopes of HERMES tracks with the slopes of tracks of selected clusters in the two planes of a module makes it possible to identify possibly incorrectly selected clusters. As can be seen in figure 6.7 two clusters

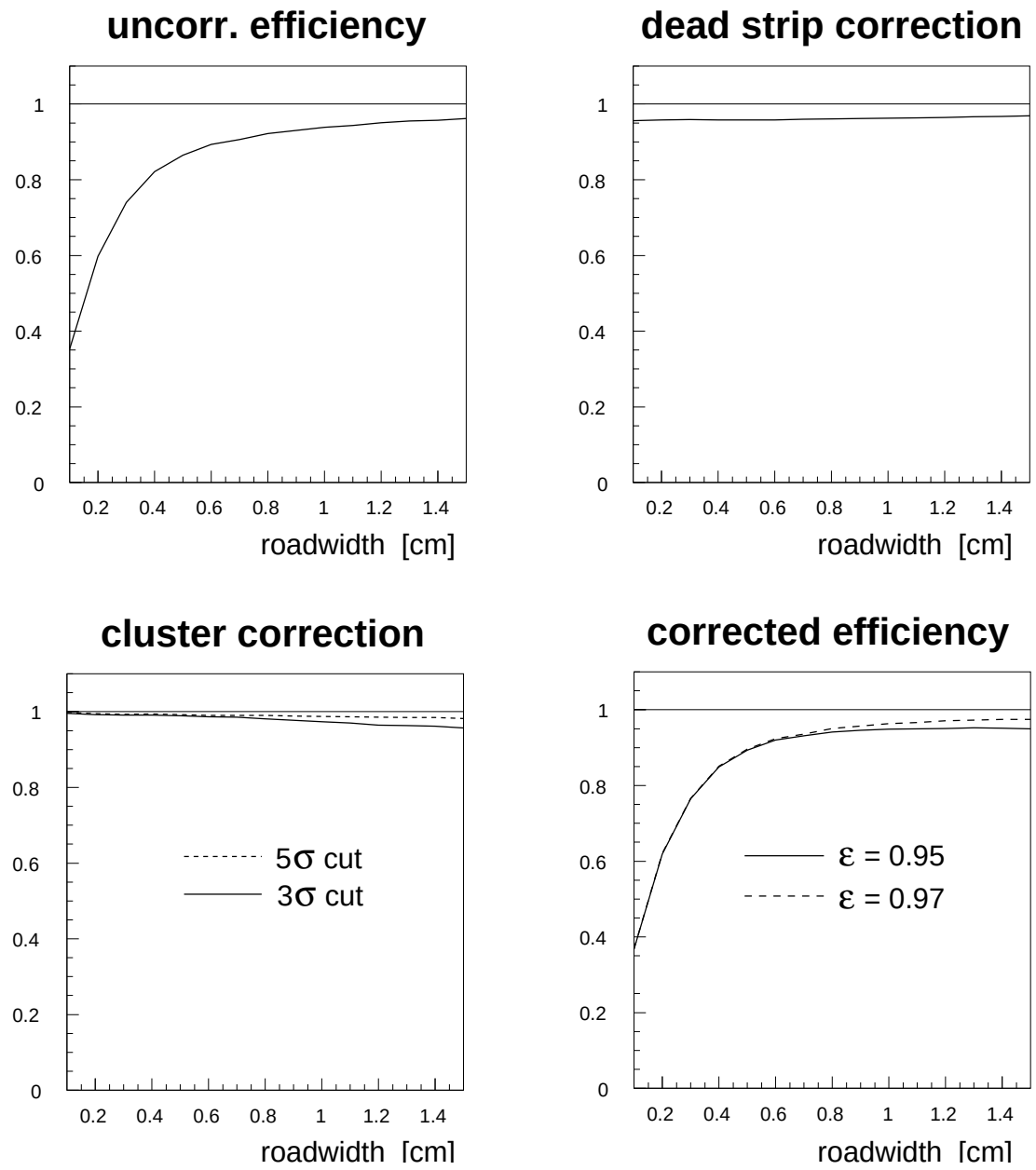

Figure 6.6: *In the upper left panel the efficiency of a single-plane of the* Lambda Wheel *prototype module is shown without corrections. In the upper right panel the correction factor for dead strips is given. In the lower left panel a correction for falsely selected clusters is given, and in the lower right panel the corrected efficiency is shown.*

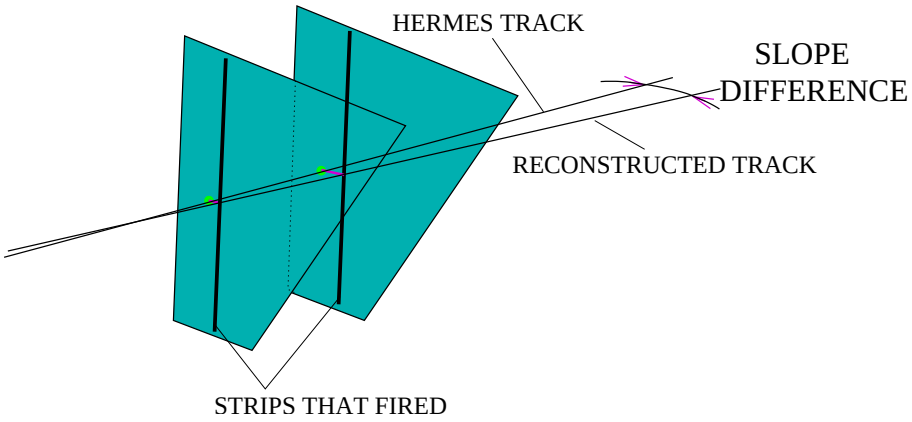

Figure 6.7: *Two silicon planes of a module are sketched. The slope between the HERMES track and the plane (only the projection of the HERMES track on this plane is shown) through the two clusters in the two silicon planes is used to determine a correction factor for incorrectly selected clusters.*

do not define a track but instead a plane, and the slope difference is defined as the angle between the true HERMES (or HRC) track and the plane. In figure 6.8 a clear peak can be seen in the distribution of slope difference signals. The signals outside the peak are due to a cluster in one of the two planes that was incorrectly assigned to the HRC track. The correction factor is now evaluated by counting the signals that are 3σ or 5σ away from the center of the peak, with $\sigma = 2.18$ mrad as obtained from a Gaussian fit through the peak, and dividing by the total number of signals. The value for the standard deviation given above and the minimal angular resolution of 0.6 mrad for HRC tracks indeed shows that the angular resolution estimated for Lambda Wheel tracks of 2.1 mrad (see section 6.2) is an upper limit[4]. Since we are interested in an efficiency per plane the number of outliers has to be divided by two. In the lower left panel of figure 6.6 the thus evaluated correction factor for falsely selected clusters is given as a function of the roadwidth. As can be seen in the figure more cluster are selected falsely if the roadwidth is increased. The linear decrease of the cluster correction factor is expected since the number of strips (and thus the probability to find a noise cluster) in a circle is proportional to the roadwidth.

[4] $\sqrt{2.18^2 - 0.6^2} = 2.1$

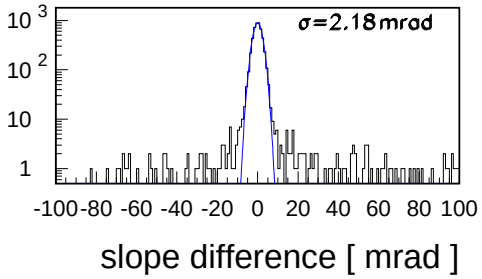

Figure 6.8: *The difference in slope between a* HERMES *track and the plane of tracks made up by two clusters. Both the cluster with the highest pulse height within the roadwidth from the hit coordinate and the next highest cluster in both planes are used. This gives three combinations of which the one with the smallest slope is plotted. The two sidebands come from incorrectly selected clusters in one of the two planes.*

Dead strip Correction

The measured efficiency of the silicon is corrected for dead strips. The correction of the efficiency ϵ is evaluated from the uncorrected efficiency ϵ_{uncorr} by

$$\epsilon = \left[\frac{\Sigma_{i=1}^{N_{\text{exp}}} (1 - F_{\text{dead}})}{N_{\text{exp}}} \right]^{-1} \epsilon_{\text{uncorr}}. \tag{6.4}$$

F_{dead} is the fraction of the area of the circle around the hit coordinate covered with dead strips. It is calculated for each event and is a function of the roadwidth. Averaging these areas over events will effectively weight the position dependent occupancy in the silicon.

In the upper right panel of figure 6.6 the inverse of the multiplicative factor that takes the area of dead strips into account is shown (i.e. the raw efficiency should be divided by this factor). As expected no large dependence on the roadwidth is present.

After applying the dead strip correction and the correction for falsely selected clusters the single-plane efficiency of the Lambda Wheel prototype module is presented in the lower right panel of figure 6.6. Comparison of the upper left panel with the lower right panel shows that the corrections result in an asymptotic value of the efficiency of 95% (97%) if a 3σ (5σ)cut is used. For this reason it is safe to quote a single-plane efficiency of 95% using the 3 σ selection criteria. It is gratifying to observe that the asymptotic efficiency is reached if the roadwidth exceeds 0.81 cm as was already expected on the basis of the intrinsic HERMES resolution. If 5σ constraints are used both for the maximum roadwidth and the slope difference, a single-plane efficiency of 97% is found.

Dependencies of the single-plane efficiencies

The efficiency curves (including all corrections) have also been evaluated for two different bias voltages and for different (software) thresholds on the strip signals. In figure 6.9 the results are shown for both the ohmic and junction sides of the silicon. It is observed that a higher bias voltage and a low threshold lead to the highest efficiencies, as expected.

6.4 Conclusions

In this chapter data taken in the year 2000 with a prototype Lambda Wheel module have been used to study the tracking of particles through the detector. The Lambda Wheel tracking has been incorporated in the XTC program. As only one module has been used in this study, it needs to be extended for the complete Lambda Wheels which were only installed at HERMES in 2002.

An estimate of the resolution that can be obtained with Lambda Wheel tracks is given. Because of the different orientations of the modules the x and y resolution are not constant. An average angular resolution of 2.1 mrad is estimated for tracks only relying on two spacepoints recorded by the Lambda Wheels.

A method to determine the efficiency of the Lambda Wheel that uses HRC tracks has been presented. Using this method the single-plane efficiency of the module has been determined to be 97%. The dependence of the efficiency on the applied bias voltage and the threshold settings has been presented as well. The dependence on the applied threshold is rather strong. Hence, it is necessary to make use of the lowest possible threshold.

The efficiency found for the module is most likely smaller than that for the modules which are now installed in HERMES as several improvements where made to the module series based on experience obtained with this prototype. Hence, it is not unreasonable to expect single-plane efficiencies in excess of 97% for the presently installed silicon modules of the Lambda Wheels.

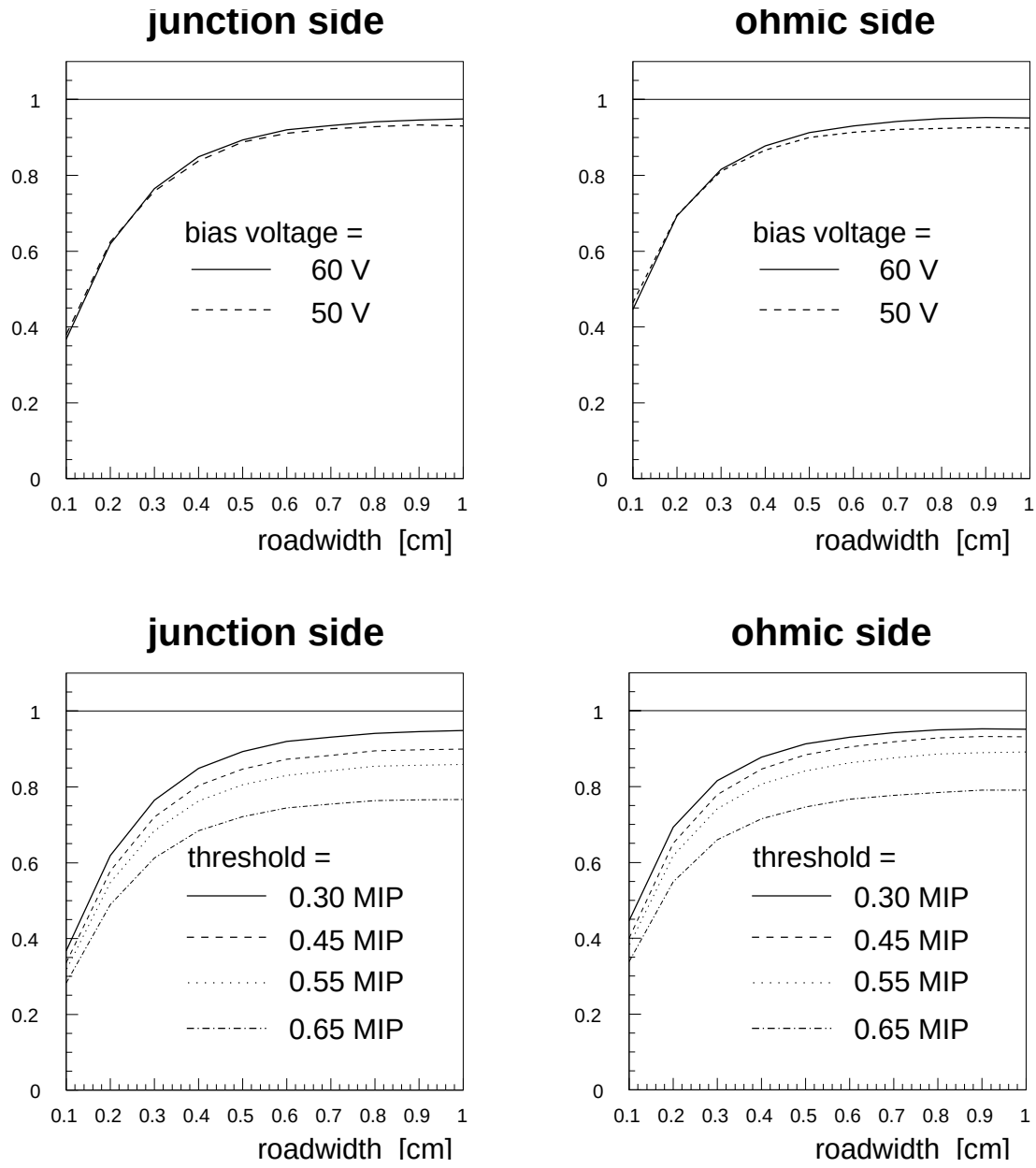

Figure 6.9: *The single-plane efficiency is plotted as a function of the roadwidth for the junction side (left) and the ohmic side (right) of a single silicon counter plane at 45/50 cm from the interaction point. All corrections have been applied. The upper row shows the dependence on two bias voltages, and the lower row the dependence on the (software) threshold applied to the strips. One* MIP *corresponds to 40 ADC-channels.*

Chapter 7

Summary

In this thesis two subjects are discussed that are different but at the same time closely related to each other. The first subject is the study of hyperons produced on a polarized ^{1,2}H target using data taken in the HERMES experiment at DESY. The second subject is the development of a tracking detector, i.e. the Lambda Wheels, that extends the acceptance of the HERMES spectrometer in order to increase the detection probability for Λ^0 hyperons. Data taken with a prototype module of the Lambda Wheels have been used to study the detector performance and to develop tracking software.

The key objective of this work is to obtain additional information on the spin structure of the nucleon. The focus of the analysis is to access the gluon spin contribution to the nucleon spin. A theoretical motivation which starts from a short summary of the Deep Inelastic Scattering framework, introduces the photon-gluon fusion process as a means to access the gluon polarization. A number of background contribution processes is discussed as well as they may also contribute to the results.

A short description of the HERMES experiment is given for a better understanding of the analysis. Important parts of the HERMES experiment like the internal gas target, which is special to the HERMES experiment as it provides a high undiluted target polarization, the tracking chambers of the HERMES spectrometer, the particle identification detectors, the luminosity detector and the trigger and data acquisition systems are discussed.

The analysis involved a search for particles decaying into a Λ hyperon and a π meson. This analysis has been performed on data taken in 1997 on a polarized proton target and in 1998, 1999 and 2000 on a polarized deuterium target.

The production of Ξ and $\Sigma^\star$ hyperons was identified for the first time at HERMES. A

comparison of the yields with the PYTHIA Monte Carlo program shows that PYTHIA sometimes overestimates the data significantly. For the $\Sigma^{\star+}$ hyperon, which decays into a Λ^0 and π^+ PYTHIA overestimates the data by a factor of 7.3. Double spin asymmetries for the Ξ and $\Sigma^\star$ hyperons are mostly zero, except for the $\overline{\Sigma}^{\star+}$, for which a positive asymmetry of 0.44 ± 0.19 is found.

The Λ_c^+ particle is observed through the $\Lambda_c^+ \rightarrow \Lambda^0\pi^+$ decay channel. If this particle is produced primarily by the photo-gluon fusion process, the double spin asymmetry of identified Λ_c^+ baryons might give access to the contribution of gluons to the nucleon spin. In the deuterium data (which correspond to an effective luminosity of 221.92 pb^{-1}) 15.9 ± 7.0 Λ_c^+ events have been observed. Under the assumption that the observed Λ_c^+ baryons are properly simulated with a PGF Monte Carlo this yield leads to an electro-production cross section of

$$\sigma^{lN \rightarrow \Lambda_c^+ \; X} = (14 \; \pm \; 6 \; _{stat} \; \pm \; 5 \; _{syst}) \text{ nb},$$

which has been translated into a photo-production cross section of

$$\sigma^{\gamma N \; \rightarrow \; \Lambda_c^+ \; X} = (538 \; \pm \; 231_{stat} \; \pm \; 188_{syst}) \text{ nb}$$

at a mean photon energy of 15.5 GeV. A comparison of the Λ_c^+ photoproduction cross section with existing total open charm cross sections at the same energy indicate that the Λ_c^+ photoproduction cross section is considerably larger. This apparent inconsistency is probably caused by the fact that the existing total charm cross sections are not directly measured but inferred from D-meson cross sections measurements using the Lund fragmentation model which is not rigorously tested near the threshold for charm production. The larger Λ_c^+ photoproduction cross section could, possibly, be due to an underestimation of the fraction of c quarks that fragment into Λ_c^+ baryons.

The number of observed Λ_c^+ baryons, using the $\Lambda_c^+ \rightarrow \Lambda^0\pi^+$ decay channel, is not enough to extract a double spin asymmetry and therefore additional Λ_c^+ decay channels, i.e. $\Lambda_c^+ \rightarrow \Lambda^0\pi^+X$ were considered. This gives an increase in the Λ_c^+ branching ratio of a factor of 15.

Non-zero asymmetries for partially reconstructed Λ_c^+ baryons are found if the transverse momenta P_{T,Λ^0} and P_{T,Λ_c^+} are taken sufficiently high. Monte Carlo simulations have shown that the sensitivity to PGF increases in the region of (P_{T,Λ^0},P_{T,Λ_c^+})-space where an asymmetry is observed using the AROMA and PYTHIA programs. If the AROMA Monte Carlo is normalized to the observed Λ_c^+ cross section and the PYTHIA background Monte Carlo is normalized to the observed $\Sigma^{\star+}$ yield, the PGF process is found to dominate the background processes in the high (P_{T,Λ^0}, P_{T,Λ_c^+})-domain.

For this reason, we can associate the observed asymmetry with the gluon polarization. After proper normalization of the Monte Carlo programs a value for the gluon spin contribution to the nucleon of

$$\frac{\Delta G}{G} = 0.92 \ \pm \ 0.38 \ _{stat} \ \pm \ 0.40 \ _{syst}$$

at a mean Q^2 of 0.31 GeV^2 is obtained. This value is consistent with the value found in the HERMES high-p_T analysis. Despite remaining model uncertainties, which are hard to estimate in these determinations of $\Delta G/G$, it is striking that the values are consistent. The value is also consistent with $\Delta G/G$=$0.63^{+0.20}_{-0.19}$ at $Q^2 = 1$ GeV^2 obtained from a fit to the world data on inclusive spin-dependent scattering using the Altarelli-Parisi equations.

As the margins of uncertainty are still very large, it is desirable to obtain higher statistics data. For that reason, a wheel-shaped array of silicon detectors, known as the Lambda Wheels, has been developed for the HERMES experiment. The main motivation for building the Lambda Wheels is to increase the angular acceptance of the HERMES spectrometer for the detection of Λ^0 hyperons. Moreover, in the determination of the Λ^0 polarization a false asymmetry is introduced by the incomplete coverage of the acceptance. The Lambda Wheels reduce this false asymmetry to the level of a few percent. Also an extension of the kinematic domain for Λ^0 detection into the target fragmentation domain, i.e. $x_F < 0$ is accessible with the Lambda Wheels.

The design considerations and chosen solutions have been presented and it was found that it is possible to install and operate a system consisting of 12 modules, each comprising two double-sided silicon counters inside the harsh environment of the HERA lepton beam vacuum. Custom made front-end electronics, read-out boards and analogue-to-digital converters were built and shown to be operational.

In the year 2000 the Lambda Wheel infrastructure was installed at the HERMES experiment and a prototype module has been operated during part of that year. The installation of the complete wheel took only place in 2002. Therefore, data taken with the complete wheel installed in the HERMES spectrometer were not available for this thesis.

The data taken with a Lambda Wheel prototype module did, however, make it possible to determine the signal-to-noise ratio of about 10, consistent with the specifications was found. These data have also been used to develop an algorithm for the Lambda Wheels tracking, which was incorporated in the eXtended Tracking Code (XTC). This code is used for additional detectors at HERMES that have a relatively large acceptance,

like the Drift Vertex Chambers (DVC). This code complements the HERMES Reconstruction Code (HRC).

An estimate is given for the coordinate and angular resolutions of the Lambda Wheel tracks under the assumption that only one strip per side has a signal above threshold. Because each module is positioned differently, the x and y resolutions are not constant and range from 46 to 122 μm. An average angular resolution of 2.1 mrad has been determined for the Lambda Wheel tracks.

Using a method to determine the efficiency of the Lambda Wheels that makes use of HRC tracks a single-plane efficiency of 97% has been determined. The dependence of the efficiency on the applied bias voltage and the threshold settings has been measured as well.

With the Lambda Wheels fully installed, the number of Λ^0 hyperon events per unit luminosity will increase by a factor four. This will make it possible to study the Λ_c^+ cross section with a better significance, thereby, reducing the statistical and systematic error given for the $\Delta G/G$ value determined from partially reconstructed Λ_c^+ baryons.

Chapter 8

Samenvatting

Er worden twee gerelateerde onderwerpen behandeld in dit proefschrift. Het eerste onderwerp gaat over hyperonen[1] die geproduceerd worden door leptonen[2] te verstrooien aan gepolariseerd atomair ^{1}H of ^{2}H gas. Hiervoor worden gegevens gebruikt die zijn verkregen in het HERMES experiment dat zich by het Duitse deeltjes fysica instituut DESY in Hamburg bevindt. Als tweede onderwerp wordt een deeltjes detector beschreven waarmee de acceptatie van de HERMES spectrometer vergroot wordt, zodat er een grotere waarschijnlijkheid is om een Λ^0 deeltje waar te nemen. Omdat er alleen gegevens met een prototype van deze zogenoemde Lambda Wheel detector zijn verkregen konden er voor de hyperon analyse geen Lambda Wheels gegevens worden gebruikt.

De voornaamste motivatie voor de beschreven analyses is het verkrijgen van additionele informatie over de spinstructuur van nucleonen[3]. De analyse richt zich in het bijzonder op het bepalen van de bijdrage van gluonen[4] aan de spin van het nucleon. De theoretische motivatie start met een korte introductie in diep-inelastische verstrooiing, waarna het foton-gluonfusieproces wordt beschreven. Dit proces stelt ons in staat om de gluonspin contributie aan de spin van het nucleon te bepalen omdat in dit proces juist één gluon wordt uitgewisseld tussen het foton en de quarks in het nucleon. Een aantal achtergrondprocessen die van invloed zijn op de metingen worden ook beschreven.

Het HERMES experiment wordt kort beschreven voor een beter begrip van de ana-

[1] Hyperonen zijn deeltjes zoals de Λ^0 met een structuur die lijkt op die van het proton of een neutron (de bouwstenen van de atoomkern) waarin één van de up of down quarks vervangen is door en strange quark.

[2] Leptonen zijn in dit verband elektronen of positronen.

[3] Nucleon is een verzamelnaam voor protonen en neutronen.

[4] Gluonen dragen de sterke kernkracht over en zorgen voor de binding van de quarks in een nucleon.

lyse en de nieuw ontwikkelde Lambda Wheels. Belangrijke delen van het experiment komen aan de orde zoals de stroom van gepolariseerd atomair gas dat het mogelijk maakt atomen van een zeer hoge polarisatie te gebruiken, de spoorreconstructiekamers, deeltjes-identificatiedetectoren, een detector voor het bepalen van de luminositeit, een systeem dat de meting initieert en een systeem voor het verzamelen van de meetgegevens.

De analyse gaat over baryonen, d.w.z. deeltjes bestaand uit drie quarks, die in een Λ hyperon en een π meson vervallen. De gegevens voor de analyse zijn verkregen door verstrooiing van leptonen aan een gepolariseerd proton gas (in 1997) en een gepolariseerd deuterium gas (in de jaren 1998, 1999 en 2000).

Voor de eerste keer zijn de Ξ en $\Sigma^\star$ deeltjes waargenomen in meetgegevens verkregen met behulp van het HERMES experiment. Uit een vergelijking van de waargenomen hoeveelheid deeltjes met een voorspelling gedaan met behulp van het PYTHIA Monte Carlo programma volgt dat PYTHIA een te grote opbrengst voorspelt. Voor het $\Sigma^{\star +}$ deeltje, dat in een Λ^0 en een π^+ deeltje vervalt, geeft PYTHIA een 7.3 keer te grote opbrengst. De gegevens zijn ook gebruikt om dubbele spin-asymmetrieën te bepalen voor de Ξ hyperonen. In vrijwel alle gevallen bleek deze asymmetrie consistent met nul te zijn. Uitzondering is het $\overline{\Sigma}^{\star +}$ deeltje waarvoor een positieve asymmetrie is gevonden van 0.44 ± 0.19. Er is geen verklaring gevonden voor deze waarneming.

Het Λ_c^+ deeltje is waargenomen in het vervalskanaal $\Lambda_c^+ \rightarrow \Lambda^0 \pi^+$. Wanneer dit deeltje voornamelijk wordt geproduceerd door het foton-gluonfusieproces, dan is de dubbele spin-asymmetrie van geïdentificeerde Λ_c^+ deeltjes te gebruiken voor het bepalen van de polarisatie van gluonen in het nucleon. In de gegevens verkregen door verstrooiing van leptonen aan gepolariseerde deuteriumatomen met zijn 15.9 ± 7.0 Λ_c^+ deeltjes gevonden. Onder de aanname dat het productieproces van deze Λ_c^+ deeltjes correct gesimuleerd kan worden door het AROMA PGF Monte Carlo programma kan een acceptatie van het HERMES experiment bepaald worden. Op basis hiervan kan een werkzame doorsnede bepaald worden voor electroproductie van Λ_c^+ deeltjes

$$\sigma^{lN \rightarrow \Lambda_c^+ \; X} = (14 \; \pm \; 6 \; _{stat} \; \pm \; 5 \; _{syst}) \text{ nb.}$$

Uit de electroproductie werkzame doorsnede is een foton productie werkzame doorsnede van

$$\sigma^{\gamma N \; \rightarrow \; \Lambda_c^+ \; X} = (538 \; \pm \; 231_{stat} \; \pm \; 188_{syst}) \text{ nb}$$

voor een gemiddelde foton energie van 15.5 GeV afgeleid. Een vergelijking van deze werkzame doorsnede voor foton productie met uit de literatuur bekende totale open

charm werkzame doorsneden geven aan dat de hier gevonden waarde aanzienlijk hoger is. Deze ogenschijnlijke tegenstrijdigheid is waarschijnlijk een gevolg van het feit dat de totale open-charm werkzame doorsneden zijn afgeleid uit gemeten D-meson werkzame doorsneden. Om van de D-meson werkzame doorsnede naar de totale open charm werkzame doorsnede te komen is er gebruik gemaakt van het Lund fragmentatie model waarvan niet bekend is of dat in het drempelgebied voor Λ_c^+ productie gebruikt mag worden. De gevonden hogere Λ_c^+ werkzame doorsnede voor foton-productie is mogelijk het gevolg van een onderschatting in het Lund model van de fractie van het aantal c quarks dat in een Λ_c^+ deeltje fragmenteren.

Het aantal gevonden Λ_c^+ deeltjes in het vervalskanaal $\Lambda_c^+ \rightarrow \Lambda^0\pi^+$ is onvoldoende voor het bepalen van een dubbele spin-asymmetrie. Er is daarom gekozen om andere vervalskanalen ($\Lambda_c^+ \rightarrow \Lambda^0\pi^+X$) mee te nemen voor de bepaling van de asymmetrie, zodat de totale vertakkingsverhouding een factor 15 groter wordt. Het is nu niet mogelijk om het Λ_c^+ deeltje compleet te reconstrueren omdat het deel X niet waargenomen wordt en daarom spreken we over partiële reconstructie.

Asymmetrieën ongelijk aan nul zijn er gevonden voor partieel gereconstrueerde Λ_c^+ deeltjes indien de transversale impulsen P_{T,Λ^0} en P_{T,Λ_c^+} voldoende hoog worden gekozen. Uit simulaties gedaan met Monte Carlo programma's blijkt dat de gevoeligheid om PGF geïnduceerde gebeurtenissen waar te nemen inderdaad toeneemt in het gebied van de (P_{T,Λ^0},P_{T,Λ_c^+})-ruimte waar een asymmetrie wordt gevonden. Wanneer de opbrengst verkregen met het AROMA Monte Carlo programma wordt genormaliseerd op het aantal gevonden Λ_c^+ deeltjes en de opbrengst verkregen met het PYTHIA Monte Carlo programma op het aantal gevonden $\Sigma^{\star+}$ deeltjes kan worden aangetoond dat het PGF proces dominant is in het hoge P_{T,Λ^0}, P_{T,Λ_c^+} domein. Om deze reden is er voor gekozen om de waargenomen asymmetrie in dit bereik te associëren met de gluon polarisatie. Na de juiste normalisatie van de gebruikte Monte Carlo programma's wordt er een waarde voor de gluon spin-bijdrage aan het nucleon van

$$\frac{\Delta G}{G} = 0.92 \ \pm \ 0.38 \ _{stat} \ \pm \ 0.40 \ _{syst}$$

voor een gemiddelde Q^2 van 0.31 GeV^2 gevonden. Deze waarde is consistent met de waarde gevonden in een eerdere HERMES analyse waarin er twee deeltjes die een hoge transversale impuls hebben worden geeist. Dit mag men opmerkelijk noemen vanwege het feit dat er in beide analyses een grote afhankelijkheid is van de gebruikte Monte Carlo programma's. Door het verschil in analyses is er echter geen wederzijdse afhankelijkheid in de gebruikte Monte Carlo programma's onderling. Verder is de gevonden waarde ook consistent met de waarde $\Delta G/G$=$0.63^{+0.20}_{-0.19}$ voor $Q^2 = 1$ GeV^2 verkregen uit een fit aan alle beschikbare gegevens van inclusieve spinafhankelijke verstrooiing

gebruikmakend van de Altarelli-Parisi vergelijkingen.

Om de statistisch onzekerheden te verkleinen is het nodig om extra metingen te doen. Om bij gelijke luminositeit toch meer gegevens te kunnen verkrijgen is er een nieuwe detector in het HERMES experiment ingebouwd. Deze detector, bekend onder de naam Lambda Wheels is voornamelijk ontworpen om de acceptatie van het HERMES experiment voor de detectie van Λ^0 deeltjes te vergroten. Verder is het nu ook mogelijk om de Λ^0 polarisatie met sterk gereduceerde valse asymmetrieën welke een gevolg is van een onvolledige acceptatie, te bepalen. De Lambda Wheels verminderen de valse asymmetrie tot op het niveau van enkele procenten. Ook zal het kinematische domein voor gereconstrueerde Λ^0 deeltjes dat toegankelijk is in het HERMES experiment worden vergroot. Gedetecteerde Λ^0 deeltjes kunnen nu afkomstig zijn van quarks in het nucleon die geen interactie met het virtuele foton hebben ondergaan (target fragmentation).

De overwegingen die een rol speelden tijdens het ontwerp en de uiteindelijk gekozen oplossingen zijn gepresenteerd. Het is gebleken dat het mogelijk is om een systeem bestaande uit 12 modulen, elk bestaande uit twee aan beide zijden gevoelig silicium, werkzaam te krijgen in het vacum van de HERA leptonen bundel waarin een hoog stralingsniveau heerst. Van op het NIKHEF gemaakte front-end elektronica, uitleesborden en analoog-naar- digitaal omzetters is ook aangetoond dat ze werken.

In 2000 is de infrastructuur van de Lambda Wheels geïnstalleerd in het HERMES experiment en een prototype module heeft gedurende een gedeelte van dat jaar gegevens verzameld. De installatie van het complete wiel heeft pas in 2002 plaatsgevonden. Een consequentie daarvan is dat er geen gegevens beschikbaar waren gebaseerd op het gehele Lambda Wheels systeem die in dit proefschrift gebruikt hadden konden worden.

De gegevens die met het Lambda Wheel prototype zijn verzameld maken het mogelijk om een signaal-over-ruis verhouding van 10 te meten, hetgeen consistentie is met de specificaties. De gegevens zijn ook voor het ontwikkelen van een algoritme gebruikt voor de reconstructie van Lambda Wheels sporen welke toegevoegd is in een code die voor alle detectoren met relatief grote acceptatie dient. Deze code complementeert een bestaande reconstructie code voor de standaard acceptatie en wordt bijvoorbeeld ook gebruikt voor de Drift Vertex kamer.

Er is een schatting gegeven van de coördinaat- en hoek-resolutie van Lambda Wheels sporen onder de aanname dat een deeltje één strip per zijde met een signaal boven de drempel geeft. Omdat elke module een andere positionering heeft variëren de resolutie in de x en y richting, ze liggen tussen de 46 en 122 μm. Er is een gemiddelde hoek

resolutie van 2.1 mrad voor de Lambda Wheels sporen gevonden.

Gebruik makend van de HRC sporen is er een methode ontwikkeld om de efficiëntie van de siliciumdetectoren te meten. Er is een efficiëntie per vlak van 97% gevonden. De afhankelijkheid van de efficiëntie op de toegepaste bias voltage en de gestelde drempelwaarden is ook gemeten.

Met het complete Lambda Wheels geïnstalleerd, zal het aantal gedetecteerde Λ^0 deeltjes per luminositeitseenheid een factor vier hoger zijn dan zonder Lambda Wheels. Als gevolg zal het in de toekomst mogelijk zijn om de Λ_c^+ werkzame doorsnede met een hogere significantie te bepalen en zodoende zal ook de statische en systematische fout voor de gemeten $\Delta G/G$ waardes worden verkleind.

Appendix:
Pythia parameter settings

Table 8.1: *Settings of parameters in* PYTHIA *used for the generation of the* $\Lambda\pi$ *background spectrum.*

I	MSTU	PARU	MSTJ	PARJ	PARF
1	0	3.14159	1	0.10000	0.50000
2	0	6.28319	3	0.16000	0.25000
3	0	0.19733	0	0.40000	0.50000
4	4000	5.06773	0	0.05000	0.25000
5	10000	0.38938	0	0.50000	1.00000
6	500	2.56819	0	0.50000	0.50000
7	4000	0.00000	0	0.50000	0.00000
8	0	0.00000	0	0.60000	0.00000
9	0	0.00000	0	1.20000	0.00000
10	2	0.00000	0	0.60000	0.00000
11	6	0.00100	4	0.50000	0.50000
12	0	0.09000	2	0.60000	0.00000
13	1	0.01000	0	0.75000	0.50000
14	0	0.00000	1	0.00000	0.00000
15	1	0.00000	0	0.00000	1.00000
16	1	0.00000	2	0.00000	1.00000
17	0	0.00000	2	0.00000	0.00000
18	0	0.00000	0	1.00000	0.00000
19	0	0.00000	0	1.00000	0.00000
20	1	0.00000	0	0.00000	0.00000
21	2	0.00000	2	0.33000	0.50000
22	10	0.00000	1	1.00000	0.00000
23	0	0.00000	1	0.01000	0.50000
24	0	0.00000	2	2.00000	0.00000
25	1	0.00000	1	1.00000	1.00000
26	10	0.00000	2	0.40000	1.00000
27	0	0.00000	2	0.00000	0.00000
28	0	0.00000	0	0.00000	0.00000
29	0	0.00000	0	0.00000	0.00000
30	0	0.00000	0	0.00000	0.00000
31	0	0.00000	0	0.10000	0.50000
32	0	0.00000	0	1.00000	0.00000
33	0	0.00000	0	0.80000	0.50000
34	0	0.00000	0	1.50000	0.00000
35	0	0.00000	0	0.00000	1.00000

I	MSTU	PARU	MSTJ	PARJ	PARF
36	0	0.00000	0	2.00000	1.00000
37	0	0.00000	0	0.20000	0.00000
38	0	0.00000	0	0.00000	0.00000
39	0	0.00000	0	0.08000	0.00000
40	0	0.00000	0	0.00000	0.00000
41	2	2.00000	2	0.89000	0.50000
42	2	1.00000	2	0.24000	0.00000
43	1	0.25000	4	0.50000	0.50000
44	4	2.50000	2	0.90000	0.00000
45	2	0.05000	5	0.50000	1.00000
46	1	0.00000	3	1.00000	1.00000
47	1	0.00000	3	1.00000	0.00000
48	0	0.00010	0	1.00000	0.00000
49	0	0.00000	0	0.00000	0.00000
50	0	0.00000	3	0.00000	0.00000
51	25	2.50000	0	0.77000	0.50000
52	24	1.50000	3	0.77000	0.00000
53	0	7.00000	0	0.77000	0.50000
54	1	1.00000	2	-0.05000	0.00000
55	0	0.50000	0	-0.00500	1.00000
56	0	2.00000	0	-0.00001	1.00000
57	0	3.20000	1	-0.00001	0.00000
58	0	0.00000	0	-0.00001	0.00000
59	0	0.00000	0	1.00000	0.00000
60	0	0.00000	0	0.00000	0.00000
61	0	0.00000	0	4.50000	0.75000
62	0	0.00000	0	0.70000	0.50000
63	0	0.00000	0	0.00000	0.00000
64	0	0.00000	0	0.00300	0.16670
65	0	0.00000	0	0.50000	0.08330
66	0	0.00000	0	0.50000	0.16670
67	0	0.00000	0	0.00000	0.00000
68	0	0.00000	0	0.00000	0.00000
69	0	0.00000	0	0.00000	0.00000
70	0	0.00000	0	0.00000	0.00000

Table 8 continued.

I	MSTU	PARU	MSTJ	PARJ	PARF
71	0	0.00000	0	10.00000	0.00000
72	0	0.00000	0	1000.00000	0.00000
73	0	0.00000	0	100.00000	1.00000
74	0	0.00000	0	1000.00000	0.33330
75	0	0.00000	0	0.00000	0.66670
76	0	0.00000	0	0.70000	0.33330
77	0	0.00000	0	10.00000	0.00000
78	0	0.00000	0	0.00000	0.00000
79	0	0.00000	0	0.00000	0.00000
80	0	0.00000	0	0.00000	0.00000
81	0	0.00000	0	0.29000	0.00000
82	0	0.00000	0	1.00000	0.00000
83	0	0.00000	0	1.00000	0.00000
84	0	0.00000	0	0.00000	0.00000
85	0	0.00000	0	10.00000	0.00000
86	0	0.00000	0	10.00000	0.00000
87	0	0.00000	0	0.00000	0.00000
88	0	0.00000	0	0.00000	0.00000
89	0	0.00000	0	0.00000	0.00000
90	0	0.00000	0	0.00010	0.00000
91	0	0.00000	0	0.02000	0.00990
92	0	0.00000	0	1.00000	0.00560
93	0	0.00000	0	0.20000	0.19900
94	0	0.00000	0	0.00000	1.35000
95	0	0.00000	0	0.00000	4.50000
96	0	0.00000	0	0.00000	0.00000
97	0	0.00000	0	0.00000	0.00000
98	0	0.00000	0	0.00000	0.00000
99	0	0.00000	0	0.00000	0.00000
100	0	0.00000	0	0.00000	0.00000
101	1	0.00730	5	0.00000	0.32500
102	0	0.23200	2	0.00000	0.32500
103	0	0.00776	7	0.00000	0.50000
104	0	1.00000	3	0.00000	1.60000
105	0	0.00001	1	0.00000	5.00000
106	0	0.00000	1	0.00000	0.00000
107	0	0.00000	0	0.00000	0.00000
108	0	0.00741	2	0.00000	0.00000
109	0	0.00000	0	0.00000	0.00000
110	0	0.00000	2	0.00000	0.00000
111	1	0.20000	0	0.00000	0.00000
112	4	0.20000	0	0.00000	0.11000
113	3	1.00000	0	0.00000	0.16000
114	5	4.00000	0	0.00000	0.04800
115	0	10.00000	1	0.00000	0.50000
116	0	0.00000	1	0.00000	0.45000
117	0	0.23219	0	0.00000	0.55000
118	3	0.58330	0	0.00000	0.60000
119	0	0.00000	0	0.00000	0.00000
120	0	0.00000	0	0.00000	0.00000
121	0	-0.69300	0	1.00000	0.20000
122	0	-1.00000	0	0.25000	0.10000
123	1	0.38700	0	91.18700	0.00000
124	0	1.00000	0	2.47857	0.00000
125	0	-0.08000	0	0.01000	0.00000
126	0	-1.00000	0	2.00000	0.00000
127	0	1.00000	0	1.00000	0.00000
128	0	1.00000	0	0.25000	0.00000
129	0	1.00000	0	0.00200	0.00000
130	0	0.00000	0	0.00000	0.00000
131	0	1.00000	0	0.00000	1.09575
132	0	-1.00000	0	0.00000	2.30837
133	0	1.00000	0	0.00000	1.54779
134	0	-1.00000	0	0.00000	1.00454
135	0	1.00000	0	0.01000	0.27851
136	0	0.00000	0	0.99000	0.69628
137	0	0.00000	0	0.00000	1.10629
138	0	0.00000	0	0.00000	0.50000
139	0	0.00000	0	0.20000	0.00000
140	0	0.00000	0	0.00000	0.00000

Table 8 continued.

I	MSTU	PARU	MSTJ	PARJ	PARF
141	0	5.00000	0	0.00000	0.75000
142	0	1.00000	0	0.00000	0.75000
143	0	1.00000	0	0.00000	0.75000
144	0	0.00000	0	0.00000	0.75000
145	0	1.00000	0	0.00000	1.00000
146	0	1.00000	0	0.00000	1.00000
147	0	0.00000	0	0.00000	0.00000
148	0	0.00000	0	0.00000	0.00000
149	0	0.00000	0	0.00000	0.00000
150	0	0.00000	0	0.00000	0.00000
151	0	1.00000	0	0.00000	0.09167
152	0	0.00000	0	0.00000	0.09497
153	0	0.00000	0	0.00000	0.02226
154	0	0.00000	0	0.00000	0.25806
155	0	1000.00000	0	0.00000	0.15000
156	0	1.00000	0	0.00000	0.15000
157	0	1.00000	0	0.00000	0.15000
158	0	1.00000	0	0.00000	0.00000
159	0	1.00000	0	0.00000	0.00000
160	0	0.00000	0	0.00000	0.00000
161	0	1.00000	0	0.00000	0.24498
162	0	1.00000	0	0.00000	0.04887
163	0	1.00000	0	0.00000	0.05417
164	0	1.00000	0	0.00000	0.51706
165	0	1.00000	0	0.00000	0.67082
166	0	0.00000	0	0.00000	0.67082
167	0	0.00000	0	0.00000	0.67082
168	0	0.00000	0	0.00000	0.00000
169	0	0.00000	0	0.00000	0.00000
170	0	0.00000	0	0.00000	0.00000
171	0	1.00000	0	0.00000	0.27851
172	0	1.00000	0	200.00000	0.05613
173	0	1.00000	0	200.00000	0.04063
174	0	1.00000	0	0.33300	0.44536
175	0	1.00000	0	0.05000	0.67082
176	0	1.00000	0	0.00000	0.67082
177	0	1.00000	0	0.00000	0.67082
178	0	0.00000	0	0.00000	0.00000
179	0	0.00000	0	0.00000	0.00000
180	0	0.00000	0	-0.69300	0.00000
181	0	1.00000	0	-1.00000	0.00000
182	0	1.00000	0	0.38700	0.00000
183	0	1.00000	0	1.00000	0.00000
184	0	0.00000	0	-0.08000	0.00000
185	0	0.00000	0	-1.00000	1.00000
186	0	1.00000	0	1.00000	1.00000
187	0	1.00000	0	1.00000	1.00000
188	0	0.00000	0	-0.69300	0.00000
189	0	0.00000	0	-1.00000	0.00000
190	0	0.00000	0	0.38700	0.00000
191	0	0.00000	0	1.00000	0.20000
192	0	0.00000	0	-0.08000	0.50000
193	0	0.00000	0	-1.00000	0.00000
194	0	0.00000	0	1.00000	0.00000
195	0	1.00000	0	1.00000	0.00000
196	0	0.00000	0	0.00000	0.00000
197	0	0.00000	0	0.00000	0.00000
198	0	0.00000	0	0.00000	0.00000
199	0	0.00000	0	0.00000	0.00000
200	0	0.00000	0	0.00000	0.00000

Bibliography

[1] J. Ashman *et al.* A measurement of the spin asymmetry and determination of the structure function g_1 in deep-inelastic muon-proton scattering. *Phys. Lett.*, B206:364, 1988.

[2] K. Goeke, Maxim V. Polyakov, and M. Vanderhaeghen. Hard exclusive reactions and the structure of hadrons. *Prog. Part. Nucl. Phys.*, 47:401–515, 2001.

[3] John R. Ellis, Dmitri Kharzeev, and Aram Kotzinian. The proton spin puzzle and lambda polarization in deep inelastic scattering. *Z. Phys.*, C69:467–474, 1996.

[4] F. Halzen and A. D. Martin. *Quarks & leptons: An Introductory Course in Modern Particle Physics*. John Wiley & Sons, 1984.

[5] J.P. Albanese *et al.* Quark charge retention in final state hadrons from deep-inelastic muon scattering. *Phys. Lett.*, B144:302, 1984.

[6] M. C. Simani. *Flavour decomposition of the nucleon spin at HERMES*. PhD thesis, Vrije Universiteit te Amsterdam, The Netherlands, October 2002.

[7] B. Andersson, G. Gustafson, G. Ingelmann, and T. Sjöstrand. Parton fragmentation and string dynamics. *Phys. Rep.*, 97:31, 1983.

[8] A. Airapetian et al. Measurement of the proton spin structure function g1(p) with a pure hydrogen target. *Phys. Lett.*, B442:484–492, 1998.

[9] S.I. Adler. Axial vector vertex in spinor electrodynamics. *Phys. Rev.*, 177:2426, 1969.

[10] J.S. Bell and R. Jackiw. A PCAC puzzle: $\pi^0 \to \gamma\gamma$ in the sigma model. *Nuovo Cimento*, A60:47, 1969.

[11] J. Lichtenstadt. QCD analysis of spin structure function data from present and prospective measurements. *Nucl. Phys. Proc. Suppl.*, 105:86–89, 2002.

[12] Alessandro Bravar, Dietrich von Harrach, and Aram Kotzinian. Large gluon polarization from correlated high-p(t) hadron pairs in polarized electro-production. *Phys. Lett.*, B421:349–359, 1998.

[13] A. Airapetian et al. Measurement of the spin asymmetry in the photoproduction of pairs of high-p_T hadrons at HERMES. *Phys. Rev. Lett.*, 84:2584–2588, 2000.

[14] Torbjorn Sjostrand, Leif Lonnblad, and Stephen Mrenna. Pythia 6.2: Physics and manual. 2001.

[15] Christer Friberg and Torbjorn Sjostrand. Total cross sections and event properties from real to virtual photons. *JHEP*, 09:010, 2000.

[16] George Japaridze, Wolf-Dieter Nowak, and Avto Tkabladze. Color octet contribution to J/Ψ photoproduction asymmetries. *Phys. Rev.*, D62:034022, 2000.

[17] A. D. Watson. Spin-spin asymmetries in inclusive muon proton charm production. *Z. Phys.*, C12:123, 1982.

[18] M. Gluck and E. Reya. Spin dependent parton distributions in polarized deep inelastic lepton nucleon scattering. *Z. Phys.*, C39:569, 1988.

[19] R. K. Ellis and P. Nason. Qcd radiative corrections to the photoproduction of heavy quarks. *Nucl. Phys.*, B312:551, 1989.

[20] J. Smith and W. L. van Neerven. Qcd corrections to heavy flavor photoproduction and electroproduction. *Nucl. Phys.*, B374:36–82, 1992.

[21] G. Baum et al. COMPASS: A proposal for a common muon and proton apparatus for structure and spectroscopy. CERN-SPSLC-96-14.

[22] Alessandro Bravar, Krzysztof Kurek, and Roland Windmolders. Poldis: A Monte Carlo for polarized (semi-inclusive) deep inelastic scattering. *Comput. Phys. Commun.*, 105:42–61, 1997.

[23] T. O. Eynck and S.-O. Moch. Soft gluon resummation for polarized deep-inelastic production of heavy quarks. *Phys. Lett.*, B498:23–28, 2000.

[24] S. J. Brodsky, P. Hoyer, C. Peterson, and N. Sakai. The intrinsic charm of the proton. *Phys. Lett.*, B93:451–455, 1980.

[25] J. Blumlein and W. L. van Neerven. Heavy flavour contributions to the deep inelastic sum rules. *Phys. Lett.*, B450:417–426, 1999.

[26] S. J. Brodsky, E. Chudakov, P. Hoyer, and J. M. Laget. Photoproduction of charm near threshold. *Phys. Lett.*, B498:23–28, 2001.

[27] M. Ryskin and E. Leader. Contamination of spin asymmetry in charm production. *J. Phys.*, G25:1541–1543, 1999.

[28] Michail P. Rekalo and Egle Tomasi-Gustafsson. Associative photoproduction of charmed particles near threshold. *Phys. Lett.*, B500:53–58, 2001.

[29] M. Burkardt and R. L. Jaffe. Polarized q $\rightarrow \Lambda$ fragmentation functions from e+ e- $\rightarrow \Lambda + X$. *Phys. Rev. Lett.*, 70:2537–2540, 1993.

[30] A. Airapetian et al. Measurement of longitudinal spin transfer to lambda hyperons in deep-inelastic lepton scattering. *Phys. Rev.*, D64:112005, 2001.

[31] C Chiang and N. C. R. Makins. Talk during HERMES analysis week. February 2002.

[32] A. A. Sokolov and I. M. Ternov. *Sov. Phys. Dokladi*, 8:1203, 1964.

[33] D.P. Barber *et al.* The HERA polarimeter and the first observation of electron spin polarization. *Nucl. Instr. Meth.*, A338:21, 2000.

[34] M. Beckmann *et al.* The longitudinal polarimeter at HERA. *Nucl. Instr. Meth.*, A461:21, 2000.

[35] HERMES collaboration. HERMES technical design report. *DESY-PRC-93-06*, 1993.

[36] J. Blouw *et al.* Design and performance of a large microstrip gas tracker for HERMES. *Nucl. Instrum. Meth.*, A434:227–243, 1999.

[37] D. Ryckbosch. The HERMES RICH detector. *Nucl. Instrum. Meth.*, A433:98–103, 1999.

[38] N. Akopov et al. The HERMES dual-radiator ring imaging čerenkov detector. *Nucl. Instrum. Meth.*, A479:511–530, 2002.

[39] H. Avakian et al. The HERMES electromagnetic calorimeter. Prepared for 6th International Conference on Calorimetry in High-energy Physics (ICCHEP 96), Rome, Italy, 8-14 Jun 1996.

[40] H. Avakian et al. Performance of the electromagnetic calorimeter of the HERMES experiment. *Nucl. Instrum. Meth.*, A417:69–78, 1998.

[41] T. Benisch et al. The luminosity monitor of the HERMES experiment at DESY. *Nucl. Instrum. Meth.*, A471:314–324, 2001.

[42] I. McLaren et al. *EPIO - Expertimental Physics Input Output Package, Cern Program Library Long Writeup I101.* Cern CN Division, Application Software and Databases Group, Geneva, Switzerland, 1993.

[43] Programming Techniques Group. *Adamo - An entity-relationship programming system, Version 3.3.* ECP Division, CERN, Geneva, 1994.

[44] E. Leader. Spin in particle physics. *Cambridge Monogr. Part. Phys. Nucl. Phys. Cosmol.*, 15:1, 2001.

[45] B. W. Filippone and Xiang-Dong Ji. The spin structure of the nucleon. 2001.

[46] G. van der Steenhoven. Polarized structure functions. In *Proceedings Baryons 2002*, Singapore, August, 2002.

[47] Xiang-Dong Ji. Deeply-virtual Compton scattering. *Phys. Rev.*, D55:7114–7125, 1997.

[48] A. Airapetian et al. Measurement of the beam spin azimuthal asymmetry associated with deeply-virtual Compton scattering. *Phys. Rev. Lett.*, 87:182001, 2001.

[49] Gerhard A. Schuler and Torbjorn Sjostrand. Towards a complete description of high-energy photoproduction. *Nucl. Phys.*, B407:539–605, 1993.

[50] Torbjorn Sjostrand. Pythia 5.7 and Jetset 7.4: Physics and manual. 1995.

[51] E. Volk. *Measurement of the $D^{*\pm}$ Cross-Section at HERMES.* PhD thesis, Ruprecht-Karls-Universität Heidelberg, Germany, January 2001.

[52] Carol Y. Scarlett. *Photon-Gluon Fusion as a way of accessing the gluons' contribution to nucleon spin.* PhD thesis, The University of Michigan, 2002.

[53] P. Hoffmann-Rothe. Λ_c^+ - search in the HERMES - data. HERMES Report, 99-017, 1999.

[54] Marcus Andreas Funk. A measurement of the polarised parton densities of the nucleon in deep-inelastic scattering at HERMES. DESY-thesis-1998-017.

[55] D. E. Groom et al. Review of particle physics. *Eur. Phys. J.*, C15:1, 2000.

[56] F. Meißner. *Measurement of the J/Ψ Cross Section and Double-Spin Asymmetries in Vector Meson Production in Polarised Lepton-Nucleon Scattering at HERMES.* PhD thesis, Humboldt-Universität Berlin, Germany, February 2000.

[57] S. Brons. Private communications.

[58] F. Menden. *Determination of the Gluon Polarization in the Nucleon.* PhD thesis, Albert-Ludwigs-Universität Freiburg, Germany, November 2001.

[59] M. P. Alvarez et al. Photoproduction of the Λ_c^+ charmed baryon. *Phys. Lett.*, B246:256–260, 1990.

[60] K. Abe et al. Lifetimes, cross-sections and production mechanisms of charmed particles produced by 20 GeV photons. *Phys. Rev.*, D33:1, 1986.

[61] M. I. Adamovich et al. Cross-sections and some features of charm photoproduction at gamma energies of 20-GeV to 70-GeV. *Phys. Lett.*, B187:437, 1987.

[62] D. Aston et al. Photoproduction of charmed D mesons at γ energies of 40 GeV to 70 GeV. *Phys. Lett.*, B94:113, 1980.

[63] J. J. Aubert et al. Production of charmed particles in 250 GeV μ^+ - iron interactions. *Nucl. Phys.*, B213:31, 1983.

[64] M. P. Alvarez et al. Study of charm photoproduction mechanisms. *Z. Phys.*, C60:53–62, 1993.

[65] H. Rubinstein and L. Stodolsky. Threshold bump in charm photoproduction. *Phys. Lett.*, B76:479, 1978.

[66] K. Abe et al. Search for a threshold enhancement in the γ p $\rightarrow$ charmed baryon + charmed meson cross-section. *Phys. Rev.*, D30:694, 1984.

[67] A. Bornheim et al. Correlated $\Lambda_c^+\bar{\Lambda}_c^-$production in e^+e^- annihilations at $\sqrt{s}$ approx. 10.5 GeV. *Phys. Rev.*, D63:112003, 2001.

[68] W.H.A. Hesselink. Private communications.

[69] M. Beckmann. Recent results on the helicity structure of the nucleon from HERMES. In *Workshop on Testing QCD through spin observables in nuclear targets*, University of Virginia, Charlottesville, Virginia, USA, April 18-20, 2002.

[70] Dmitri Diakonov, V. Petrov, P. Pobylitsa, Maxim V. Polyakov, and C. Weiss. Nucleon parton distributions at low normalization point in the large N(c) limit. *Nucl. Phys.*, B480:341–380, 1996.

[71] G. van der Steenhoven (contact person) *et al.* New silicon-detector systems for the HERMES front region. Internal HERMES report 97-032, DESY 1997.

[72] J. Visser. *Deep inelastic scattering off hydrogen and deuterium.* PhD thesis, Rijksuniversiteit Groningen, The Netherlands, September 2002.

[73] R. Kaiser *et al.* A large acceptance recoil detector for HERMES. Internal HERMES report 01-017, DESY, 2001.

[74] O. Grebenyuk, editor. *Longitudinal Lambda polarization measured at HERMES*, Singapore, July 2001. World Scientific.

[75] S.L. Belostotski. Longitudinal spin transfer to the Λ hyperon in lepto-production. IX WORKSHOP ON HIGH ENERGY SPIN PHYSICS, Dubna, Russia, Aug 2 - 7, 2001.

[76] M.G. van Beuzekom *et al.* Technical design report of the new silicon-detector system. Internal HERMES report 98-014, DESY, 1998.

[77] J. J. M. Steijger. The HERMES silicon project. *Nucl. Instrum. Meth.*, A447:55–60, 2000.

[78] J. J. M. Steijger. The lambda wheels, a silicon vertex detector for HERMES. *Nucl. Instrum. Meth.*, A453:98–102, 2000.

[79] O. Postma. Vacuum outgassing measurements for the HERMES vertex detector. NIKHEF report MT 99-03, NIKHEF, 1999.

[80] E. Garutti. *Nuclear effects in Semi-inclusive Deep-Inelastic Scattering off ^{84}Kr and other nuclei.* PhD thesis, University of Amsterdam, March 2003.

[81] W. Fallot-Burghardt *et al.* A readout chip for the HERA-B microstrip detectors. In *Proceedings of the second workshop on electronics for LHC experiments*, page 503. CERN/LHCC/96-39, 1996.

[82] M. G. van Beuzekom, E. Garutti, D. Heesbeen, J. J. M. Steijger, and J. Visser. First experience with the HERMES silicon detector. *Nucl. Instrum. Meth.*, A461:247–250, 2001.

[83] W. Wander. *Reconstruction of high energy scattering events in the HERMES experiment.* PhD thesis, Friedrich-Alexander-Universität Erlangen-Nürnberg, April 1996.

[84] M. Amarian *et al.* The HERMES charm ugrade program: A measurement of the double spin asymmetry in charm leptoproduction. Proposal to the DESY PRC, HERMES 97-004, DESY, 1997.

[85] J. J. M. Steijger. Private communications.